



Helmholtz-Zentrum für Ozeanforschung Kiel

RV SONNE
Fahrtbericht / Cruise Report
SO227 TAIFLUX

**Fluid and gas migration in the transition from a passive
to an active continental margin off SW Taiwan**

02.04. – 02.05.2013
Kaohsiung – Kaohsiung (Taiwan)



Berichte aus dem GEOMAR
Helmholtz-Zentrum für Ozeanforschung Kiel

Nr. 11 (N. Ser.)

August 2013



Helmholtz-Zentrum für Ozeanforschung Kiel

RV SONNE
Fahrtbericht / Cruise Report
SO227 TAIFLUX

**Fluid and gas migration in the transition from a passive
to an active continental margin off SW Taiwan**

02.04. – 02.05.2013
Kaohsiung – Kaohsiung (Taiwan)



Berichte aus dem GEOMAR
Helmholtz-Zentrum für Ozeanforschung Kiel

Nr. 11 (N. Ser.)

August 2013

ISSN Nr.: 2193-8113

Das GEOMAR Helmholtz-Zentrum für Ozeanforschung Kiel
ist Mitglied der Helmholtz-Gemeinschaft
Deutscher Forschungszentren e.V.

The GEOMAR Helmholtz Centre for Ocean Research Kiel
is a member of the Helmholtz Association of
German Research Centres

Herausgeber / Editor:
Christian Berndt

GEOMAR Report
ISSN Nr.: 2193-8113, DOI 10.3289/GEOMAR_REP_NS_11_2013

Helmholtz-Zentrum für Ozeanforschung Kiel / Helmholtz Centre for Ocean Research Kiel
GEOMAR
Dienstgebäude Westufer / West Shore Building
Düsternbrooker Weg 20
D-24105 Kiel
Germany

Helmholtz-Zentrum für Ozeanforschung Kiel / Helmholtz Centre for Ocean Research Kiel
GEOMAR
Dienstgebäude Ostufer / East Shore Building
Wischhofstr. 1-3
D-24148 Kiel
Germany

Tel.: +49 431 600-0
Fax: +49 431 600-2805
www.geomar.de

Content

2. Introduction	5
2.1. Objectives of the cruise	8
3. Participants	11
3.1. Scientists	11
3.2. Crew	12
4. Agenda of the cruise	13
5. Work completed and first results	17
5.1. 3D seismic acquisition and processing	17
5.1.1. Formosa Ridge	17
5.1.2. Four-Way-Closure Ridge	19
5.1.3. Results of 3D seismic processing	19
5.1.3.1. Formosa Ridge	19
5.1.3.2. Four-Way-Closure Ridge	23
5.2. OBS experiments	27
5.2.1. Objectives	27
5.2.2. Instrument description	27
5.2.3. Experiment design	27
5.2.3. Preliminary results	29
5.3. Controlled source electromagnetic surveys	33
5.3.1. Overview over the experimental setup of the electromagnetic (EM) surveys at Formosa Ridge and Four-Way-Closure	33
5.3.2. Formosa Ridge Survey	35
5.4. Heat flow	41
5.4.1. Objectives	41
5.4.2. Work at sea	42
5.4.3. Preliminary results	42
5.5. Bathymetry	45
5.5.1. Equipment used	45
5.5.2. Sound velocity profiles	45
5.5.3. Results	46
5.6. Deep-towed sidescan sonar	51
5.6.1. Equipment used	51
5.6.2. Deployments	53
5.6.3. Results	53
5.7. HyBis operations	65
5.7.1. The HyBis vehicle	65
5.7.2. Laboratory control unit setup	66
5.7.3. High-voltage power setup	67
5.7.4. Dive narrative and vehicle performance summary	67
5.7.4. Summary of HyBis operations	69
5.8. Geological Sampling	69
6. Acknowledgements	69
7. References	70
8. Appendices	74
Appendix 1: Multi-beam, Parasound	74
Appendix 2: Sidescan Sonar profiles	80
Appendix 3: OBS stations	81
Appendix 4: Seismic profiles	82
Appendix 5: Controlled source EM	90

Appendix 6: HyBis transects	96
Appendix 8: TV-Grap	99
Appendix 9: Sound velocity profiles	99

1. Cruise summary

The underlying scientific motivation of SO227 was to constrain the geological processes that control the distribution and saturation of hydrate in marine sediments. The most important objective of the cruise was to observe the effect of additional fluid advection along blind thrusts into the gas hydrate stability zone. With its clear distinction into a passive margin and an active margin the area SW of Taiwan is particularly well suited for this kind of research because it is very well studied and it is known where the tectonic structures of the compression and subduction zone disturb the otherwise fairly homogeneous surface sediments of the margin.

After a reconnaissance survey using multi beam echo sounder and side scan sonar we selected two sites that are typical for the active and passive margin, respectively. At these two sites we carried out comprehensive geophysical experiments including high-resolution 3D seismic imaging with the P-Cable system, ocean bottom seismometer (OBS) deployments, controlled source electromagnetic (CSEM) measurements, heat flow measurements, and ground-truthing using HyBis and TV grab. While the P-Cable data allow us to determine the internal structure of the study areas down to a depth of approximately 500 m below sea floor, the OBS and CSEM data will constrain the hydrate and free gas saturation along two-dimensional transect through the 3D seismic cubes. The heat flow data will provide information on the thermal conditions of the sediments.

The first site covers the Formosa Ridge on the passive margin of the South China Sea. The ridge is the result of canyon erosion in the north, west, and east. The high-resolution three-dimensional seismic data show a continuous bottom simulating reflector (BSR) marking the base of the hydrate stability zone. Particularly, underneath the canyon in the north the BSR is much shallower than underneath the centre of the ridge. This may indicate that the canyon incision has changed the hydrate stability field and that hydrate formation at depth has not been able to adjust to the new pressure and temperature conditions.

The second site includes a roll over anticline called Four-Way-Closure Ridge which is the surface expression of an underlying blind thrust. In this area numerous high amplitude reflectors occur above the BSR. This unusual observation may suggest very high gas hydrate saturations and coeval presence of free gas and gas hydrate in the sediments. Evaluation of the OBS and CSEM data will allow to test this hypothesis. The 3D seismic data clearly show fluid migration pathways through the gas hydrate stability to the sea floor.

Sea floor video footage and sampling confirmed the presence of on-going methane seepage at the Formosa Ridge above the fluid migration pathway imaged in the 3D seismic data. They also establish that there is at least one seep on the Four-Way-Closure Ridge at which methane is released into the ocean above another seismically imaged fluid migration pathway. This is the first active seep site with chemosynthetic ecosystems discovered on the active margin SW off Taiwan.

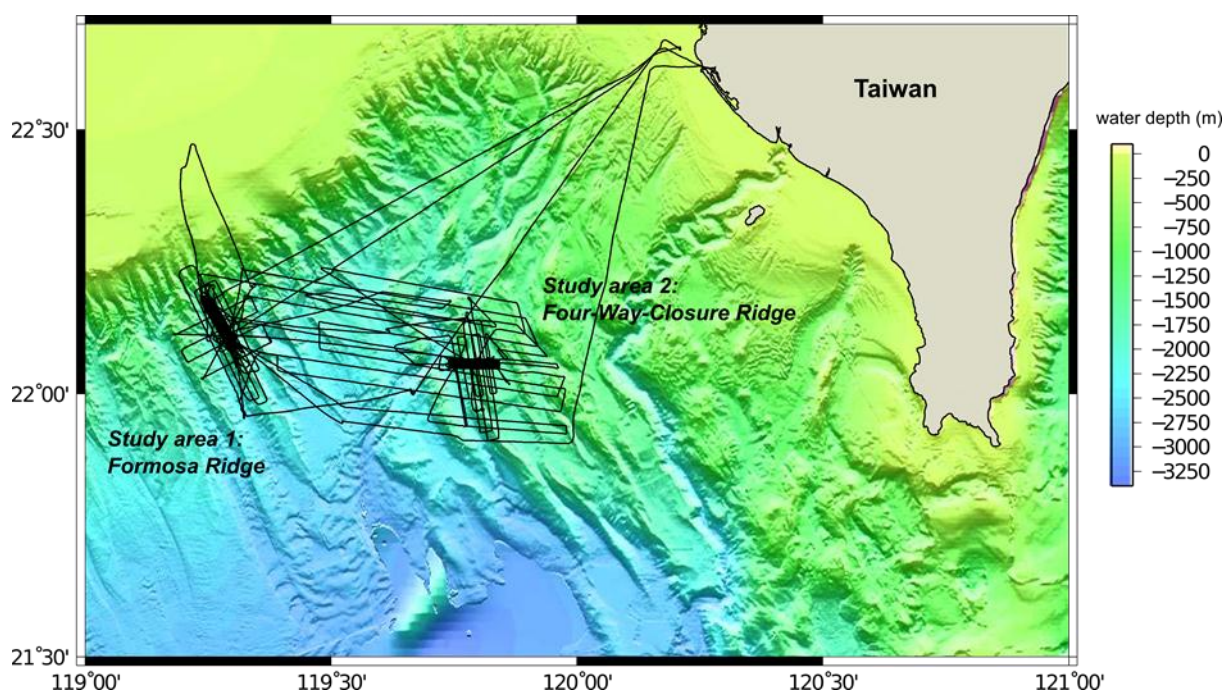


Figure 1: Cruise SO227 started from Kaohsiung, Taiwan on 2-4-2013, and finished in Kaohsiung, Taiwan on 2-5-2013. The main working areas were the Formosa Ridge and the Four-Way-Closure Ridge SW of Taiwan.

2. Introduction

Gas hydrates are ice like compounds that trap gas molecules under low temperature and high pressure conditions typically encountered in marine sediments. Because of the enormous amount of natural gas that is captured in gas hydrates, i.e. some 500 to 4500 Gt of carbon (Milkov, 2004, Archer and Buffet, 2005) compared to 700 Gt in the atmosphere at present, gas hydrate systems are an important element of the global carbon cycle. Whereas some countries such as Japan, India and Taiwan consider them a future source of energy some are concerned that greenhouse gases may be released unintentionally if global warming continues at its present rate (Kennett et al., 2003; Berndt, 2005, Westbrook et al., 2009). Therefore, it is important to understand the geological processes that lead to the formation of gas hydrates and those that may mobilize the gas that is captured in the hydrate systems. Gas hydrates have been the subject of various research projects over the past two decades, but there are still fundamental processes that are poorly understood, such as the rates of formation and dissociation of gas hydrates, and the role of fluid migration in their mobility (Haacke et al., 2008).

The understanding of the formation of free gas zones beneath the base of hydrate stability was recently improved, following considerations of methane solubility beneath the hydrate zone (Haacke et al., 2007; 2008). The mechanisms driving the formation of the free gas zone may differ considerably depending on the rates of upward fluid flux, which can vary greatly between passive and active margin settings (Haacke et al., 2007; Liu and Flemings, 2007). The mobility of free gas and the mechanisms that drive it, both beneath the hydrate layer and within the region of hydrate stability, is the focus of much ongoing research and debate. Possible scenarios that allow the migration of free gas through hydrate bearing sediments, where conversion to gas hydrate is prevented, include: a limitation in the availability of water, advection of warm fluids, and a marked increase in local pore water salinity as hydrate forms (Ginsburg and Soloviev, 1997; Wood et al. 2002; Liu and Flemings 2007).

Although gas hydrates represent an enormous global source of methane gas, it is of fundamental importance to address the issue of where hydrates are sufficiently concentrated that they could be economically exploited (Milkov and Sassen 2002; Johnson and Max, 2006). Studies conducted in various hydrate provinces around the world indicate that hydrate-bearing sands have the best potential for commercial development (Johnson and Max, 2006). Not only do these sediments have a high pore space fraction available for the deposition of highly-concentrated deposits, but the extraction of gas at viable rates seems to favour these more porous lithologies – in contrast to mudstones for example (Boswell, 2007). A major challenge will be to successfully use remote-sensing methods to characterise the stratigraphic locations and concentrations of attractive hydrate deposits within the hydrate stability zone. The character of gas hydrate precipitation in marine sediments can differ markedly from site to site in response to variations in the physical properties and surface chemistry of sediments (Clennell et al., 1999). At the pore scale, gas hydrates may form within pore spaces without interacting with the sediment matrix, or they may contribute to building or cementing the sediment matrix (e.g. Winters et al., 2004). Various models, both rock physics-based and empirical, have been proposed for the prediction of gas hydrate concentration from elastic velocities (e.g. Ecker et al., 1998; Carcione and Tinivella 2000; Jakobsen et al. 2000). Significant differences between model predictions can arise under different sedimentary conditions such as porosity and clay content (Chand et al., 2004). On a larger scale than the pore scale, gas hydrate precipitation can fill open fractures (vein-filling in secondary porosity), or can occur as massive deposits closer to the seafloor (Abegg et al., 2007; Long et al., 2009).

Relationships between gas hydrates and submarine slope failure, an area of research that first began with an association made by Carpenter in 1981, are still widely-studied around the globe (e.g. Paull et al., 2000; Pecher et al., 2005; Brown et al., 2006; Sultan 2007; Micallef et al, 2009). The Storegga Slide off mid-Norway is the best studied example for a major landslide in a hydrate area. For this event we know that gas hydrate dissociation has not been the trigger (e.g. Mienert et al., 2005; Berndt et al., 2004; Brown et al., 2006), but hydrates have still played a role in the evolution of the slide (Micallef et al., 2009). It seems likely that hydrate dissociation due to a change in environmental conditions (i.e. a reduction in pressure or an increase in temperature) can liberate large volumes of free gas that increase the pore-fluid pressure within sediments, thereby decreasing their mechanical strength (Xu and Germanovich, 2006). Studying the hydrates off Taiwan, of which the surface-near accumulations are particularly sensitive to bottom water temperature changes, will provide further constraints on this process.

The potential impact of past climate change on gas hydrate destabilisation has been widely reported (e.g. Dickens et al., 1995; Hesslebo et al., 2000; Kennett et al., 2003) and there is great concern that present day gas hydrate provinces will be significantly destabilised in response to global warming (Milkov and Sassen, 2003; Fyke and Weaver, 2006, Reagan and Moridis, 2007). The shallowest hydrate deposits, subject to lower pressures, are the most prone to temperature-induced dissociation as the temperature range of stability is smaller at lower pressures. Theoretical simulations of the potential impact of anthropogenically-forced elevated atmospheric CO₂ suggest that the global gas hydrate stability zone responds significantly to increased CO₂ over time scales of 10,000 years (Fyke and Weaver, 2006). Supplementing theoretical studies, but on a regional scale and a much smaller time scale, are numerous observations of methane venting on the West Spitsbergen continental margin that are suggested to be the response to warming of ocean bottom temperatures (by about 1 °C) over the past 30 years (Westbrook et al., 2009). Seismic reflection surveys may also show evidence for the transient nature of hydrate stability, in the form of double BSRs. It has been

suggested that as the region of hydrate stability shifts and a new BSR forms, relics of the former BSR (representing the former state of stability) may be left behind, resulting in the double BSR phenomenon (e.g. Nouze et al., 2004; Golmshtok and Soloviev, 2006).

The area offshore south-western Taiwan (Figure 1) offers a unique opportunity to further our understanding of geological controls on gas hydrate formation, dissociation, and mobilization, because gas hydrates are very wide-spread, and the area comprises different plate tectonic settings. The Taiwan collision zone is located along the boundary between the Eurasian plate and Philippine Sea plate where the Chinese continental margin has collided with the northern segment of the Luzon island arc (Bowin et al., 1978). South of Taiwan, oceanic lithosphere of the South China Sea is subducting eastward beneath the Philippine Sea plate along the Manila Trench (Figure 1) (Bowin et al., 1978; Taylor and Hayes, 1983). To the north, the thick Chinese passive margin is juxtaposed to the convergent boundary, causing the rapid uplift of the Taiwan fold and thrust belt (Suppe et al., 1984; Hirtzel et al., 2009; Chi and Reed, 2008). Taiwan is among the best seismically-imaged hydrate regions in the world. Two dense multi-channel seismic reflection datasets have been acquired in the region offshore southwestern Taiwan (Fig. 1, Liu et al., 2006; Chi et al., 1998). They provide the basis for studying the distribution and sub-bottom depth of the BSR. In addition, 160-channel data collected by R/V Ewing have been used for imaging deeper crustal structures and also for analysing velocity information at shallow depths (e.g. Schnurle et al., 2004). In 2009, R/V Langseth collected almost 3-months' worth of 468-channel MCS data around Taiwan, many of the survey lines covered the hydrate region. A wide-spread bottom-simulating reflector (BSR) which represents the interface between gas hydrates and free gas covers an area of more than 15000 km² west and south of Taiwan (Fig. 1). It ranges in sub-bottom depth from a few meters to several hundred meters below sea floor (Chi et al., 1998). We have documented the spatial extent and sub-bottom depth of more than thousand segments of this BSR and found that at least 1023 km³ of sediments fall inside the hydrate stability field in this region (Chi et al., 2006, Liu et al., 2006). The Ewing and Langseth air gun sources were also recorded by a very dense 2D OBS array. Velocity analyses using the large offshore data recorded by the streamers and by the OBSs have shown evidence for a hydrate layer above the BSR and a layer of gas below it (Schnurle et al., 2004, Cheng et al., 2006). Preliminary studies using OBS data show that the hydrate concentration is higher (about 15-20%) in the passive margin compared with that (about 10%) in the active margin (Chen, 2009). On the other hand, joint-inversions of MCS/OBS gave a lower estimate of 0-10% hydrate saturation in the sediment (Schnurle et al., 2004). In summary, there is evidence for wide-spread occurrence of gas hydrates. However, just from mapping the BSR occurrence it is not possible to deduce the amount of methane. To assess this it is necessary to constrain the concentrations, and the way in which hydrates occur in the sediments.

A regional in-situ heat flow survey has been conducted over the last decade (c.f. Shyu et al., 2006). Chi and Reed (2008) have argued that some of the discrepancy consistently found between the BSR-based heat flows and the in-situ measurements at shallow water depth is due to temperature fluctuation on the seafloor related to sea-level changes, earthquake generated perturbations (Chi et al., in prep.), and other processes.

Many geochemical datasets derived from sediment cores and bottom water have been systematically collected and analysed. The data document the presence of some very active venting sites in the region. Chiu et al. (2006) have found that the distribution of the gassy sediments is spatially associated with a clear BSR. Yang et al. (2008) have studied carbon isotopic composition of dissolved inorganic carbon (DIC) and found large methane flux from depth just south of this region, in a rate compatible with that of the Blake Ridge of the US.

They also found different geochemical characteristics of this region compared with the results from another core along the passive margin further to the west. Currently, both biogenic and thermogenic gases have been found in the active margin (Oung et al, 2006), while only biogenic gases have been reported in the passive margin (Liu, 2006). Wang et al. (2008) discovered geochemical anomalies in the cored sediments near the faults, and they proposed that active fluid migration along the fault has affected hydrate dissociation and formation in this region. A 25-meter long piston core was taken in this region on R/V Marion Dufresne. And Lin et al. (2008) propose possible temporal changes in methane migration modes based on the identified alternating anoxic/oxide/anoxic zones in the core. It is one of the important goals of the proposed project to constrain further the rates at which hydrates form and dissociate.

Analysing all the available datasets, Lin et al. (2009) have proposed a model for the formation of hydrates in this region. In their model the hydrates in the passive margin and near the toe of the accretionary prism are composed mostly of biogenic gas. As the collision progresses, the Taiwan fold and thrust belt dumps high amounts of organic carbon into the marine sediments. Such organic materials may help produced methane trapped in hydrates offshore Taiwan (Chi et al., 1998). On the other hand, the hydrates near the deep-rooted emergent thrusts are possibly dominated by thermogenic methane components (Lin et al., 2005). As a result Lin et al., (2009) have divided the active margin into a frontal segment where the thrusts are mostly blind, and a rear segment where the thrusts emerge at the seafloor. Active fluid venting on the seafloor has been documented in shallow water region near the coast (Liu et al, 2006). You et al. (2004) have argued that farther on land the gas emitted from the sub-areal mud volcanoes is mostly thermogenic and is a result of salient sedimentary pore fluids with waters affected by clay dehydration released at depth. Yang et al. (2006) have compared the water samples collected near the emerging thrusts with the gas samples collected from mud volcanoes on shore. They found that the offshore gas source is very similar to that of the on-shore mud volcanoes. The unique onshore datasets provide important additional constraints for studying orogenic-scale methane emission from the crust and its potential climate impacts.

2.1. Objectives of the cruise

In spite of three decades of research on marine gas hydrates there is still very much open, but with the recently developed technologies such as high-resolution 3D seismic imaging, CSEM in conjunction with proven techniques such as high-resolution ocean bottom seismometer experiments, and possibly even a major drilling campaign we stand an excellent chance to make a major step forward in our fundamental understanding of marine gas hydrates. Through the proposed cruise we will address five questions of fundamental importance for understanding the role of gas hydrates in the climate system, their potential as a future energy source, and their role for slope stability.

Why does hydrate form where it forms?

The regional gas hydrate stability zone (GHSZ) is conventionally defined as the zone where gas hydrates are stable, given a particular heat flow regime (geothermal gradient), fluid pressure regime, gas composition and salinity. However, although gas hydrates may be stable within a large region, they are not uniformly concentrated within this region – there will be places where gas hydrates are absent and also areas where they exist in relatively high concentrations. The importance of focused fluid flow in generating economically valuable accumulations of gas hydrate has been underscored in many recent studies (e.g. Milkov and

Sassen, 2002, 2003; Liu and Flemings 2007). In the offshore southwestern Taiwan area, correlations have been made between particular geological features, such as faults and folded strata in anticlines, and enhanced fluid flow into the hydrate system (Chi et al. 1998; Lin et al. 2009). We will seek to improve the understanding of the conditions that promote the migration of gas-charged fluids into and through the GHSZ. It will be important to determine the relative importance of sedimentary fabrics and structural features (such as faults and fractures) in the context of fluid migration and hydrate precipitation styles within particular regions of the study area (e.g. Milkov and Sassen, 2002). In terms of hydrate distribution at different stratigraphic levels of the GHSZ, we will aim to determine whether there are any patterns that can be observed pertaining to a preferred depth region within the GHSZ for the formation of highly-concentrated hydrate deposits. In other words, the highest concentrations of gas hydrate are located near the base of the GHSZ, somewhere in the middle, or nearer the seafloor. The character of hydrate distribution within the GHSZ is fundamentally inseparable from the flow dynamics and permeabilities of the sedimentary reservoirs (Nimblett and Ruppel 2003; Ruppel, 2007). Therefore, a sound assessment of sediment characteristics and controls on fluid flow pathways will be required to address this question. For example, several recent studies draw relationships between precipitation style and depth within the sedimentary section, i.e. massive deposits nearer the seafloor and vein-filling deposits at greater depths (Abegg et al., 2007; Long et al., 2009). The relation of gas hydrate concentration to lithofacies distribution is of utmost importance for assessing the economic value of hydrates and the SUGAR project.

In a regional context (i.e. the proposed study area), there is a pre-existing hypothesis that rapidly-deposited terrigenous sediments with relatively high organic carbon content in the north western part of the Manila Trench may be correlatable with increased hydrate concentrations (Chi et al. 1998). We will test this hypothesis and improve the understanding of the processes that govern the spatial distribution of attractive hydrate accumulations in the study area. The area offers a unique opportunity to study gas hydrates in a region that is characterised by the juxtaposition of an accretionary wedge on top of a rifted continental margin (Chi et al. 1998; McDonnell et al. 2000; Lin et al. 2009). Complex tectonic relationships, for example at the confluence between the passive and active margins, may have important implications for methane origin, fluid flow and hydrate formation. Based on BSR occurrences, gas hydrates may be more widely distributed in the accretionary wedge than in the South China continental margin (Lin et al., 2009). Lin et al (2009) suggest that this may be due to multiple fault zones in the wedge that encourage the ascent of deep-seated gas-bearing fluids towards the GHSZ. The addition of these fluids to shallow biogenic gas could result in a larger source of methane for hydrate formation.

We have chosen sites in both the passive margin and the active margin, from variable water depths, in order to discern differences between gas hydrate dynamics in the different tectonic settings and depth sections of the hydrate stability zone.

What are the geological processes that control gas hydrate dissociation?

The dynamics of the gas hydrate system are important for (1) Understanding the role of hydrates on future climate change as hydrates that dissociate fast will inject more methane into the water column and potentially into the atmosphere in a short time. As methane gets oxidized very quickly in the atmosphere, the partial pressure of methane can only rise as a consequence of hydrate dissociation if hydrate dissociation is fast. (2) Assessing the commercial value of a gas hydrate deposit, because the easier they are to dissociate, the easier and more cost-efficient it is to extract the gas.

Whereas the theoretical gas hydrate stability conditions are well understood (e.g. Sloan, 2007) there is still much debate about the rate at which gas hydrates adapt to new temperature and pressure conditions in a real geological situation (Jung and Vogt, 2004, Berndt et al., 2005). This is due to a number of unconstrained physical processes such as the development and diffusion of latent heat, the way in which a heat anomaly progresses through the sediments, i.e. by conduction or advection, and the distribution of hydrates in the subsurface. As hydrates are particularly sensitive to temperature changes (more than pressure changes), it is most important to constrain the temperature evolution in the subsurface which is governed by the advection of fluids and conduction of heat. Unfortunately, all the aforementioned uncertainties affect the temperature evolution.

Although attempts are being made to constrain the physical processes in the laboratory and from a theoretical point of view (e.g. Sultan et al., 2004), we are convinced it is necessary to make observations in a real marine gas hydrate system that can be used to calibrate the theoretical and inform the laboratory studies. We propose to investigate the response of the hydrate system to constrained changes in the pressure and temperature conditions over three time scales. On the long scale we wish to investigate the effect of tectonic uplift in the SW of Taiwan on the marine hydrates, and on the intermediate time scale we will look at the directly measured temperature variations in the shallow part of the gas hydrate system and compare them with observed seepage. Finally, on the short time scale, we will look at the possible temperature perturbation caused by fluid migration along fault zones induced by many large earthquakes in this region (Chi et al., in prep.). Through this approach we should be able to constrain the time that it takes for hydrates to adapt to a change in pressure and temperature conditions.

How does gas migrate through the gas hydrate stability zone?

In the last decade it has emerged that methane can migrate through the GHSZ in the gas phase, i.e. not only in solution (e.g. Wood et al. 2002; Tréhu et al. 2004; Liu and Flemings 2006, 2007). We aim to provide more insight into the mechanisms that can allow this process to occur, as there is evidence that highly-concentrated gas hydrate deposits may form within or around particular features, such as gas chimneys, that provide conduits for free gas migration through the GHSZ (e.g. Liu and Flemings 2007, Haacke et al., 2008). We will search for examples of this process in the study area, and will then seek to determine the geological conditions that support their formation – i.e. not only structural and stratal relationships, but also temperature, pressure and chemical conditions.

What are the potential dangers of gas extraction from hydrates?

Many of the hazards associated with gas extraction from hydrates are continually being assessed by oil and gas industry initiatives, due to the need for extraction of conventional hydrocarbons from beneath hydrate deposits. This process has required an understanding of how hydrate-bearing sediments respond to drilling-induced perturbations of the local stress field and temperature and pressure regimes (Birchwood et al., 2007). Recent numerical simulations of hydrate reservoirs, which considered the geo-mechanical response of sediments to drilling operations, show that induced warming due to production activities can affect the cohesion and stability of hydrate-bearing sediment (e.g. Freij-Ayoub et al., 2007). The decrease in sediment integrity, which is even more pronounced in unconsolidated sediments typical of the shallow seafloor, could be extremely hazardous to ongoing operations as drilling platforms and equipment could become unstable. The potential liberation of

uncontrolled excess fluid pressure as hydrates are dissociated, not only has implications for sediment strength, but also for borehole blowouts and damage to drilling equipment. The characterization of sediment properties and their potential response to various gas extraction techniques (e.g. thermal stimulation, depressurization, inhibitor injection, or CO₂ substitution – Ruppel 2007) would have to be well-understood before energy production from gas hydrates in the proposed study area could begin. Many of the data we will collect will provide insight into the dangers of gas extraction from hydrates. For example, gravity cores will expose lithologies that can be geotechnically-tested for sediment strength properties, and remotely sensed data (electromagnetic and seismic) will provide information on the distribution and concentration of free gas and gas hydrate, both of which can drastically influence the integrity of sediments.

3. Participants

3.1. Scientists

Name	Expertise	Institute
1. Prof. Christian Berndt	Chief scientist	GEOMAR
2. Dr. Marion Jegen	Leader CSEM	GEOMAR
3. Sebastian Hölz	CSEM	GEOMAR
4. Malte Sommer	CSEM	GEOMAR
5. Dr. Chih-Wen Chiang	CSEM	NCU
6. Dr. Gareth Crutchley	Leader P-Cable	GEOMAR
7. Sina Muff	P-Cable	GEOMAR
8. Ho-Han Hsu	P-Cable	IONTU
9. Liwen Chen	P-Cable	IGNTU
10. Kathrin Lieser	Leader OBS	GEOMAR
11. Dr. Wu-Cheng Chi	OBS	SINICA
12. David Bösing	OBS	GEOMAR
13. Judith Elger	OBS	GEOMAR
14. Dr. Tomas Feseker	Heat flow	MARUM
15. Dr. Ingo Klauke	Seafloor imaging	GEOMAR
16. Prof. Saulwood Lin	Sedimentology	IONTU
17. Gero Wetzel	HyBis	GEOMAR
18. Anja Bräuning ¹	Watch keeper	MARUM
19. Kira Aßhoff ²	Watch keeper	MARUM
20. Fang Hsu Kuo	Watch keeper	TORI
21. Martin Wollatz-Vogt	CSEM engineer	GEOMAR
22. Torge Matthiessen	Seismic technician	GEOMAR
23. Patrick Schröder	Electronic engineer	GEOMAR
24. Olav Schwartz	Engineer	GEOMAR
25. Kai-Jhung Guo	Military Observer	Taiwan Navy

GEOMAR Helmholtz Centre for Ocean Research Kiel, Marine Geodynamics,
Wischhofstr. 1-3, 24148 Kiel, Germany.

¹Stayed onshore from April 2 to April 5 to accompany Kira Aßhoff

²Only participated in the cruise preparation until April 2 for medical reasons

SINICA	Academia Sinica Institute of Earth Sciences, 128 Academia Road, Taipei, Taiwan.
MARUM	Center for Marine Environmental Sciences (MARUM) University of Bremen, Klagenfurter Straße, 28359 Bremen, Germany.
IONTU	Institute of Oceanography National Taiwan University, No. 1, Sec 3, Roosevelt Rd, 10617, Taipei, Taiwan.
IGNTU	Institute of Geosciences National Taiwan University, No. 1, Sec 3, Roosevelt Rd, 10617, Taipei, Taiwan.
NCU	Department of Earth Sciences, National Central University, No. 300, Jhongda Rd., Jhongli City, Taiwan.
TORI	Taiwan Ocean Research Institute, No. 219, Sec. 1 Dongfang Rd., Qieding Dist., Kaohsiung City 85243, Taiwan (ROC).

3.2. Crew

Name	Rank
1. Oliver Meyer	Master
2. Jens Christian Goebel	Chief Officer
3. Lars Hoffsommer	2. Officer
4. Tim Henning	2. Officer
5. Dr. Bodo Bauer	Ship's Doctor
6. Jörg Leppin	System Manager
7. Wolfgang Borchert	System Manager
8. Werner Guzman-Navarrete	Chief Engineer
9. Andreas Rex	2. Engineer
10. Steffen Genschow	2. Engineer
11. Thomas Beyer	Electrician
12. Volker Blohm	Fitter
13. Jens Kuderski	MPC/Motorman
14. Torsten Bolik	MPC/Motorman
15. Frank Tiemann	Chief Cook
16. Sebastian Matter	2 nd Cook
17. André Garnitz	2 nd Cook
18. Andreas Pohl	Chief Steward
19. Maik Steep	2. Steward
20. Andreas Schrapel	Boatswain
21. Reno Ross	A.B.
22. Ingo Fricke	A.B.
23. Jürgen Kraft	A.B.
24. Finn Mohrdiek	MPC/A.B.
25. Benedict Kuhn	Trainee
26. Sebastian Uwe Thimm	Trainee
27. Oliver Eidam	MPC/A.B.
28. Michael Barkow	A.B.

4. Agenda of the cruise

Saturday 30 March

The cruise started with a big press reception in the morning. The Vice President of National Taiwan University, the Director of the National Science Council of Taiwan, the Deputy Director General of the German Institute in Taipei, the director of the National Energy Program, and representatives of various other organisations such as the harbour master of Kaohsiung and the Taiwanese Ocean Research Institute attended it. After the press conference we took on board two containers with provisions which were not allowed to be unloaded onshore because of foot and mouth disease. We had to sail out of the 24 mile zone where we stripped the first container until night fall.

Sunday 31 March

In the morning we stripped the other container and sailed back to Kaohsiung.

Monday 1 April

After custom clearance we started to unload the two empty food containers and took on board the scientific equipment which took the entire day. During the afternoon the ship's doctor took Kira Aßhoff to the hospital where she was diagnosed serious illness. This meant that she could not take part in the cruise. Because she was in a bad state we decided to leave one other student (Anja Bräuning) on shore with her and send her home with the first possible flight and pick up Ms Bräuning later.

Tuesday 2 April

Tuesday morning at 0800 we departed from Kaohsiung. We reached the study area at 1315. First we ran the water sampling rosette with a CTD to measure a sound velocity profile for the multibeam data acquisition. Afterwards at 1630 we carried out tests of the OBS and CSEM releasers. At 2000 we deployed the side scan sonar system at Formosa Ridge, but the deep sea cable had a bad connection and we had to recover the system. Throughout the night we collected multi-beam bathymetry data while the cable was re-terminated and finally abandoned for the LWL cable. The weather was overcast with 1-3 m swell from various directions, abating.

Wednesday 3 to Thursday 4 April

The multi-beam bathymetry and PARASOUND survey continued until lunchtime. By that time the LWL cable was prepared and we deployed the side scan sonar south of Formosa Ridge. During the next two days we surveyed the entire Formosa Ridge and the canyons surrounding it. This worked well in spite of the rugged topography (up to 45 degree slopes). The most exciting area was as expected the southern summit of the ridge where we found both active flares in the water column and carbonates at the sea floor. There were heavy rainstorms on Thursday afternoon but the swell came down.

Friday 5 April

At 0100 in the morning we started to retrieve the side scan sonar which was on deck at 0200. A length of 4 cm black rope had been caught in the depressor weight and was cut loose. At 0200 we set off for Kaohsiung to pick up Ms Bräuning who had looked after Ms Aßhoff. She came on board with a pilot boat at 0800. We used the time in the wind shadow to stow away the side scan sonar and rig the back of the ship for seismic operations. At 0900 we sailed back to the deployment station for the OBS on Formosa Ridge. We arrived back in the study area and deployed twelve OBS along a profile on the crest of the ridge and in the vicinity of a cluster of six OBS deployed by Taiwanese colleagues prior to our cruise on the

southern summit of Formosa Ridge. All OBS were out by 1730. Then we started to deploy the P-Cable system which took until 2300. We began shooting at 2300.

Saturday 6 April

At 0300 the starboard paravane toppled over during a turn. This broke the cable of the power supply for the GPS antenna. We fixed this problem and continued shooting at 0530. During the rest of the day the system worked fine and we collected good data although the weather deteriorated.

Sunday 7 April

At 0300 the starboard paravane toppled over again due to heavy seas. When pulling the system towards the ship it turned around the cross cable and had to be taken onboard. Throughout the rest of the night we steamed slowly into the wind which was now coming in at force 7-8 causing 3-4 m high waves. In the morning when we tried to turn around to the survey area the data cable was severed and the entire system had to be taken on board. We steamed back to the survey area shooting long perpendicular lines to obtain a wider range of azimuths for the 3D tomography of the OBS data. In the meantime repairs of the P-Cable system took place while waiting for more suitable weather.

Monday 8 April

P-Cable surveying made good progress until lunch time, when something got caught in the system. The paravanes first closed up on each other and then parted when the cable broke. The system was retrieved, repaired and redeployed under four hours and was back in surveying mode at 18:00.

Tuesday 9 April

We continued to shoot P-Cable data until 19:00 when the weather deteriorated because of a new frontal system. We recovered the P-Cable by 20:00 and continued multi-beam bathymetry surveying and PARASOUND profiling. The weather was overcast and winds were up to force 6.

Wednesday 10 April

In the morning we began recovering the OBS. This took until 15:00. All twelve OBS could be retrieved. Afterwards we steamed to the side scan sonar deployment site on Four-Way-Closure Ridge. Winds varied between for 6 and 8. The side scan sonar was deployed at 0700 and surveying continued throughout the rest of the night without any interruptions.

Thursday 11 April

The side scan sonar data revealed several previously unknown seep sites on Four-Way-Closure Ridge making suitable targets for sampling. At 3 in the afternoon abandoned long-line fishing gear got caught in the depressor. We slowed down to reduce the tension on the cable, but the tension increased to 7 tonnes before most of the fishing gear ripped loose. We continued the survey until 1900 and retrieved the side scan sonar finding some remnants of the fishing gear still caught on the depressor. Afterwards we steamed back to Formosa Ridge.

Friday 12 April

From midnight to 0800 we carried out a heat flow survey across the northern part of Formosa Ridge to ascertain if canyon incision indeed causes a shift in the hydrate stability field. At 0900 we started to deploy the OBEM along the ridge top.

Saturday 13 April

The OBEM deployment was successfully finished at 0800 and we started to deploy the receiver. Due to electrical problems and steep topography which caused the arms of the transmitter to stay in the upright position progress was slow and only three out of 32 measurements could be completed.

Sunday 14 April to Tuesday 16 April

We recovered Sputnik at 0230 and carried out heat flow measurements until 1000. Afterwards we redeployed the P-Cable seismic system. The system was running without interruption in very calm weather until 1630 on Tuesday 16. By 1730 everything was back on deck and we deployed the repaired Sputnik.

Tuesday 16 April to Thursday 18 April

Sputnik was working perfectly in calm weather and the southern summit of Formosa Ridge could be measured by CSEM. Originally it was planned that we would have to leave the study area by Wednesday 17 because Taiwanese and American colleagues wanted to deploy their AUV, but in a (for us) fortunate turn of events they had technical problems and we could carry on measuring until we finished our experiment by 1200 on Thursday 18. Afterwards we recovered the OBEM receivers releasing them acoustically and towing them to RV Sonne with help of the tender. All OBEMs were on board by 1900. Throughout the night we continued the regional mapping with multi-beam and PARASOUND to establish whether Formosa Ridge and Four-Way-Closure Ridge are representative for the passive and active margin, respectively.

Friday 19 April

In the morning we deployed twelve OBS across the Four-Way-Closure Ridge. In calm and sunny weather this could be completed within four hours. Right afterwards we deployed the P-Cable system. For this we had changed the hydrophone and removed one of the double floats for each T-junctions. At 100 m trawl cable length the system towed beautifully at 2-3 m depth and 144 m spread.

Saturday 20 April

P-Cable surveying continued in calm weather.

Sunday 21 April

P-Cable surveying continued until lunch time when the weather picked up. At 1400 we decided to recover the P-Cable system in force 5 and 2 m waves. This turned out to be the right decision because we discovered that one of the chains that hold the airgun had got disconnected and there was wear on the cross-cable. For the rest of the day and throughout the night we shot strike profiles across the OBS to obtain long offsets also in this direction. At the same time we repaired the damages on the P-Cable system.

Monday 22 April

On Monday morning at 0630 the weather had calmed down sufficiently to continue P-Cable seismic acquisition. At 1000 we had redeployed the system and continued shooting throughout the rest of the day.

Tuesday 23 April

Just before midnight we lost connection to the two starboard streamers. When retrieving the system it turned out that the cross-cable had parted between streamer 12 and 13. The reason is unclear, but it looked as if the strength member had been worn off. The timing of this incident was fortunate because we had just finished the last planned line of the cube and

only small coverage gaps remained. Throughout the rest of the night we acquired multi-beam and PARASOUND data between study areas 1 and 2. At 0800 we began to deploy the OBEM using the Posidonia releaser. This carried on for the rest of the day.

Wednesday 24 April

At 0430 we had deployed the last OBEM. From 0500 to 1200 we retrieved the OBS without any problems. At 1300 we deployed the electromagnetic source Sputnik. Because of light winds and 1 kt easterly current that made navigation difficult we started in the middle of the profile across Four-Way-Closure Ridge and worked our way eastward to avoid the steep flank of the ridge until the end of the deployment.

Thursday 25 April

Except for a short interruption in the afternoon due to a cable problem, Sputnik operations continued successfully in calm weather until 1830. Then the system was retrieved and we deployed the heat flow probe.

Friday 26 April

Until the morning we had occupied 12 stations from the west up onto Four-Way-Closure Ridge Ridge. At 0900 the probe was back on deck and we prepared the HyBis ROV for video imaging of the seep sites to ground truth the side scan sonar imagery. The system was deployed at 1300 and during the first dive we discovered chemosynthetic communities on Four-Way-Closure Ridge Ridge that showed that the seep is still active. We also took a sediment sample to obtain carbon isotope information. During a second dive at this seep site we discovered bacterial mats. The following dive was dedicated to video imaging several other side scan sonar anomalies on the western flank of Four-Way-Closure Ridge Ridge.

Saturday 27 April

During the night we carried out a fourth and fifth dive at the large seep discovered in side scan sonar data on the unnamed ridge south of Four-Way-Closure Ridge Ridge. During the first of these dives we collected a couple of carbonate chimney fragments. During the second we mapped out the extent of the seep. At 0800 we recovered HyBis and sailed back north to release the OBEM stations. This was finished by 1700. All 12 OBEM came back up to the surface. To continue HyBis operations we sailed back into survey area 1 at Formosa Ridge where we arrived at 2000. We deployed HyBis on the western flank of the ridge 400 m northwest of the southern summit. For the first three hours we only saw the muddy side of the seafloor, but at 2300 we found the main seep with mussel colonies, crabs, big slabs of carbonate and evidence for gas bubbles in the Parasound data.

Sunday 28 April

At 0000 we made a first attempt to collect samples, but this only yielded some sediments at the side of HyBis. A much more successful grab took place at 0400 when we managed to retrieve about 0.3 cubic meters of mussels with white crabs and some sediment. The Taiwanese colleagues will use these for carbon isotope analysis. Starting from 2100 we carried out the final three heat flow measurements at Formosa Ridge. This was finished at 1300 on Monday.

Monday 29 April

The heat flow measurements were interrupted by 1000 to use the TV-G at equal time spacing to allow re-charging of the batteries. We deployed the TV-G on top of the southern summit of Formosa Ridge at 1100. With the first grab we obtained a large amount of clays

with high water content and shell and carbonate fragments. The second dive yielded a large piece of authigenic carbonate.

Tuesday 30 April

During the night we collected more multi beam and PARASOUND data to complete the coverage between the two study areas. As both the W6 and the fibre optic wire had to be re-terminated in the morning this survey lasted until 1100 before we were able to collect more heat flow measurements at Four-Way-Closure Ridge. At 1500 these measurements were finished and we deployed the TV-grab at the large seep site on Four-Way-Closure Ridge. We managed to retrieve one grab full of gassy sediments below a bacterial mat and had several unsuccessful attempts at getting a large piece of carbonate for retrieving several smaller pieces.

Wednesday 1 May

From 0100 to 1200 we collected more multi-beam and PARASOUND data before taking two more TV-grabs at Formosa Ridge. As the weather had picked up again and the gravity corer weight could not be moved we had to cancel the planned gravity coring and collected a last sound velocity profile for the multi-beam data processing before sailing back to Kaohsiung.

5. Work completed and first results

5.1. 3D seismic acquisition and processing

High-resolution 3D seismic data were acquired with the P-Cable system at two study areas. The first survey was conducted at Formosa Ridge, a steep and rugged bathymetric high on the passive margin that is flanked on each side by deeply incised canyons. The second target was Four-Way-Closure Ridge, a thrust ridge system on the active margin. By acquiring 3D seismic data at both of these target areas, the aim is to be able to determine differences in gas hydrate systems that result from the influence of different tectonic settings.

5.1.1. Formosa Ridge

The P-Cable survey area at Formosa Ridge was defined to target a known cold seep on the southern summit as well as an incised canyon at the northern end of the ridge (Fig. 5.1.1.). NW-SE-striking 2D seismic profiles showed a BSR that appeared to be much shallower beneath the incised canyon than beneath the summits of the ridge. For this reason, we aimed to determine the influence of canyon incision on the gas hydrate system; how are gas hydrates adjusting to a dynamic system driven by rapid erosion? To image these regions of interest, a NW-SE-striking survey area of 10.5 km by 2.5 km (Fig. 5.1.1.) was planned with sail lines spaced 60 m apart.

We deployed a relatively long cross cable (165 m) with 14 streamers attached (Fig. 5.1.2). The outer three streamers on each side of the cross cable were spaced 15 m apart and the inner eight were spaced 10 m apart. Two spherical floats were attached to each junction box, except those at the outermost streamers (streamers 1 and 14). Additionally, single floats were tied to the cross cable between the following streamers: 5-6, 6-7, 7-8, 8-9, 9-10. These provided additional buoyancy in the centre of the cross cable where the most sag was expected. Initially, the paravanes were towed with 80 m of trawl wire rolled off the winch, but this was increased to 90 m and then finally to 100 m, in order to improve the spread of the system.

GPS receivers were attached to each paravane and to a known position on the ship for reference. Likely through a combination of the floats and the wide spread between paravanes, streamers were towed relatively shallow for most of the survey (around 1-2 m). This resulted in appreciable low-frequency noise.

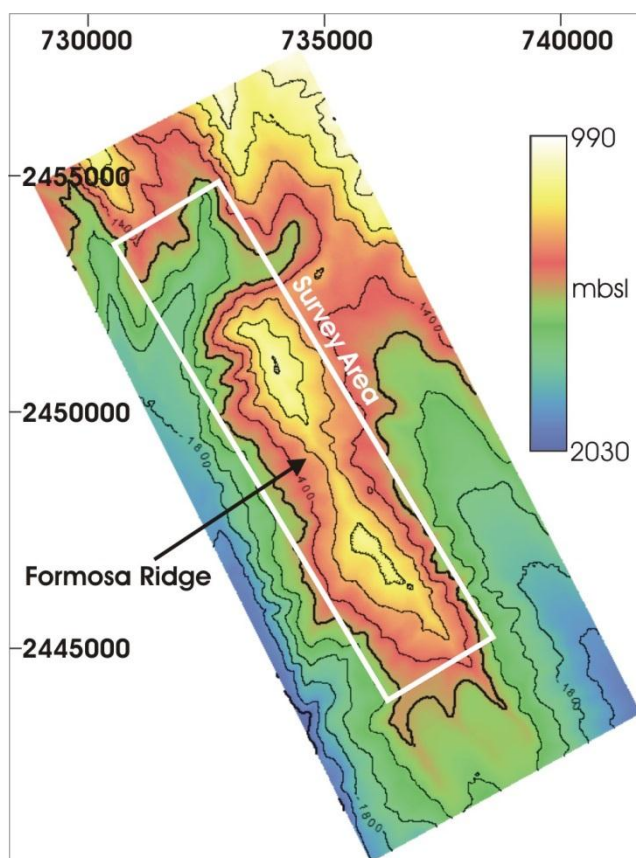


Fig. 5.1.1 Local bathymetry in the region of Formosa Ridge. Coordinates are in UTM Zone 50 N. The P-Cable survey area is annotated as the white box.

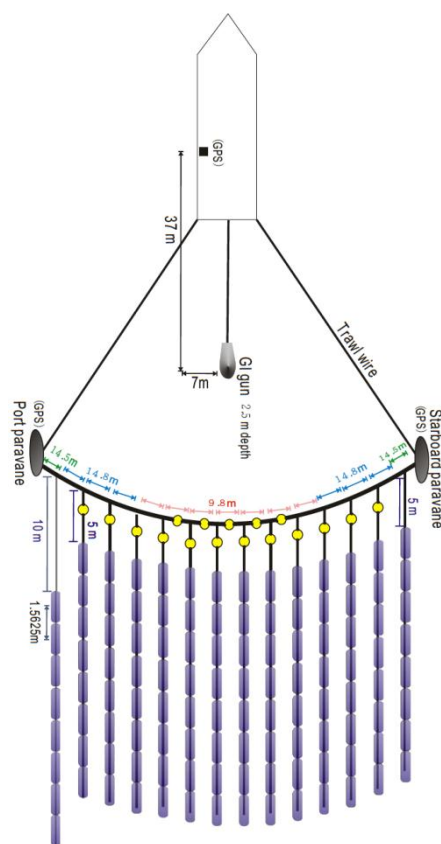


Fig. 5.1.2 P-Cable system configuration for the two surveys.

As a source, we deployed a 105/105 cu-in GI gun, which we operated without the injector during the first (Formosa Ridge) survey because the hydrophone was not working and we did not manage to correctly synchronise the injector in order to suppress the bubble pulse. The airgun was fired every 5 seconds and we recorded data for 4 seconds at a sampling rate of 1 ms. The average ship speed was 3.5 knots through the water; speed over ground varied due to currents, but not to a great extent.

On-board processing included predictive positioning of the streamers from the paravane locations under the assumption that the cross cable conforms to a catenary curve as it is towed through the water. Direct arrivals from the outermost streamers (streamers 1 and 14) were used to position the gun for every shot of the survey. Receiver locations were then adjusted from the predicted positions such that the direct arrivals at each streamer agreed with the source-receiver offsets. The source-receiver locations were then binned on a grid with 6.25 m by 6.25 m cells. Seismic traces were then balanced and filtered, before an NMO correction (with a constant velocity of 1500 m/s) and stacking were applied. The stack was then migrated in a two-pass method with a 2D Stolt algorithm (1500 m/s constant velocity model), first in the cross line direction, then in the inline direction.

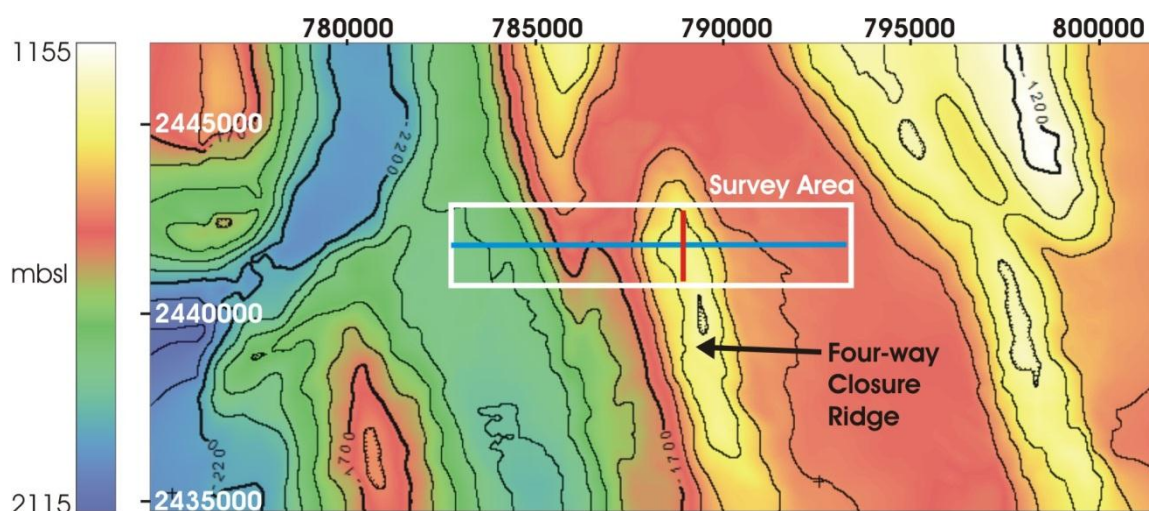


Fig. 5.1.3 Local bathymetry in the region surrounding the Four-Way-Closure Ridge study area. Coordinates are in UTM Zone 50 N. The P-Cable survey area is annotated as the white box. The E-W blue line shows the location of the in-line profile given in Fig. 5.1.11. The N-S red line shows the location of the cross-line given in Fig. 5.1.10.

5.1.2. Four-Way-Closure Ridge

The survey area at Four-Way-Closure Ridge was defined to image fluid migration patterns in the basins either side of the accretionary ridge and into the ridge itself. To this end, we planned an E-W oriented survey 10.5 km long and 2.1 km wide (Fig. 5.1.3). Sail lines were positioned at 60 m spacing to each other.

The configuration of the cross cable and streamers was the same as for the survey at Formosa Ridge (Fig. 5.1.2). However, instead of attaching two floats at the junction boxes, we only attached one float per junction box in an attempt to get the streamers to tow slightly deeper. For the amount of trawl wire paid out to the paravanes (100 m on each side), this float configuration seemed to work well. The streamers were towed slightly deeper, but still sufficiently shallow to avoid receiver ghosts in the data.

The same source was used, but for this survey the hydrophone was working and we were able to effectively use the injector to suppress the bubble pulse. As for the Formosa Ridge survey, we triggered the airgun at 5 s intervals and recorded data for 4 s at a sampling rate of 1 ms. At the beginning of the survey the average ship speed was 3.5 knots through the water, but we increased this to 3.7-3.8 knots for the bulk of the acquisition in order to ensure that we had enough tension on the cross cable to keep the streamers from towing too deep.

The data were processed according to the flow described for the Formosa Ridge survey.

5.1.3. Results of 3D seismic processing

5.1.3.1. Formosa Ridge

The ridge is characterized by extremely rugged seafloor topography, well-developed sediment wave structures, and a BSR that can be traced beneath most of the survey area. Focused fluid flow and gas invasion into the gas hydrate stability zone is particularly evident beneath the seep site on the southern summit of the ridge (Fig. 5.1.4). There is also a clear relationship

between the topography of the BSR (marking the base of the gas hydrate stability zone) and the topography of the seafloor. Positive relief structures are associated with a thick gas hydrate stability zone, whereas negative relief structures, like the incised canyon in the north of the survey area, are associated with relatively thin gas hydrate stability zones (Fig. 5.1.5). Example in-line and cross-line profiles from Formosa Ridge, with distance and two-way time annotations, are given in Fig. 5.1.6 and Fig. 5.1.7.

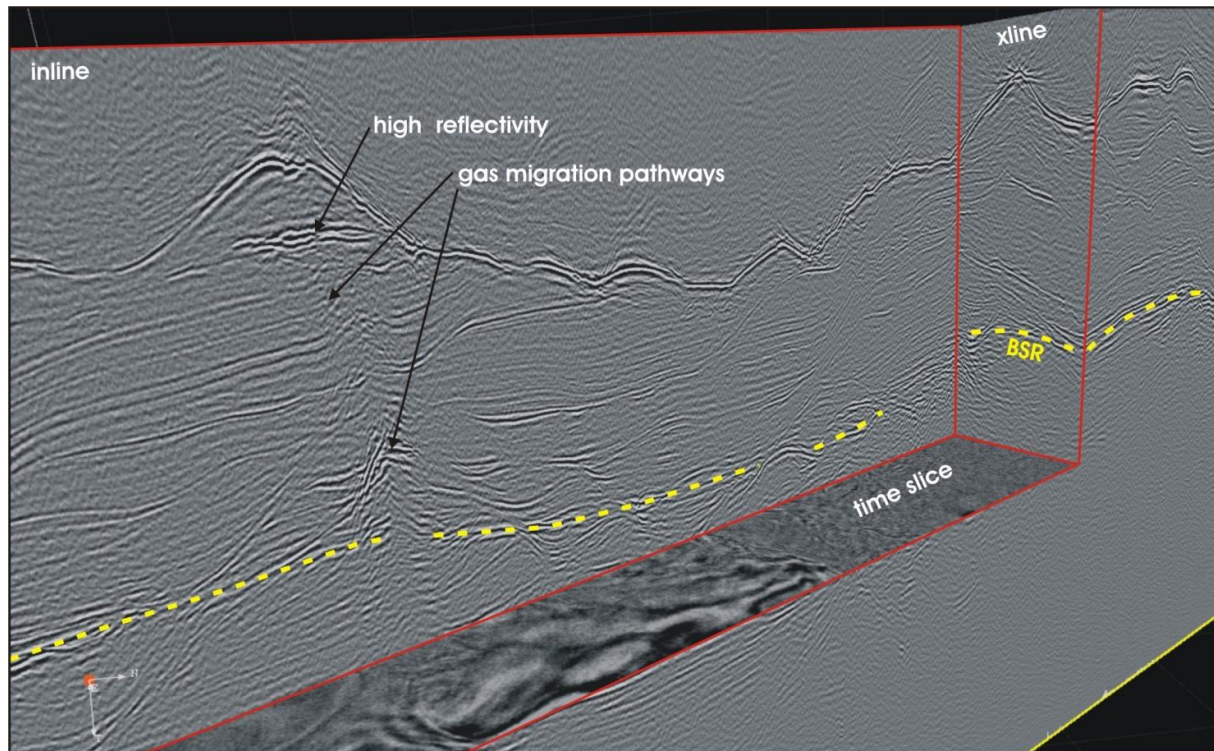


Fig. 5.1.4: 3D “chaircut” view into the 3D seismic data of Formosa Ridge in the southern part of the survey area. Annotated are: 1) the bottom simulating reflection (BSR), which marks the base of the gas hydrate stability zone, 2) gas migration pathways, which are manifested as discontinuities in the stratigraphic succession, 3) a zone of high reflectivity directly beneath the southern summit.

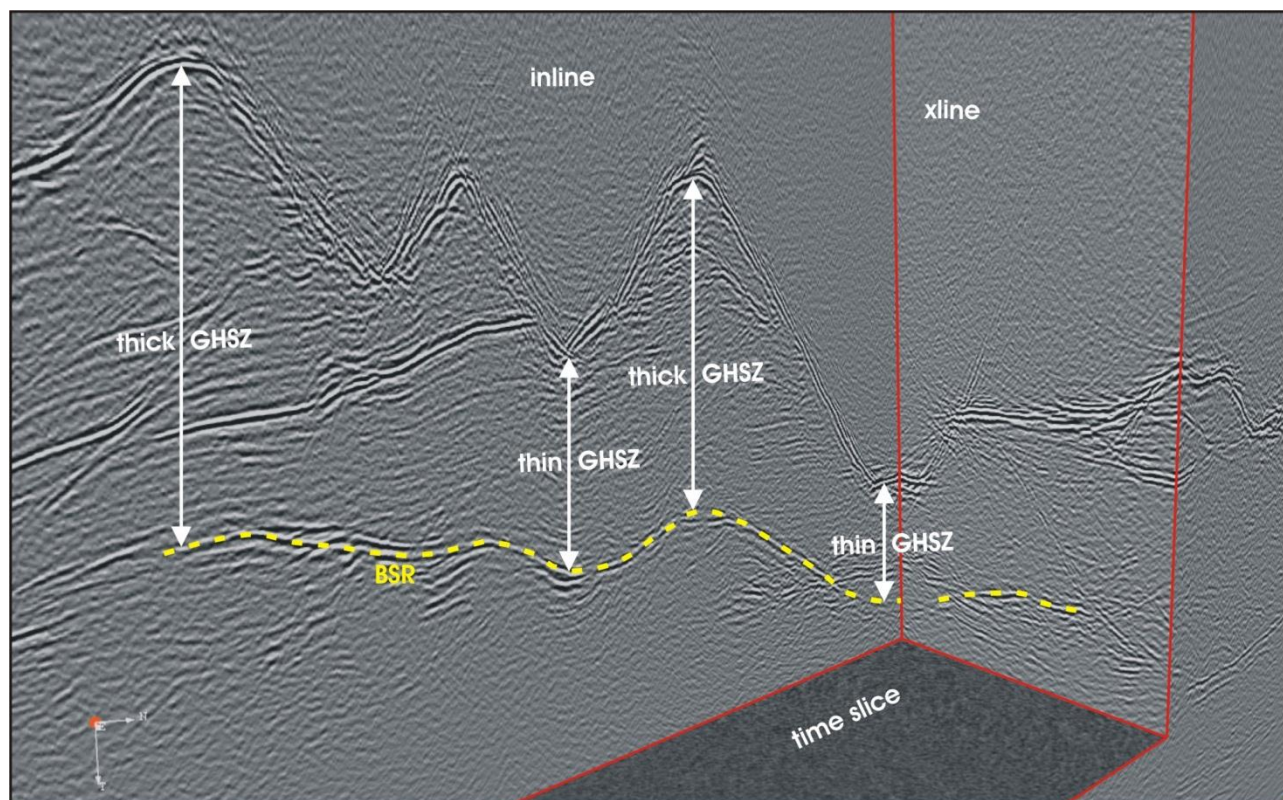


Fig. 5.1.5: 3D “chaircut” view into the 3D seismic data of Formosa Ridge in the northern part of the study area. The bottom simulating reflection (BSR) is marked by the broken yellow line. The gas hydrate stability zone (GHSZ) is relatively thin beneath topographic lows and relatively thick beneath topographic highs.

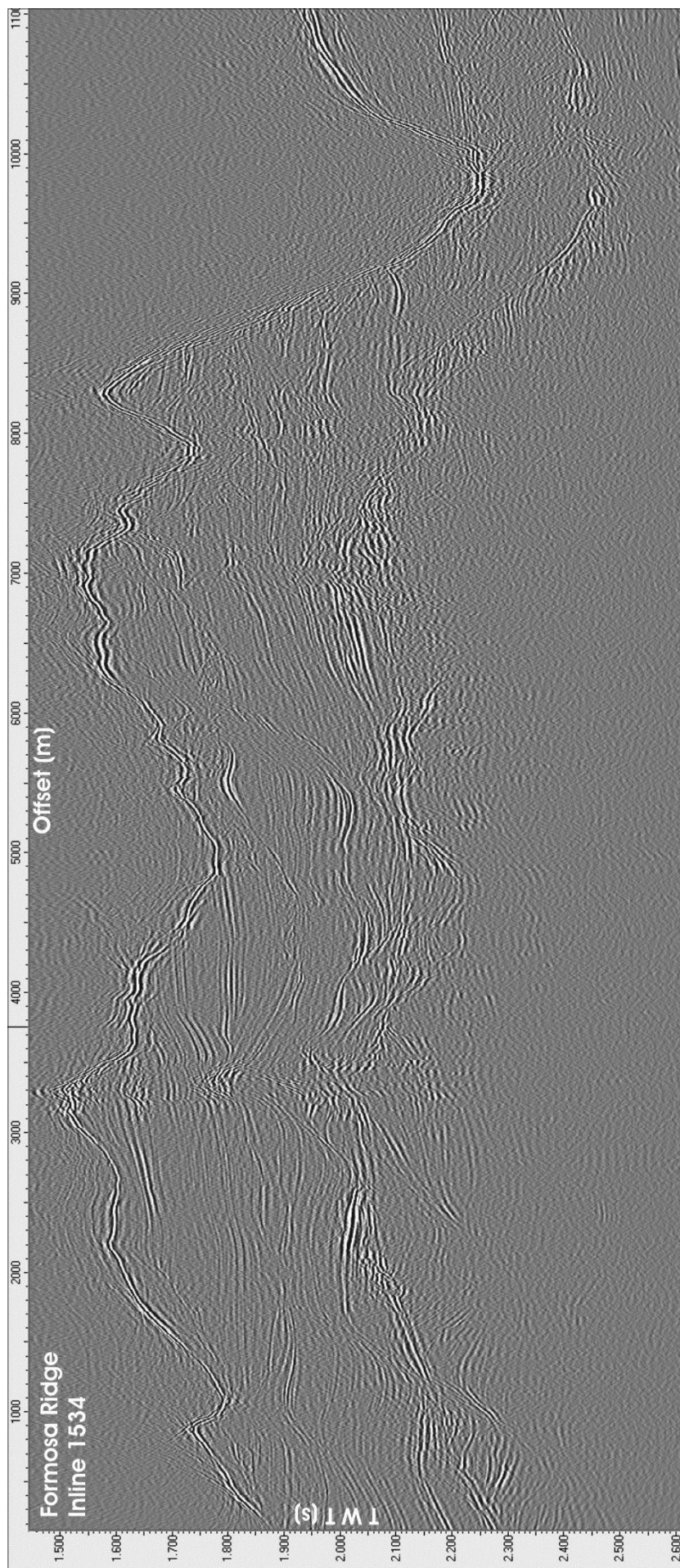


Fig. 5.1.6 Example in-line (In-line 1534) from the seismic volume acquired over Formosa Ridge.

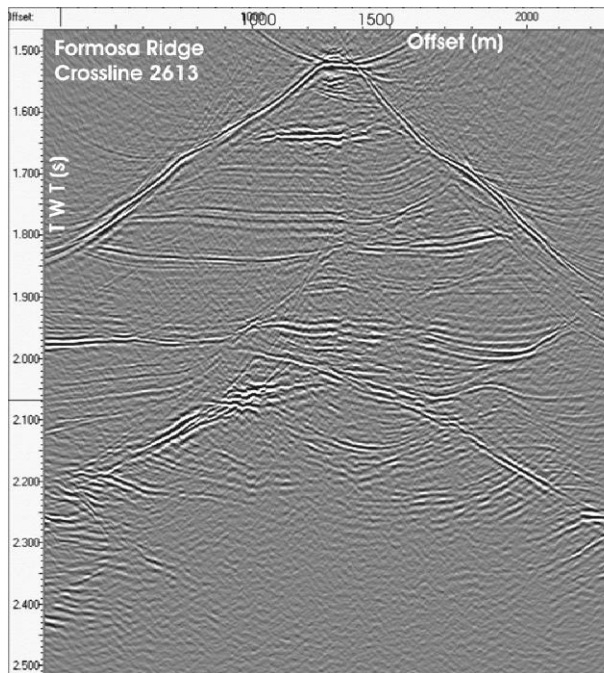


Fig. 5.1.7: Example cross-line (Cross-line 2613) from the seismic volume acquired over Formosa Ridge.

5.1.3.2. Four-Way-Closure Ridge

The Four-Way-Closure Ridge is characterised by packages of strong reflections above the BSR in the lower part of the gas hydrate stability zone (Fig. 5.1.8). Such well-developed zones of high-reflectivity immediately above the BSR were not observed beneath Formosa Ridge. East and west of the ridge, well-stratified sedimentary successions in the basins verge towards the ridge, cross-cutting the BSRs. A highly-reflective patch of the seafloor (Fig. 5.1.9) was shown to consist of massive carbonates by video observations from Hybis (see Section 5.7). Other highly-reflective patches just beneath the seafloor can be observed further west of this site; these may be buried carbonate formations from a region of seepage that is no longer active. Example in-line and cross-line profiles from Four-Way-Closure Ridge, with distance and two-way time annotations, are given in Fig. 5.1.11 and Fig. 5.1.10.

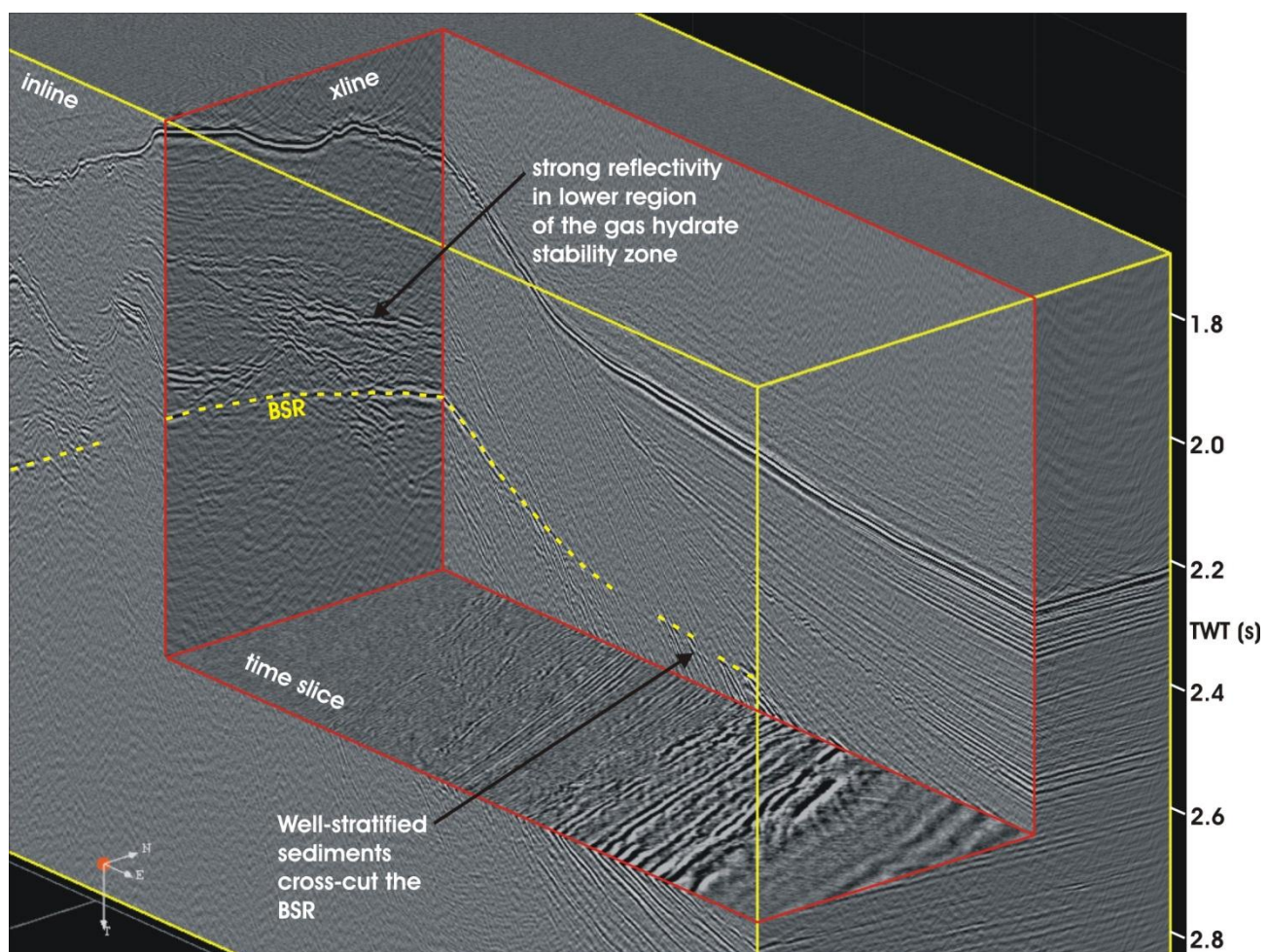


Fig. 5.1.8: 3D “chair-cut” view into the 3D seismic data of the Four-Way-Closure Ridge study area. The bottom simulating reflection (BSR) is annotated, as are strong reflections above the BSR and reflections from well-stratified sediments that cross-cut the BSR.

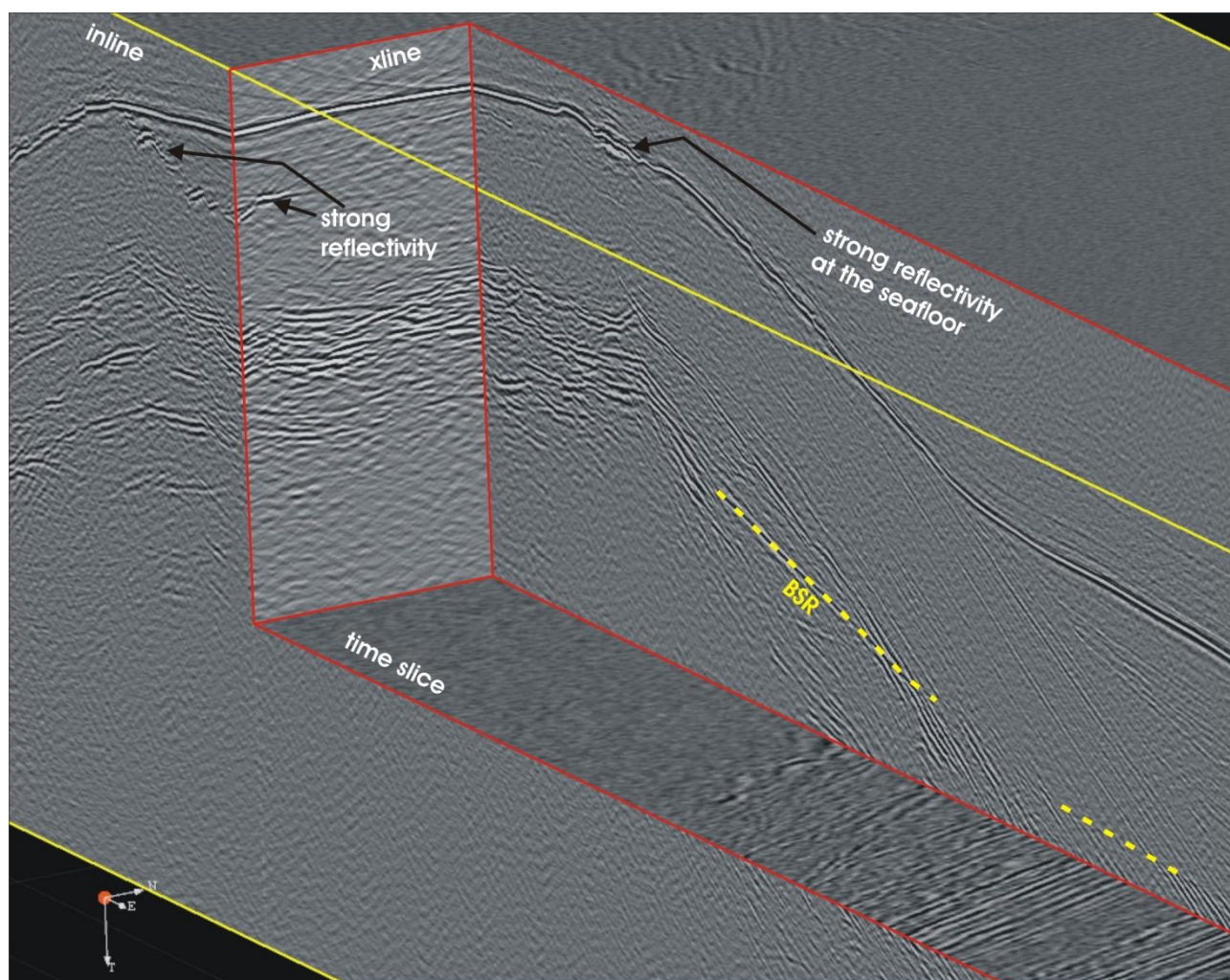


Fig. 5.1.9: 3D “chair-cut” view into the 3D seismic data of the Four-Way-Closure Ridge study area. The bottom simulating reflection (BSR) is annotated. Also annotated are: 1) a patch of strong reflectivity at the seafloor, and 2) other similar patches further west, beneath the seafloor in the upper part of the gas hydrate stability zone (to the left of the figure).

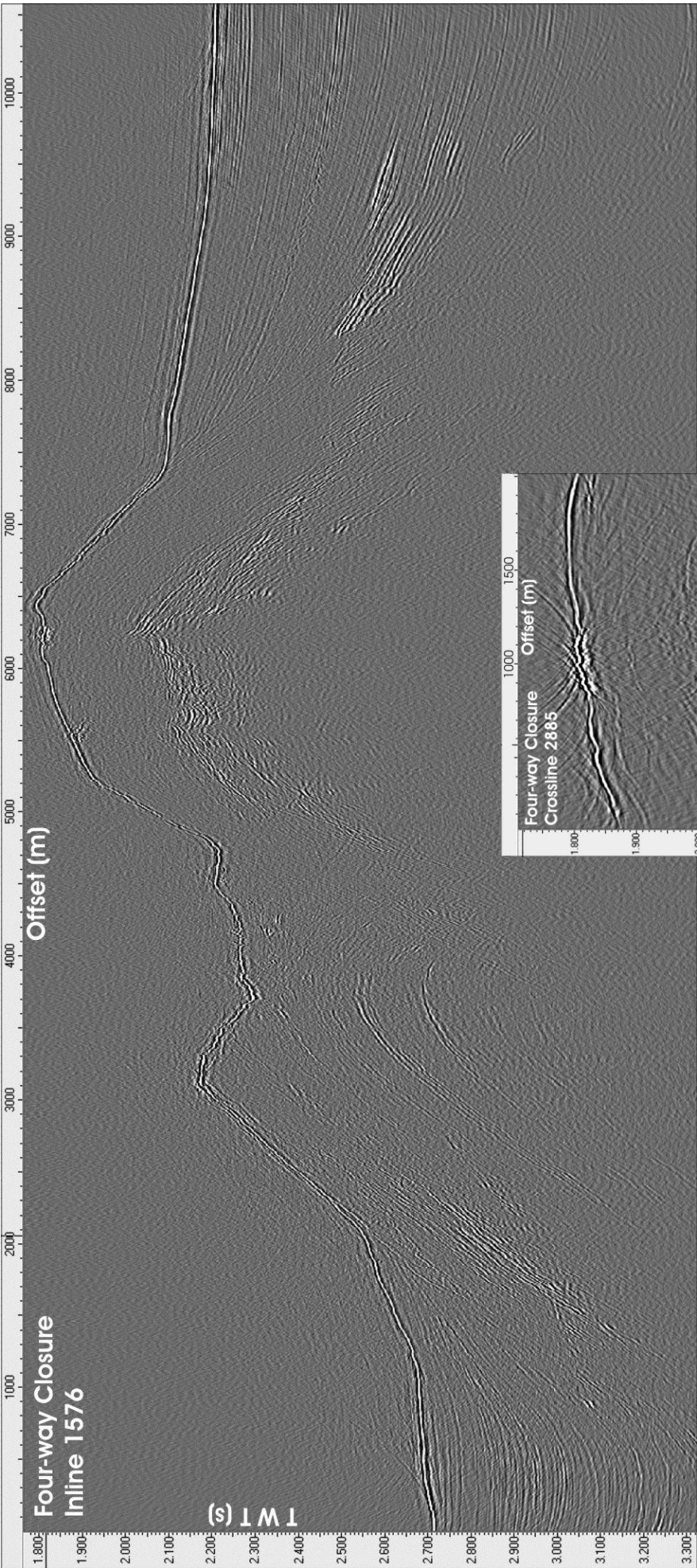


Fig. 5.1.10: (left). Example cross-line (Cross-line 2885) from the seismic volume acquired over Four-Way-Closure Ridge.

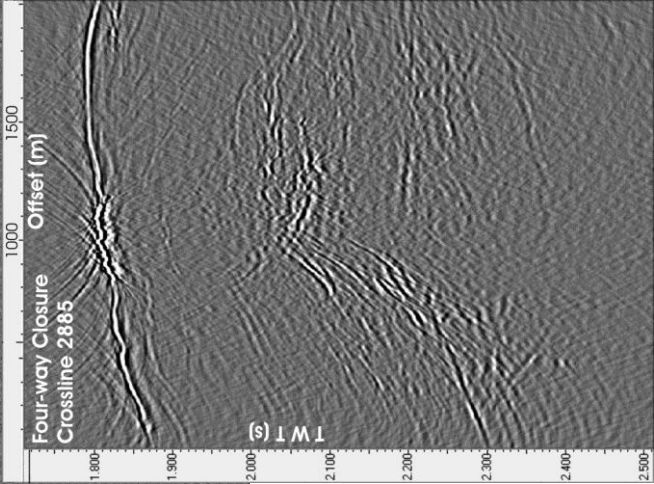


Fig. 5.1.11 (above). Example in-line (In-line 1576) from the seismic volume acquired over Four-Way-Closure Ridge.

5.2. OBS experiments

5.2.1. Objectives

The high-resolution records of ocean-bottom seismometers allow to distinguish between several petrophysical models of gas hydrate distributions in sediments and to quantify the concentration of possible free gas. Further, the velocity distribution of the seismic waves can be determined and will improve results of the seismic 3D cube. Therefore, two ocean-bottom seismometer (OBS) surveys had been carried out, one at Formosa Ridge and one at Four Way Closure.

5.2.2. Instrument description

The OBS consists of four floats connected to frame, which carries a three-component seismometer, a hydrophone and a data recorder cased in a high-pressure tube (Fig. 5.2.1). The sensors are connected to the recording unit, which continuously records the signals of the sensors. The systems itself would float at the sea surface, so in order to deploy it at the ocean bottom a weight is mounted to the frame with a releaser unit. The releaser has an acoustic communication unit, which can be addressed from the ship in order to disconnect the weight after the experiment. The OBS will then ascend to the surface and can then be recovered. A flashlight, a radio transmitter and a flag are attached to the frame in order to facilitate sighting the OBS. While the OBS measures seismic signals an additional data logger continuously records the shot times.

The data recorders have to be programmed before the deployment of the system. The sample rate of the OBS recorders was set to 500 Hz at the first site, the Formosa Ridge, while the data logger recorded at a sample rate of 1000 Hz. The gain of the input channels was set to 21 to 23 for the three geophone components and 5 to 7 for the hydrophone. The recorder was equipped with one 1 GB and two 2 GB flash cards. The exact recording parameter for the deployments can be found in Appendix 3. The recording units were synchronized with a GPS signal before as well as after the recording period in order to correct the drift of the logger's internal clock.

5.2.3. Experiment design

Twelve OBS stations were deployed on 5. April 2013 in an area where Taiwanese colleagues already deployed six OBS instruments (Fig. 5.2.2). Therefore, the OBS locations were chose in a way that both OBS surveys complement each other. Fig. 5.2.3 shows an arbitrary seismic line through the 3D cube along the OBS deployment. The instruments were recovered 5 days later on 10. April 2013. A few days later the Taiwanese OBS were recovered but two of them could not be found.

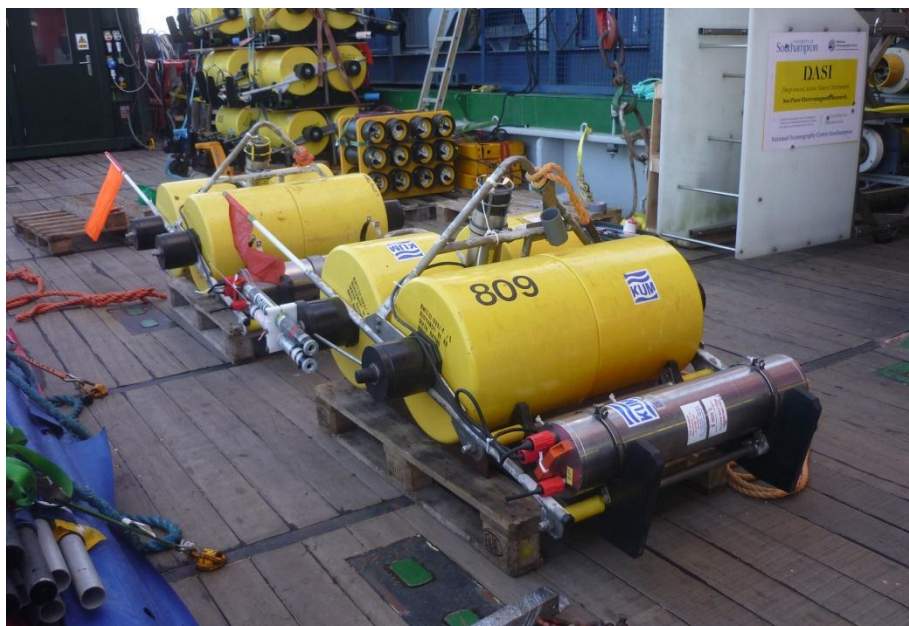


Fig. 5.2.1: Ocean-bottom seismometer prior to deployment.

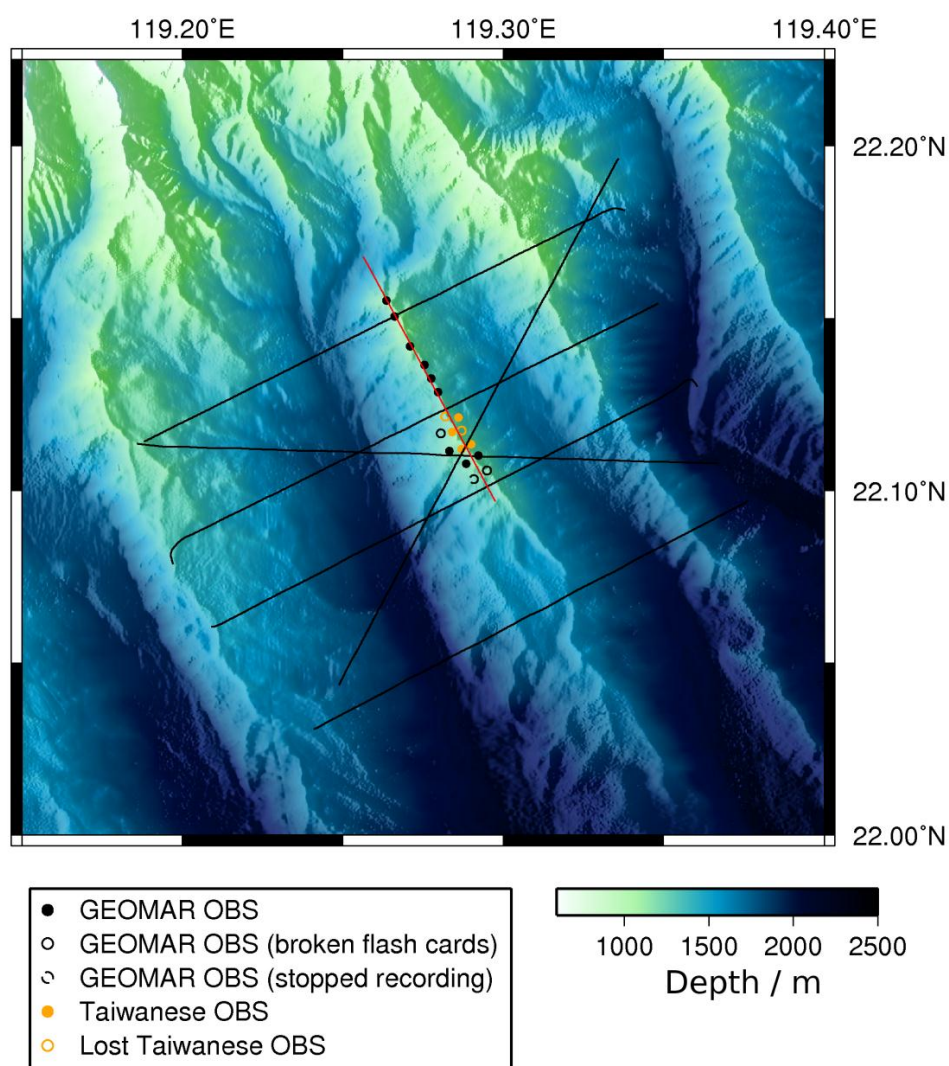


Fig. 5.2.2: Map of OBS locations at Formosa Ridge. Black lines are OBS shooting Profiles. The red line is the arbitrary seismic line through the 3D cube shown in Fig. 5.2.3.

Six OBS units recorded data and did not show any error messages after recovery and synchronization. 4 OBS showed error messages due to low battery but for three of them the error occurred at time of recovery. This does not have any effect on the recorded data. The other OBS stopped recording on 8. April 2013 but still contains the OBS-shooting profiles while two days of 3D-seismic shooting are missing. In two recorders some flash cards failed. While for one recorder two flash cards contained data and the third one was not readable, for the second OBS no data at all could be copied from the flash cards. However, there still may be a chance to read some data from the broken flash cards back home in Kiel with special tools.

At the second site, the Four Way Closure, again, twelve OBS stations were deployed for five days from 19. April 2013 to 24. April 2013 (Fig. 5.2.4). An arbitrary line through the seismic 3D cube along the OBS instruments is shown in Fig. 5.2.5. The gain for the four channels was the same as at the Formosa Ridge while the sampling rate was increased to 1000 Hz in order to increase the resolution. This time only two recorders showed error messages due to low battery. However, one error occurred after the recovery and the other one about 13 hours prior to the recovery and after the shooting of OBS as well as 3D seismic profiles was done. Therefore, the errors did not have an effect on the data and there is no data loss at the Four Way Closure site.

5.2.3. Preliminary results

Data conversion on a few OBS for both sites was carried out on board and shows good wave forms of the vertical components as well as the hydrophone component while the horizontal components show some noise. Detailed processing will be carried out after the cruise.

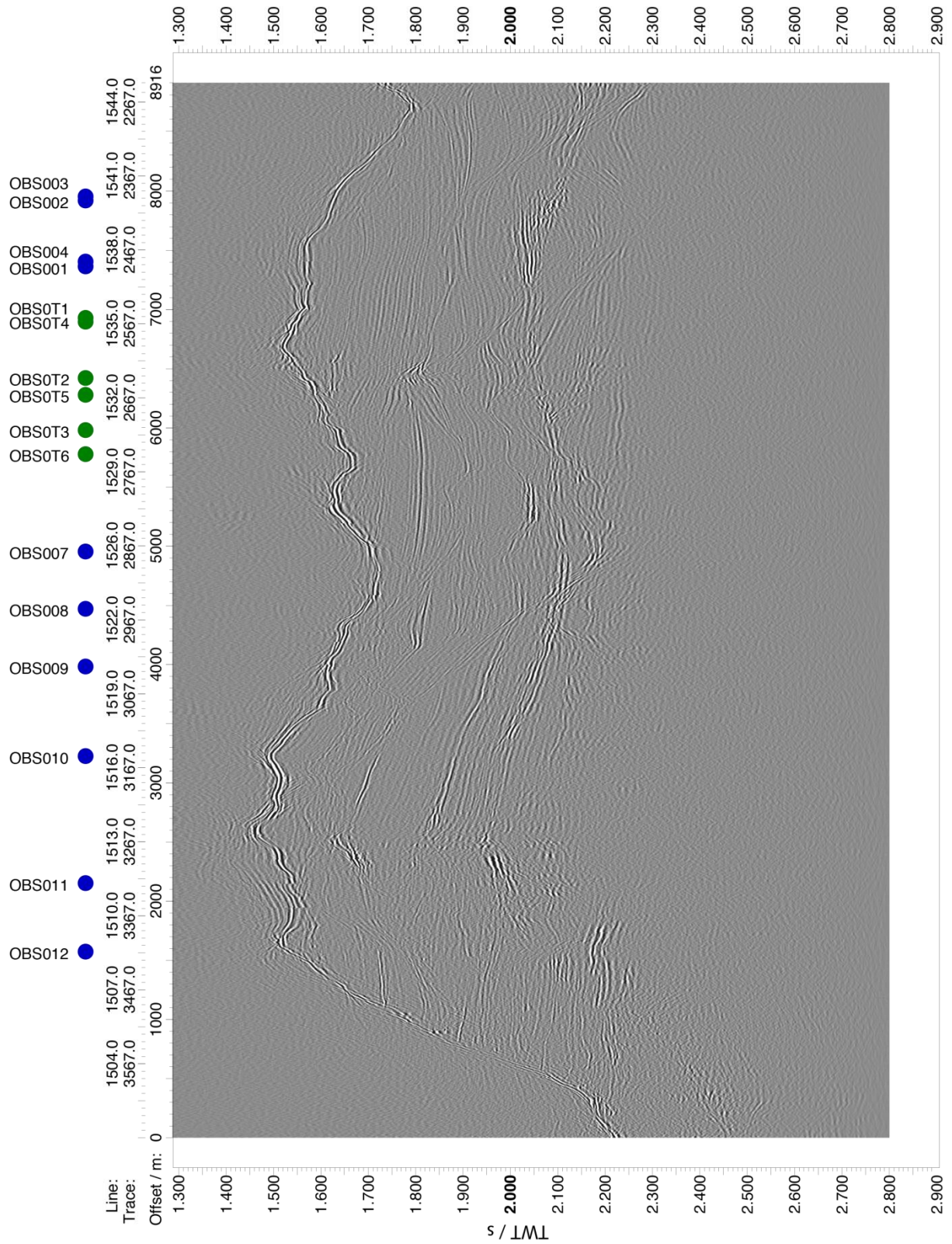


Fig. 5.2.3: Arbitrary seismic line through the 3D cube. Blue are projected locations of GEOMAR OBS and green locations of Taiwanese OBS.

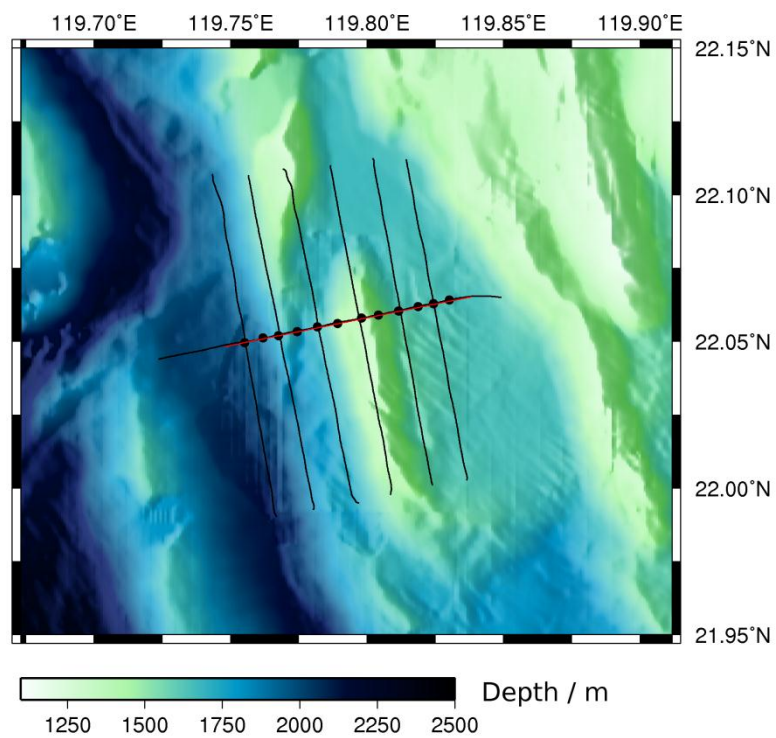


Fig. 5.2.4: Map of OBS locations at Four Way Closure (black dots). Black lines are OBS shooting profiles, the red line is the arbitrary seismic line through the 3D cube shown in Fig. 5.2.5.

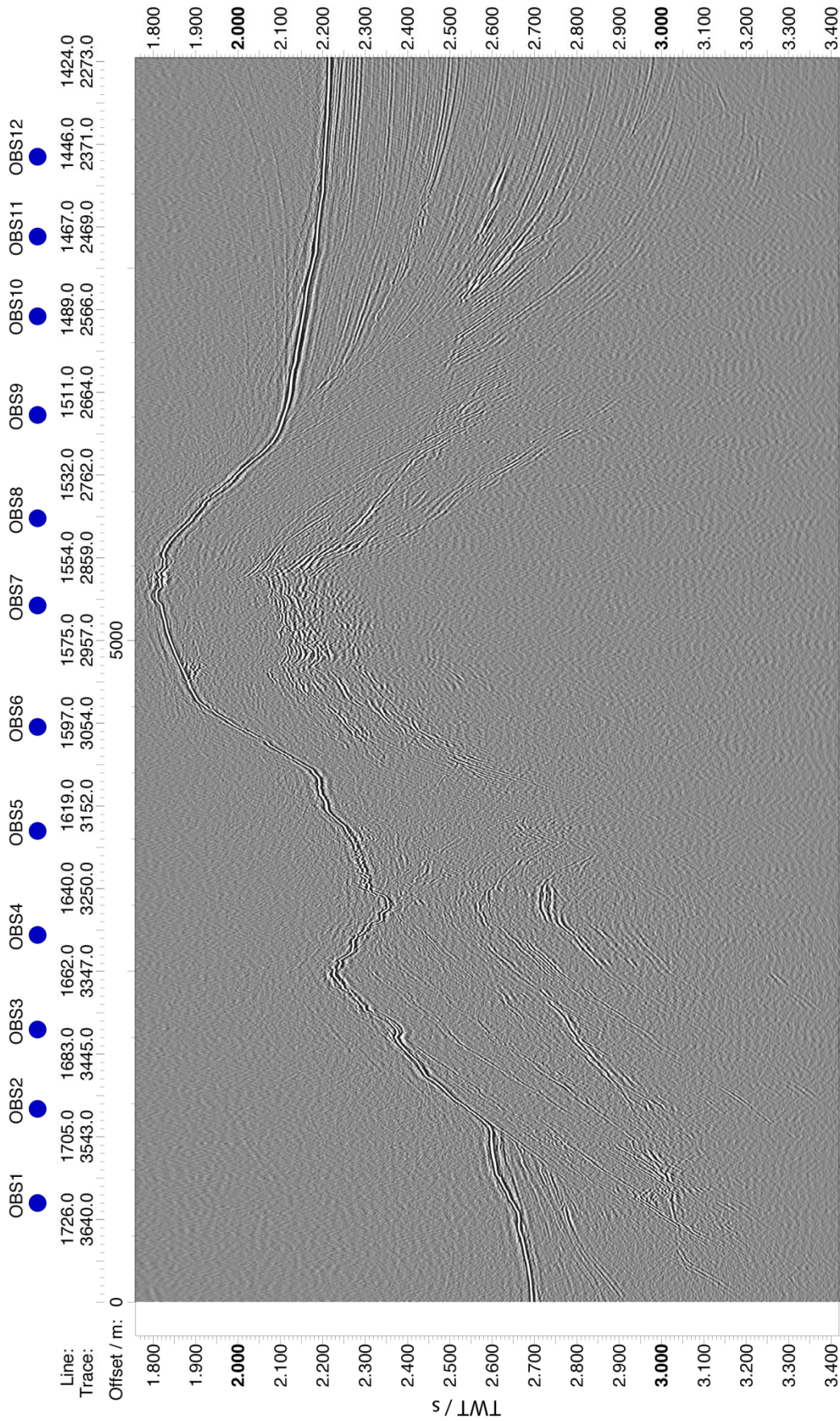


Fig. 5.2.5: Arbitrary seismic line through the 3D cube. Blue dots are projected locations of the OBS.

5.3. Controlled source electromagnetic surveys

5.3.1. Overview over the experimental setup of the electromagnetic (EM) surveys at Formosa Ridge and Four-Way-Closure

Electromagnetic measurements determining the electrical resistivity of the seafloor were carried out concurrent with 3D seismic data in two regions, the Formosa Ridge and Four-Way-Closure (Four-Way-Closure Ridge). Electrical resistivity, which is sensitive to the type and amount of pore space fluid, increases rapidly with increasing gas or methane hydrate concentration replacing the conductive salt water in the pore space (Fig. 5.3.1: Dependency of electrical resistivity on gas or gas hydrate saturation of the pore space, shown for rock porosities of 30%, 50% and 70%). The values have been calculated using Archie's law (Archie, 1942 with coefficients of $a=1.4$, m and n of **1.76**). It has therefore an increased sensitivity towards hydrate and gas saturations compared to seismic data, but at the same time lacks the structural resolution of seismic data. To harvest the maximum amount of information from the geophysical data sets, we therefore intend to invert the data jointly to a common Earth model.

The electromagnetic experiment carried out consists of a time domain controlled source electromagnetic approach (CSEM). We employ an electric dipole transmitter (Sputnik) connected through a 18 mm coax cable to the ship, which generates a square wave signal on the seafloor through a 10 m dipole. 12 stationary electromagnetic receivers (OBEM) are deployed prior to the experiment and measure electric field changes at a sampling frequency of 10 kHz. While the receivers are stationary, Sputnik is placed on the seafloor, undergoes one transmission cycle, and is then raised approx. 50 m above the seafloor and moved to the next transmission point. The diffusion time of the signal from transmitter to receiver as well as the amplitude of the received signal depend on the resistivity of the seafloor. Vertical resolution is achieved through measuring the response at different distances as well as over a longer time scale. Additional resolution may be derived from measuring the response to different polarization modes. For this reason both the transmitter as well as the receivers transmit and receive the electric fields in orthogonal directions.

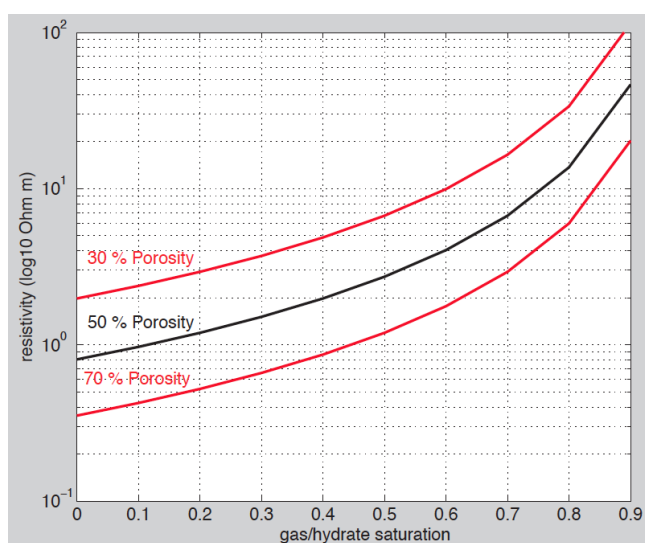


Fig. 5.3.1: Dependency of electrical resistivity on gas or gas hydrate saturation of the pore space, shown for rock porosities of 30%, 50% and 70%. The values have been calculated using Archie's law (Archie, 1942 with coefficients of $a=1.4$, m and n of 1.76).

Fig. 5.3.2 and Fig. 5.3.3 show the Sputnik transmitter as well as the Geomar OBEM receivers. The transmitter is capable of injecting square waves with different amplitudes into

the seafloor ranging from 10 A up to 50 A. With a 10 m dipole length this translates to distance of reach on the order of 800 m (depending on seafloor resistivity) and therefore the experiment has a depth of penetration on the order of 300 m. To maintain sufficient power, the instrument is equipped with lead battery pack with an output power of 48 V, which are charged through the coax-cable at a Voltage of 400 V. For accurate time keeping the transmitter is equipped with a high precision Seascan clock, which is synchronized before and after the experiment. The transmitter is driven through a Firefox Linux based microcontroller, which can be accessed through DCHP modem connection through the coax cable. The transmitted waveform is logged onto a USB drive and downloaded through the modem connection onto the ship during movement to the next transmission station. The placement onto and lift from the seafloor is monitored through a little camera situated at the bottom of the transmitter and through an acoustic altimeter. From a mechanical point of view, Sputnik has been designed to fold up the arms vertically when hanging by its own weight on the cable to facilitate deployment as well as moving of the transmitter. When the Sputnik is placed on a surface the arms unfold reaching their 10 m horizontal dipole length. The inclination of the arms is a parameter, which is also logged during the operation.

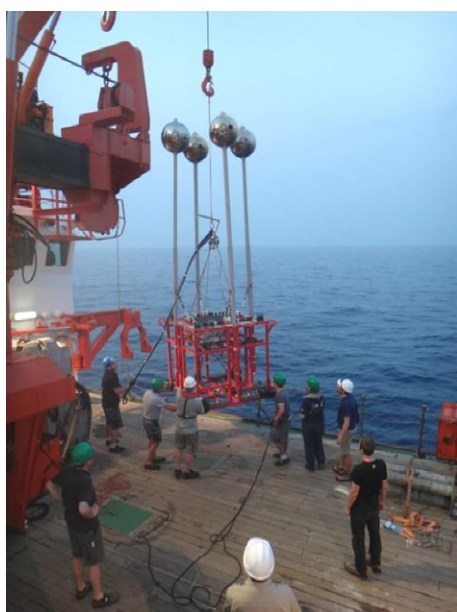


Fig. 5.3.2: Left: Sputnik electric dipole transmitter. Right: Geomar OBEM receiver.

The Geomar OBEM receivers have a twofold function. During the CSEM transmission they record electric field waves at 10 kHz, and during other times the natural source electric and magnetic signal at a frequency of 10 Hz are recorded and complement the CSEM data with a magneto-telluric data set which sheds light on temperature and fluid flow at greater depth, alas with less resolution. The type of signal to be recorded can be chosen by sending a CSEM/MT acoustic signal from the ship to the receiver unit. While the electronics and magnetic field sensors have been developed by Magson, Berlin, the instrument frame has been designed and constructed by Geomar in collaboration with KUM, Kiel. The instruments can be deployed free falling, however, in order to have accurate positioning for the CSEM experiment, they have been lowered on a cable 50 m above the seafloor on a Posidonia releaser. The receivers remain on the seafloor until the anchor is released through an acoustic signal to the releaser, which hold the anchor onto the otherwise positively buoyant instrument. Additional relative navigation accuracy between receiver and transmitter is achieved through an internally developed short baseline type of a navigation system. For this purpose Sputnik has been equipped with four transducers. The transducers on Sputnik are used to send an

interrogation pulse to the seafloor receivers, which in turn answer at different pre-set frequencies. The time of flight of the acoustic signal as well as directional phase shifts are recorded by the transducer heads allows accurate positioning between transmitter and receiver units to a precision of a 1 to 3 m.

5.3.2. Formosa Ridge Survey

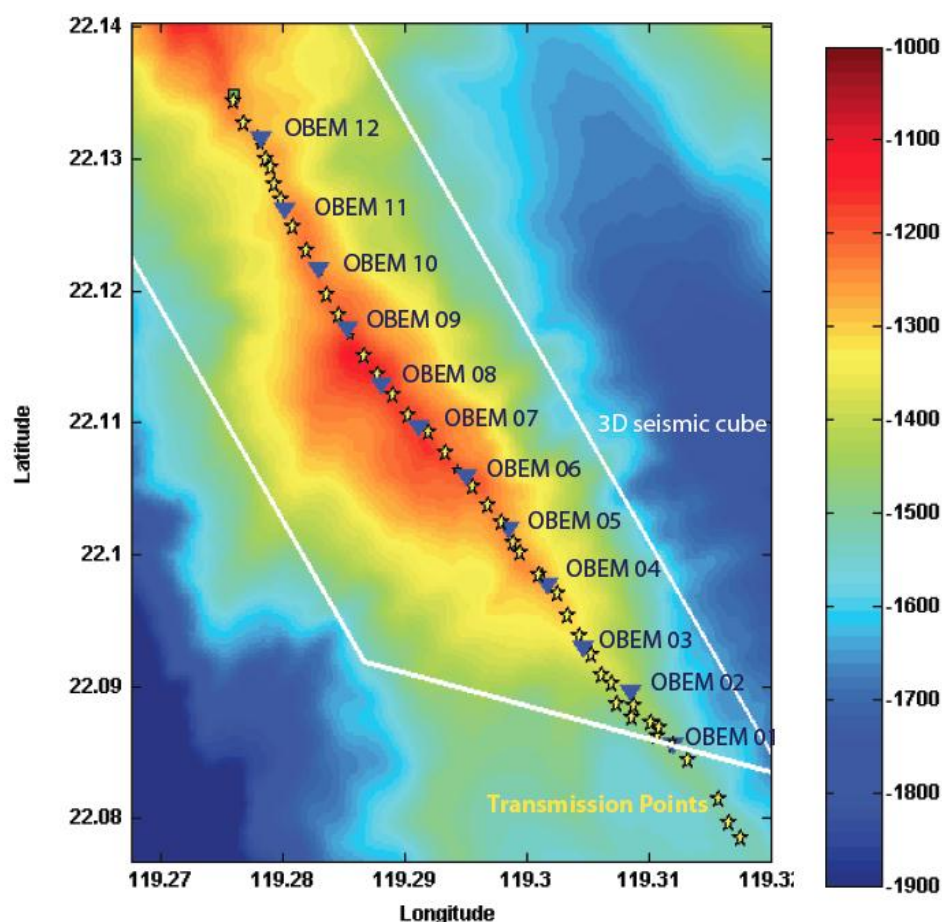


Fig. 5.3.3: Survey layout Formosa Ridge. OBEM profile length is about 7 km.

Fig. 5.3.3 shows the lay out of the Formosa survey. Twelve OBEM receivers have been placed along a profile at the centre of the 3D seismic cube of the Southern Ridge, where seep activity has been observed at the summit. Along the profile altogether 45 transmission cycles have been completed between April 17th 00:11 to April 18th 2013 04:11. Transmission at each point included a 50 A waveform subsequently emitted in both dipole directions as well as a 20 A waveform (to avoid saturation of the amplifiers in nearby receivers). The transmitted waveforms as well as the inclinometer data on the four dipole arms and on the frame have been logged continuously. At each position all receivers have been pinged twice for navigation purposes and the travel time have been recorded. Fig. 5.3.4 shows an overlay of the EM profile onto the shipboard processed 3D cube data along the profile. Unfortunately OBEM11 and OBEM12 failed to switch into CSEM modus and therefore recorded magneto-telluric data only. Due to the strong topography along the profile and much higher slope than anticipated slope angles along the profile, the data acquisition proved to be rather challenging but could be completed successfully.

OBEM #	Lat	Long
OBEM01	22.0855	119.3120
OBEM02	22.0895	119.3070
OBEM03	22.0897	119.3026
OBEM04	22.0975	119.3013
OBEM05	22.1020	119.2979
OBEM06	22.1060	119.2948
OBEM07	22.1095	119.2913
OBEM08	22.1130	119.2878
OBEM09	22.1174	119.2853
OBEM10	22.1218	119.2823
OBEM11	22.1259	119.2796
OBEM12	22.1315	119.2780

Table 5.3.1: Deployment coordinates of the OBEM receivers on Formosa.

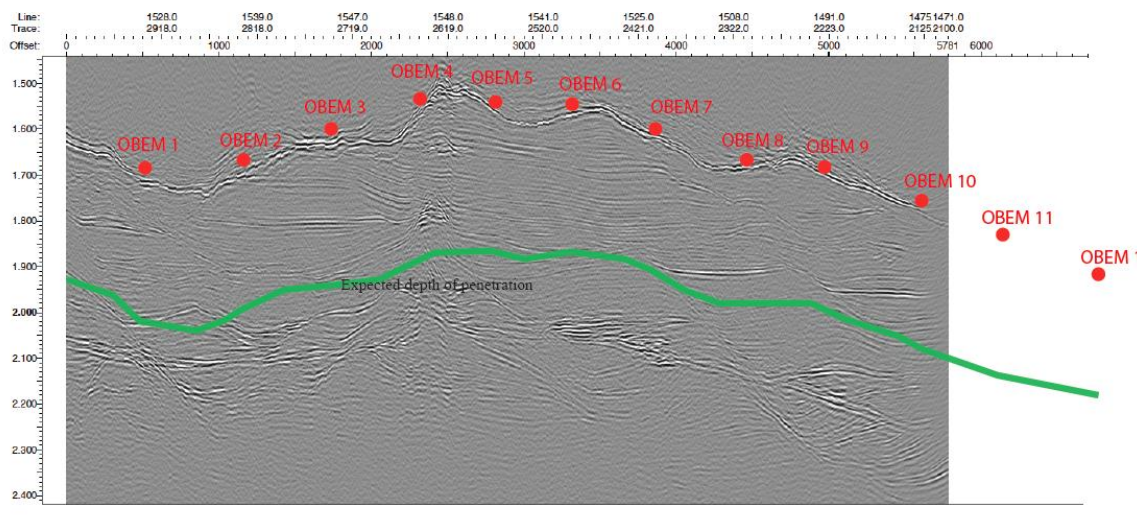


Fig. 5.3.4: Overlay of OBEM position on Formosa Ridge on onboard processed p-cable data. Red dots mark the OBSEM positions, the green line the approximate depth of penetration of the CSEM signal. The BSR is observed at a travel time of approximately 2200 msec underneath the summit.

Example Data:

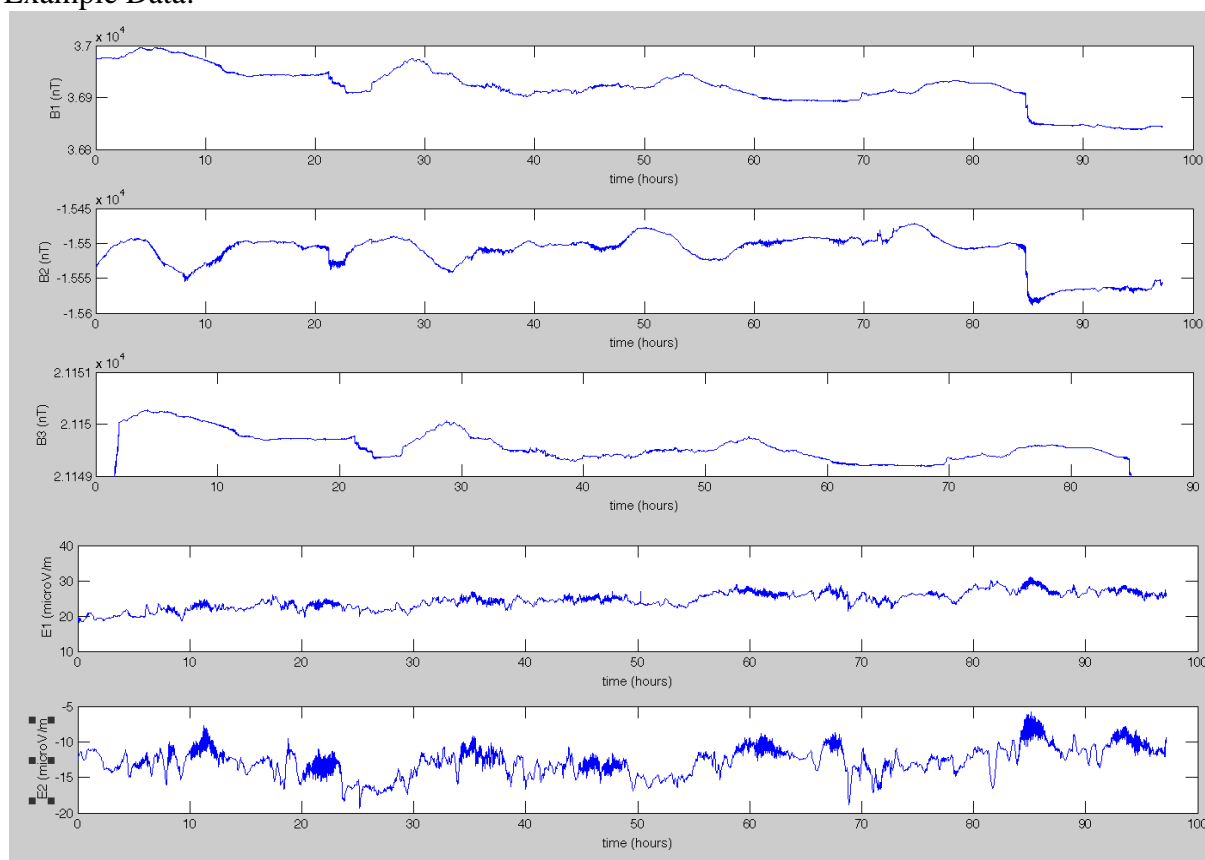


Fig. 5.3.5: Magnetic fields variations (B_1 and B_2 are orthogonal horizontal fields, B_3 vertical fields) and orthogonal electric field variations at station 9. The data has been resampled from the original 10 Hz sampling frequency to .1 Hz. Start date 21:48:12 April 12th, 2013, end date 23:01:25 April 16th 2013.

Exemplarily for the Formosa region, we present the natural source (magneto telluric) data that has been sampled at a frequency of 10 Hz during the time that the instrument has not been switched into CSEM mode. Examples of CSEM data will be presented for the Four-Way-Closure Ridge survey. Fig. 5.3.5 shows the measured magnetic and electric field variations at station 9. While the magnetic field data is of high quality, the electric field data exhibits some noise, most likely through strong bottom water current which forces the electric dipole arm movements. Fig. 5.3.6 depicts the derived apparent resistivity and phases for the raw, un-rotated magnetotelluric data at station 9. While the responses are not fit for an interpretation yet, they indicate that coherent responses may be derived in a period range from 50 to 20 000 sec, which corresponds to a depth of penetration of approximately 15 to 20 km. Generally there is a trend of increasing resistivity with depth indicating the presence of less porous sediments and basement at depth.

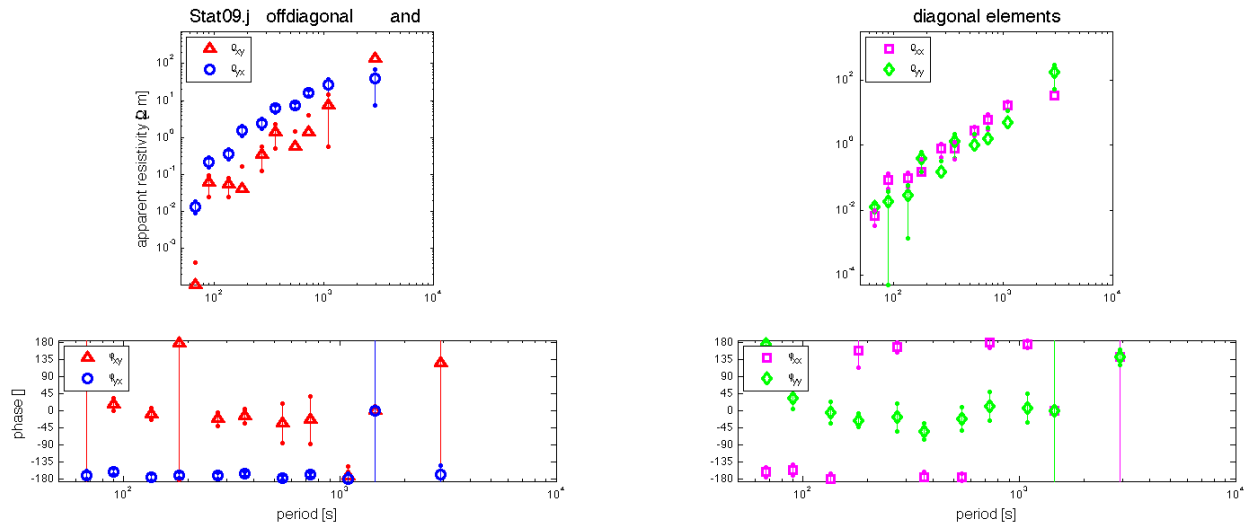


Fig. 5.3.6: Ship board preliminary processed magneto telluric data of station 9. The data has neither been rotated to strike nor remote referenced. While amplitudes and phases are unreliable at this processing stage, an increase in resistivity with period is observed indicating a decrease of fluid filled pore space and basement at greater depth. Given the coherency of the data, a depth of penetration of about 20 km can be expected.

5.3.3. Four-Way-Closure Ridge Survey

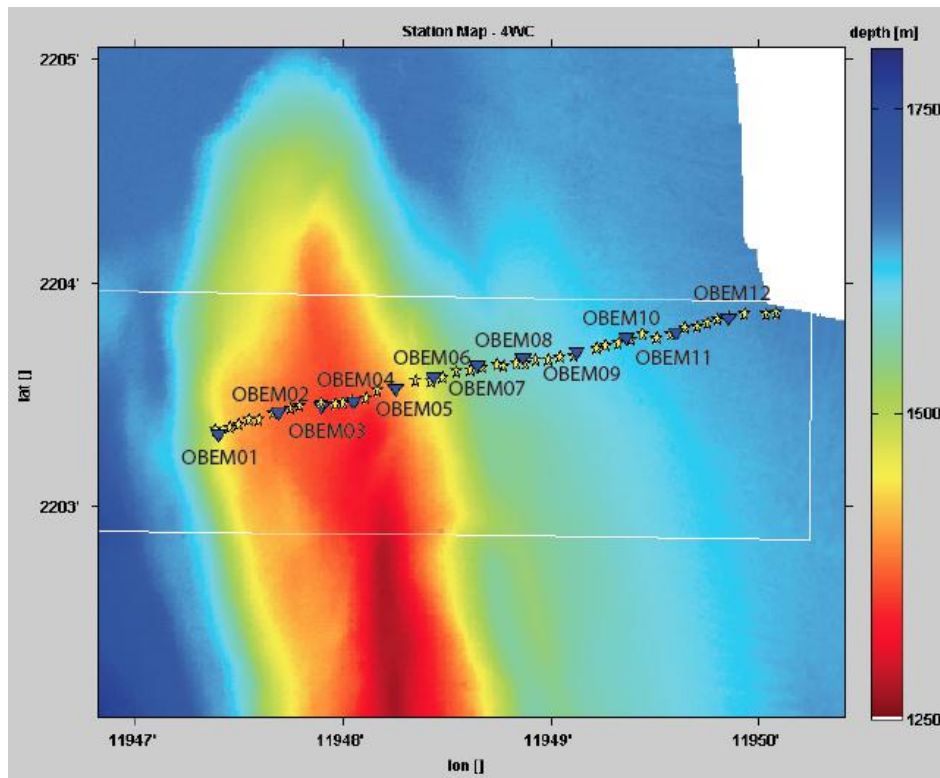


Fig. 5.3.7: OBEM and transmission points of the Four-Way-Closure Ridge survey.

OBEM #	Lat	Long
OBEM01	22.0555	119.7900
OBEM02	22.0570	119.7947
OBEM03	22.0575	119.7982
OBEM04	22.0580	119.8010
OBEM05	22.0588	119.8041
OBEM06	22.0597	119.8073
OBEM07	22.0606	119.8108
OBEM08	22.0609	119.8144
OBEM09	22.0616	119.8187
OBEM10	22.0619	119.8227
OBEM11	22.0630	119.8267
OBEM12	22.0640	119.8309

Table 5.3.2: Deployment coordinates of the OBEM receivers on Four-Way-Closure Ridge.

As for the Formosa station, 12 OBEMs have been deployed in the seismic cube (see Fig. 5.3.7 and Fig. 5.3.8). The focus of the experiment is to compare hydrate saturations on the summit and in the basin of the topographic structure. Due to the less steeper topography, we have chosen to focus on the western basin as the comparative site. The direction of the approximately 4.5 km long profile is diagonal across the seismic p-cable cube, perpendicular to geological strike direction and along the OBS profile. Due to an improvement on the mechanical opening mechanism of the Sputnik transmitter, the arms unfolded properly at all transmitter stations even at large inclinations and the transmitter profile could be finished in about 28 hours between April 24th 06:56 to April 25th 2013 10:38. Also, all OBEM receivers switched properly into the CSEM modem and recorded, after first sighting good quality data. An example of the data acquired is shown in Fig. 5.3.9. It depicts the transmitted waveform in one polarization mode in the bottom panel and the received signal at the two orthogonal dipoles at OBEM 3 in the top two panels. The transmission point is situated in close proximity of the station.

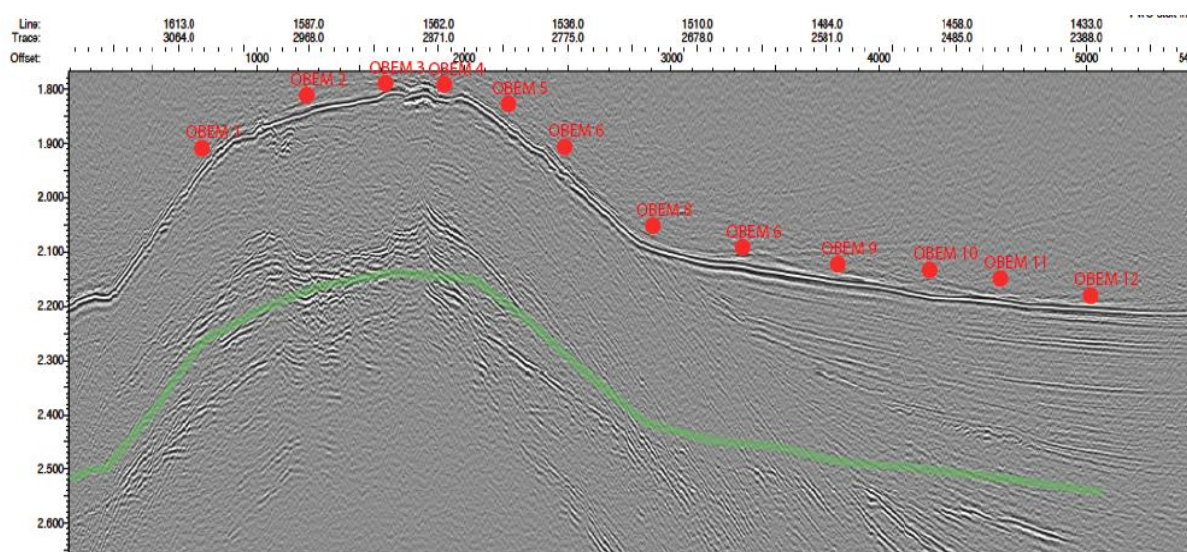


Fig. 5.3.8: Overlay of OBEM position on Four-Way-Closure Ridge on onboard processed p-cable data. Red dots mark the OBEM positions, the green line the approximate depth of penetration of the CSEM signal. The BSR is observed at a travel time of approximately 2300 msec underneath the summit.

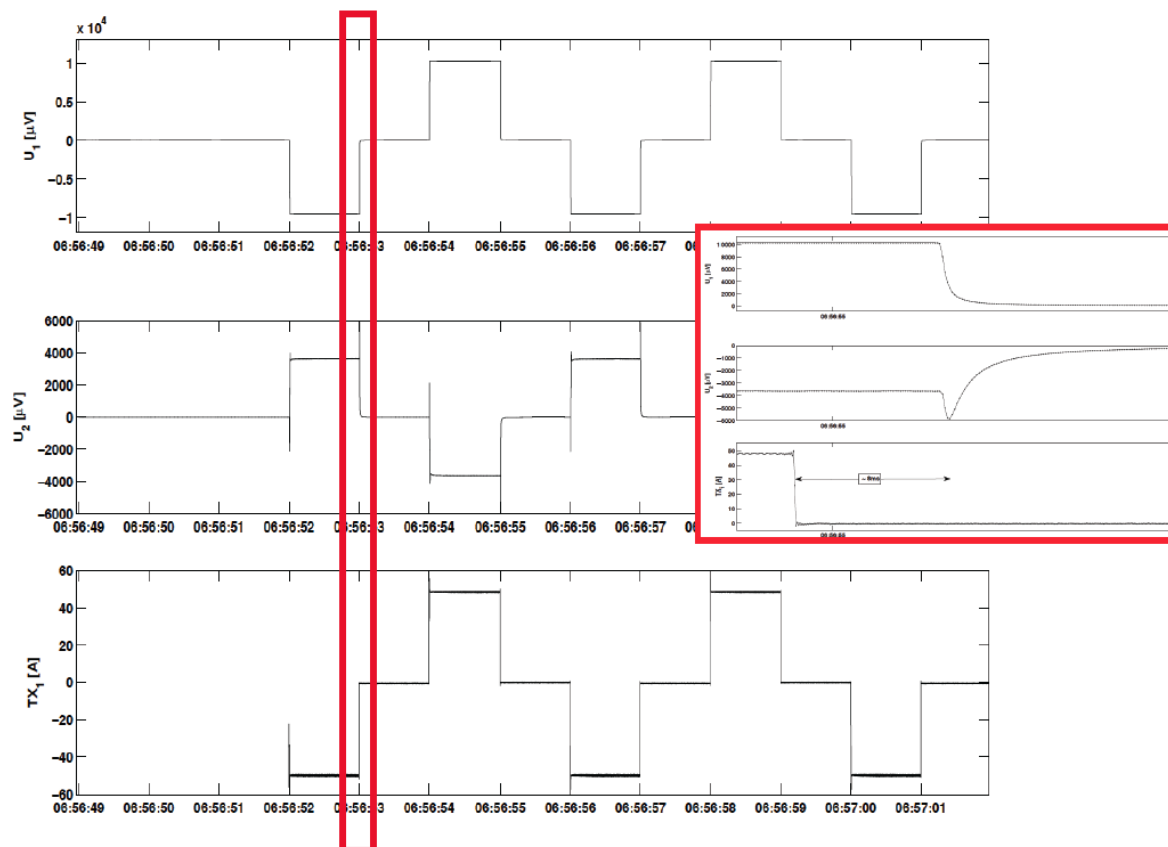


Fig. 5.3.9: Data example of the transmitted current wave form in one dipole polarization (bottom panel) and the received signal at OBEM 3 at both orthogonal dipoles (top two panels). The transmission point was in close proximity to the receiver position. Insert shows a zoom in of the first transmitted and received transient.

The transients are clearly visible in the receiver data and a zoom in on a single transient shows high quality data. The signal could clearly be observed to a distance of approximately 700 m, such that we expect a depth of penetration of the experiment to approximately 200 to 300 m. Since the knowledge of the exact distance between transmitter and receiver is crucial for high quality data and quantitative hydrate concentration estimates, a ranging between transmitter and all receivers has been carried out at each transmission point. An example of the data recorded is shown in Fig. 5.3.10. It depicts the reply signal from the receivers (reply frequencies are varied for different receivers to facilitate identification) at the four transducers on Sputnik after an interrogation ping. The right hand panel displays the recorded signal, the left hand signal the spectrograms of the signal. The insert shows a zoom in of the signal for the reply event from one of the OBEMs. While the time of flight of the acoustic signal will be used to determine the distance of the OBEM and transmitter, the observed phase delay can be used to determine the heading of the reply signal for each receiver. Due to the short distances the signal travels through the water at the seafloor (as opposed to the entire water column with varying sound velocity for the Posidonia signal, which communicates to a ship board Posidonia antenna), we expect to be able to determine the position of the instruments and transmitter to an accuracy of 1 to 2 m.

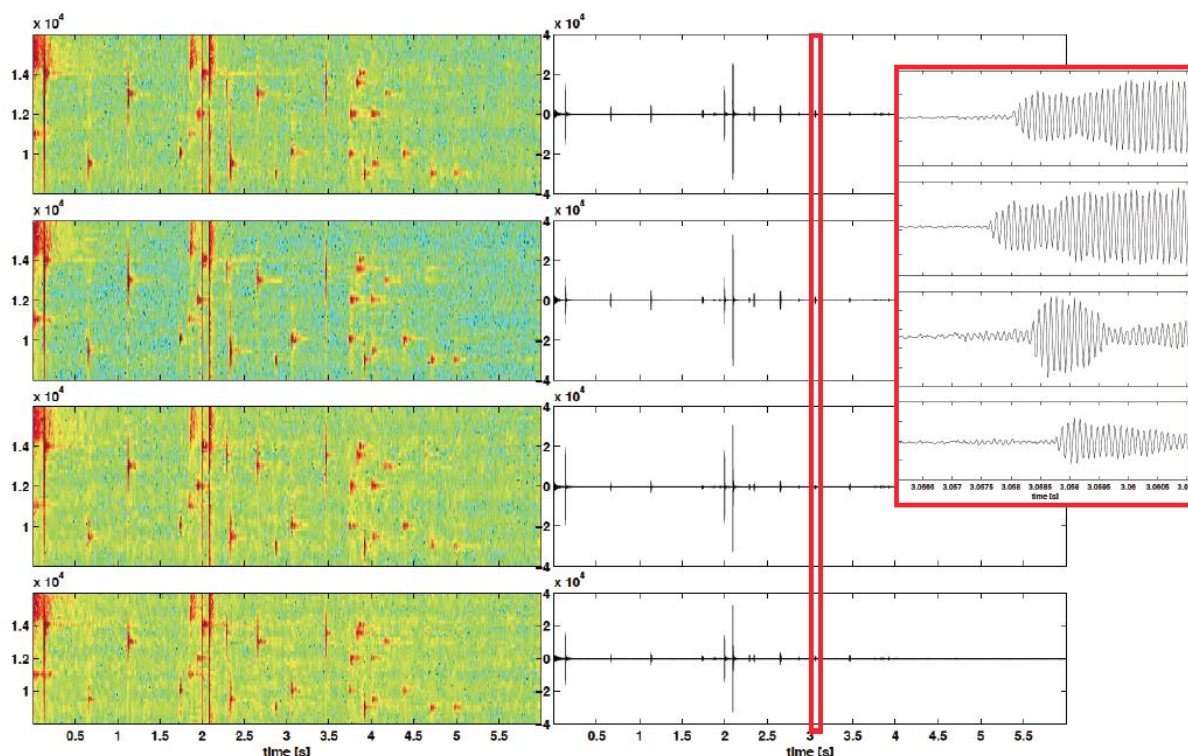


Fig. 5.3.10: Ranging data example. Reply signal from the receivers (reply frequencies are varied for different receivers to facilitate identification) at the four transducers on Sputnik after an interrogation ping. Right hand panel depicts the recorded signal, the left hand signal the spectrograms of the signal. The insert shows a zoom in of the signal for the reply event of a single receiver.

The concurrent seismic and electromagnetic data will help us, through a joint analysis, allow us to identify and distinguish between temperature anomalies, (low resistivity anomaly), presence of highly saline water (low resistivity anomaly) and hydrate (high resistivity and high P-wave anomaly) and gas distribution (high resistivity and low P-wave anomaly).

5.4. Heat flow

5.4.1. Objectives

The stability of gas hydrates depends on pressure and temperature. Pressure in the pore space of shallow marine sediments is hydrostatic and thus controlled by depth. In contrast, the temperature distribution in the sub-seabed is more complex and subject to temporal changes, e.g. due to seasonal variability of bottom water temperatures. Mapping of the effective geothermal gradient at the seabed provides a means to estimate the temperature field. Therefore, in situ sediment temperature measurements are crucial for determining the extent of the gas hydrate stability zone in the sub-seabed. In addition to conductive heat transfer in the sediment, the ascent of warm fluids at cold seeps and along faults creates temperature anomalies at the seabed. Detecting and quantifying these anomalies in turn provides information about the seepage. During this cruise, we conducted in situ temperature and thermal conductivity measurements in order to assess the extent of the gas hydrate stability zone, and to identify fluid flow in the sub-seabed.

5.4.2. Work at sea

In situ sediment temperature and thermal conductivity measurements were conducted using a 6 m-long heat flow probe. The probe has a Lister-type violin bow design. The sensor strings contain 22 thermistors spaced at an interval of 26 cm and a heater wire along the entire length of the string. The electronics are integrated into the head of the probe. Four 8-channels 22-bit A/D converters are used to record temperature readings at a sampling interval of 1 s. The probe can be operated in an autonomous mode or with real-time data transmission when using the ship's coax wire. During this cruise, measurements were conducted with real-time data transmission in so called 'pogo-style', performing several penetrations in a row at small distances. Each penetration consisted of raising the probe some hundred meters above the sea floor from the previous penetration, slowly moving the ship to the next penetration site and letting the wire angle become nearly vertical before dropping the probe into the sediment for the next penetration. Once the probe had penetrated the seafloor, it was left undisturbed for 7 minutes for the sediment temperature measurement and another 7 minutes, in case a thermal conductivity measurement was conducted. For the spacing of stations used in this survey, the transit between measurements took between 30 and 120 minutes. Transit speed was governed by the trade-off between keeping the wire angle small and minimizing the time between measurements.

Winch speed during payout and retrieval of wire was 1 m/s. Deployment of the instrument was from amid ship on the starboard side, employing a beam crane and assistance crane. This procedure ensured safe operation even during medium sea state and minimum interference due to the ships vertical movement during station work. For precise positioning of the probe at the seafloor, an IXSEA Posidonia transponder was mounted on the wire 100 m above the instrument. The IXSEA Oceanos Abyss positioning system was used to track the probe at depth.

Full processing of the measurements included the calibration of thermistor sensors, calculation of sediment temperatures and temperature gradients, correction for probe tilt during penetration, and calculation of thermal conductivities. Prior to each series of measurements, the probe was stopped at 100 to 200 m above the seabed for three to five minutes to inter-calibrate the temperature sensors. The software MHFRED (based on Villinger, 1987) was used to extrapolate the equilibrium sediment temperatures from the recorded time series at each station and to determine the thermal conductivity of the seabed at selected stations. Due to technical problems, thermal conductivity measurements could only be conducted during two deployments of the probe.

5.4.3. Preliminary results

During this cruise, we conducted 30 measurements in the working area at Formosa Ridge (Fig. 5.4.1) and 15 measurements in the second working area at the Four-Way-Closure Ridge Zone (Fig. 5.4.2). The locations were selected based on both previously available and newly acquired seismic data and will help to verify whether the current depth of the bottom simulating reflector is at equilibrium with the current temperature field. Preliminary analysis of the data suggests that the temperature distribution is controlled mainly by the seafloor topography. Lateral cooling leads to decreased temperature gradients along the ridge crest, whereas depressions and incisions on the flanks are characterized by increased temperature gradients. Several profiles show indications of bottom water temperature variability, see Fig. 5.4.3 for an example.

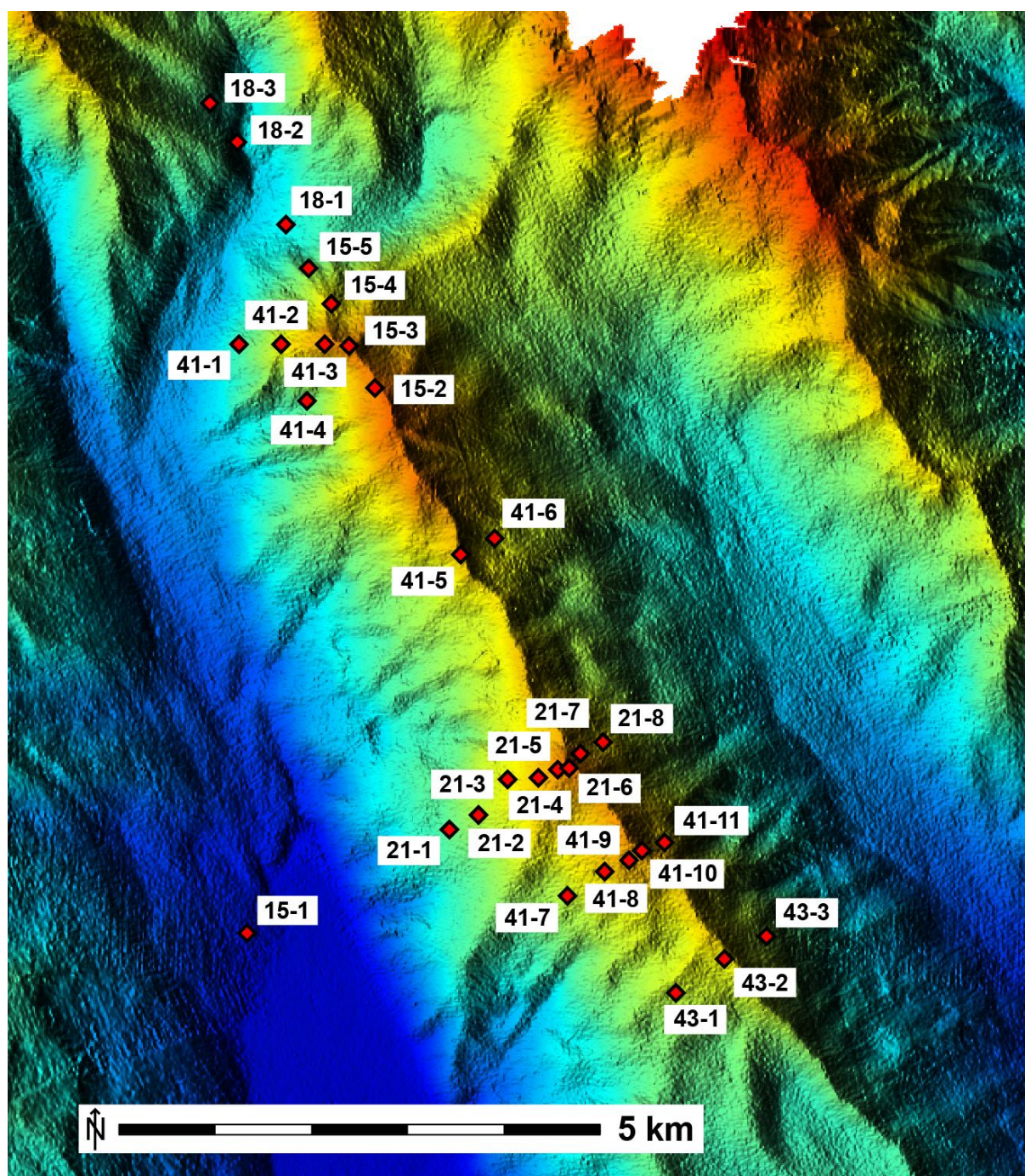


Fig. 5.4.1: Bathymetric map of the Formosa Ridge showing the locations of heat flow stations. The labels indicate the station numbers during the SO-227 cruise.

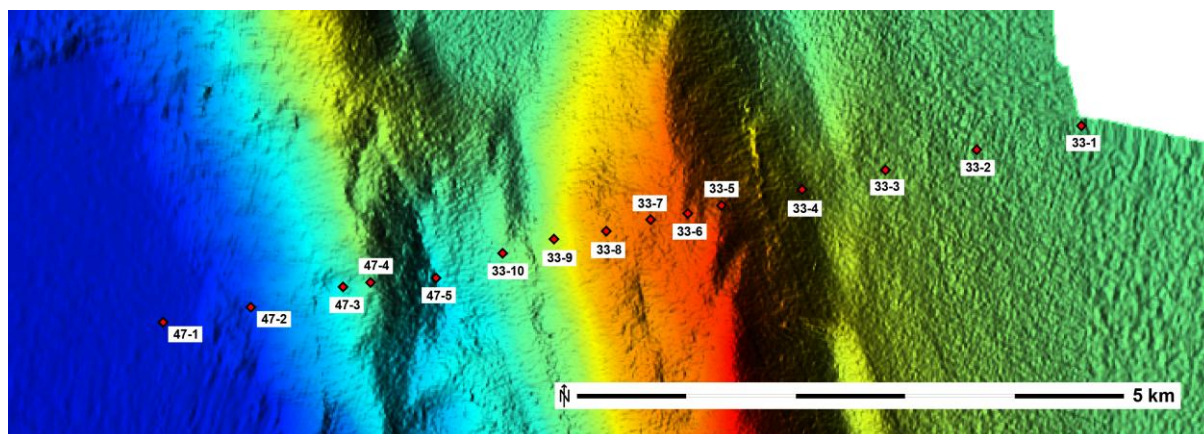


Fig. 5.4.2: Bathymetric map of the Four-Way-Closure Ridge Zone showing the locations of heat flow stations along a transect line perpendicular to the general dip. The labels indicate station numbers during the SO-227 cruise.

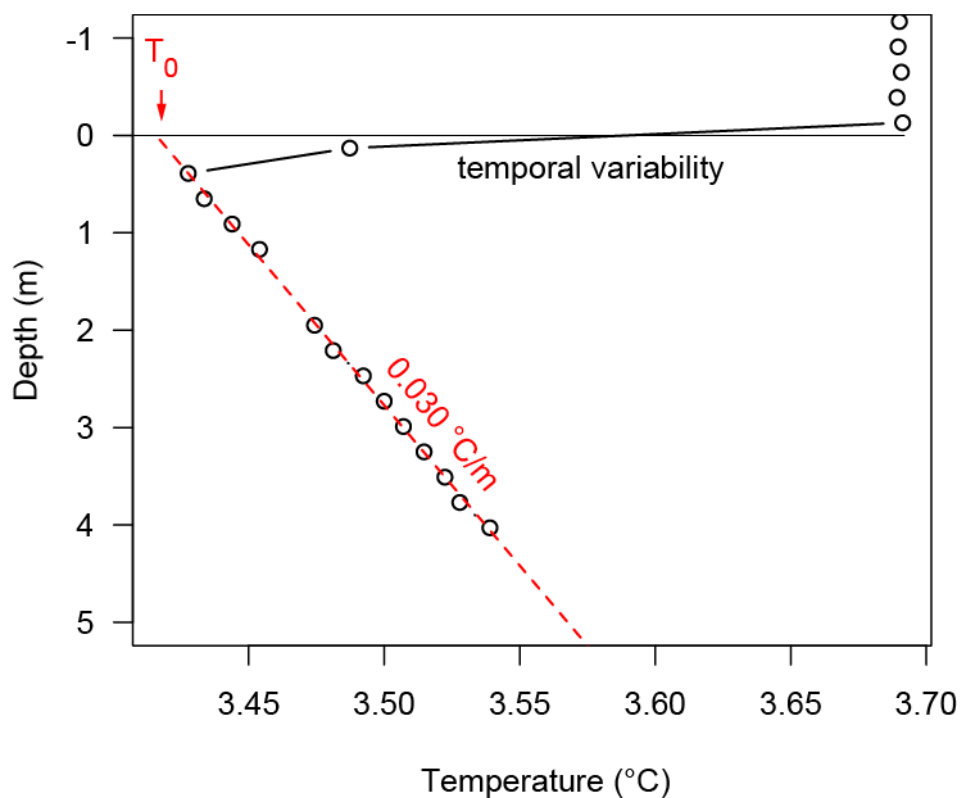


Fig. 5.4.3: In situ sediment temperature profile measured at station 21-4 on Formosa Ridge. At the time of the measurement, the bottom water temperature was approximately 0.3 °C higher than the long-term effective bottom water temperature T_0 indicated by the gradient of the deeper temperature profile (dashed red line).

5.5. Bathymetry

5.5.1. Equipment used

The RV SONNE is equipped with a SIMRAD EM 120 multi-beam echo sounder for continuous mapping of the seafloor. The SIMRAD EM 120. The SIMRAD EM 120 uses a frequency of 12 KHz with a total angular coverage sector of up to 150° (75° per port/starboard side), but can be modified by the user. During the cruise angles of 45 and 60 degrees, respectively, have been used. Each transmission ping is received as 191 reception beams and transformed into individual depth soundings. The beam spacing can be defined as either equidistant, equiangular, or a combination both and has been run in equidistant mode throughout the cruise. During the survey the transmit fan is split into individual sectors with independent active steering according to vessel roll, pitch and heave. This forces all soundings on a line perpendicular to the survey line and enables continuous sampling with complete coverage. Pitch and roll movements within ± 10 degrees are automatically compensated for by the software. The accuracy of the depth measurements depends on weather conditions and survey speed. Survey speed was variable ranging from 3 kn during the side scan and P-cable surveys to 8 kn during dedicated bathymetry profiles. Based on results of a previous cruise (SO226) a new roll calibration could be carried out and the roll value has been corrected by - 0.2 degrees. However, whether these corrections are still applicable is not clear. The calibration profiles during cruise SO226 have been obtained in an area with 13°C surface water temperature, while offshore Taiwan 26°C surface temperature has been measured. The ship's hull most likely deforms with these differences in water temperature. New roll calibration profiles could not be recorded by lack of flat-lying topography in deep water offshore Taiwan. Moreover, it is unlikely that this error has profound consequences on the geological interpretation of bathymetric features, which was the prime objective of bathymetric measurements during this cruise.

Multi-beam data were processed on board using the Caribes[®] software package for data cleaning, gridding and display. Roll corrections have not been applied and data before and after the new roll correction values had been entered into the acquisition system have been gridded together. The density of sounding allowed gridding the dedicated bathymetry profiles to a 50 metres grid size, while the bathymetric data obtained during the side scan and P-cable surveys allowed gridding at 25 and 10 metres grid spacing, respectively. The latter data have been gridded using a weighted distance algorithm while the other grids are based on near-neighbour algorithms. For some grids, dip and strike curvature maps have been calculated in Kingdom suite.

5.5.2. Sound velocity profiles

Good depth measurements require a correct sound velocity profile. Sound velocity profiles were collected at the beginning and in the end of the cruise (Fig. 5.5.1). Sound velocity corrections are automatically applied to bathymetry data in the Simrad operation software (SIS). Unfortunately, the original sound velocity profile obtained on April 2, 2013 was erroneous below 1957 metres water depth resulting in wrong depth measurements below that water depth. Attempts to correct these data on-board were unsuccessful and additional work will be required onshore.

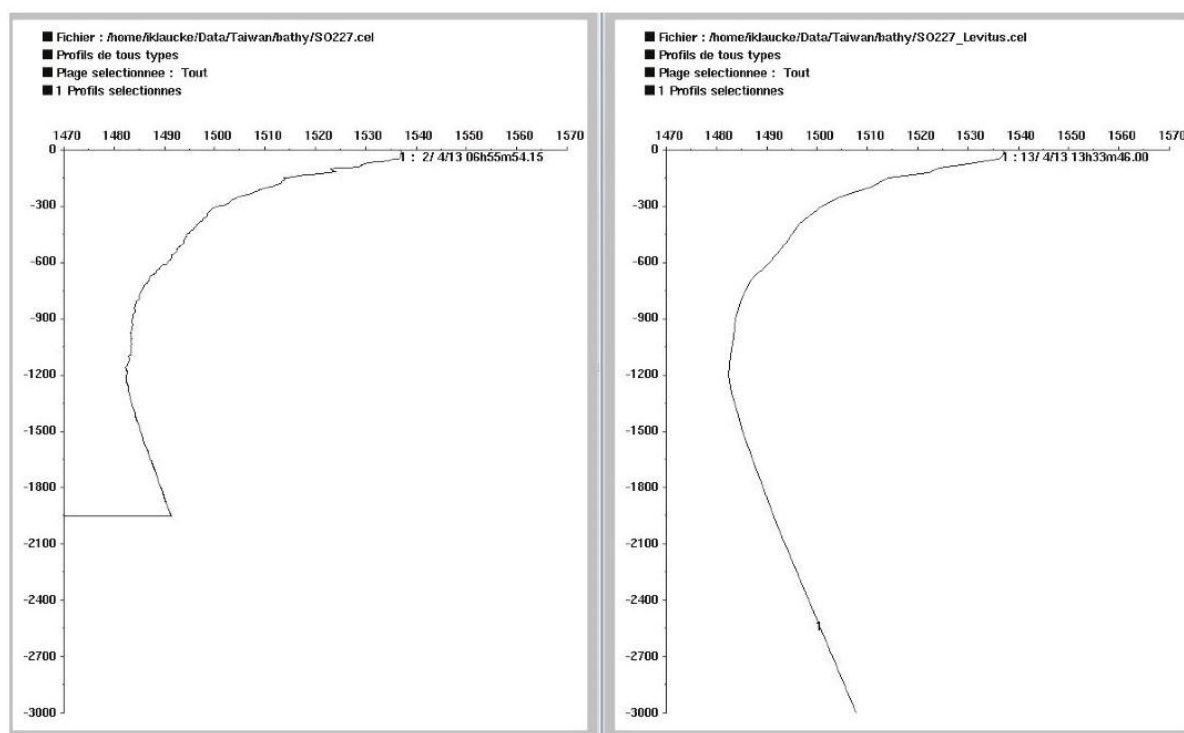


Fig. 5.5.1: Sound velocity profiles measured at the beginning and at the end of the cruise. The sound velocity profile to the left resulted in wrong depth measurements below 1957 metres water depth.

5.5.3. Results

Bathymetric data have been acquired in the entire working area southwest of Taiwan and covers water depths ranging from 500 to 2200 metres (Fig. 5.5.2). These data clearly show the difference between the passive continental margin in the West showing erosive canyons and ridges and the active margin in the East that is characterized by accretionary ridges. A short stretch of the active canyon is also shown. Observed mismatches between adjacent survey lines could be the result of wrong sound velocity, roll calibration or navigation, or a combination of all or part of these influences. Both P-cable and side scan sonar survey lines resulted in a particularly high data coverage at Formosa Ridge. Formosa Ridge has strong total relief of more than 700 metres between the base of the bounding canyons and the crest of the ridge that has two individual summits. A shaded relief map of the ridge highlights a number of interesting geological features including the thalweg of a canyon north of Formosa Ridge, terraces at the northern flank of the ridge, many stacked slump scars on the western flank of the ridge, and small elevations at the ridge crest marking the site of a known cold seep (Fig. 5.5.3). The slump scars and the terraces are particularly well highlighted by a dip curvature map (Fig. 5.5.4) of the bathymetry grid, while a strike curvature map images the drainage pattern on the ridge showing a typical badlands topography (Fig. 5.5.5). In comparison, Four-Way-Closure Ridge, on the other hand, shows a different morphology (Fig. 5.5.6). The ridge, as well as other ridges on the accretionary margin, is bounded in the West by a small, linear saddle that most likely marks the surface expression of thrust faults associated with the accretionary ridges. The western margins are also characterized by several mass failures with sharp looking slump scars. The eastern margin of the ridges, on the other hand, is generally somewhat smoother, but Four-Way-Closure Ridge is marked by two large and overlapping depressions, whose nature and formation mechanism remain unclear.

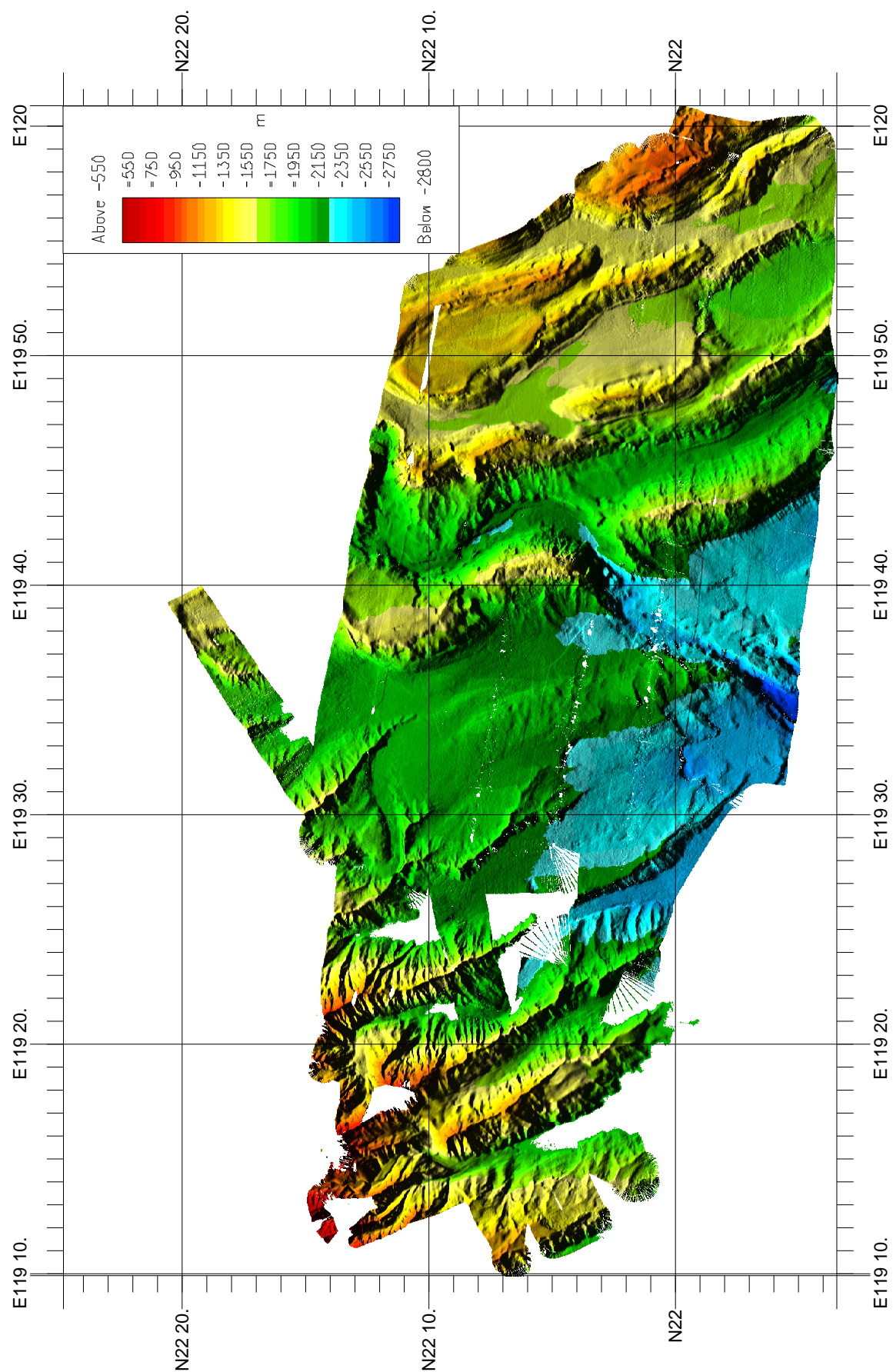


Fig. 5.5.2: Bathymetric chart of the working area offshore SW Taiwan showing the coverage of bathymetric data obtained during cruise SO227.

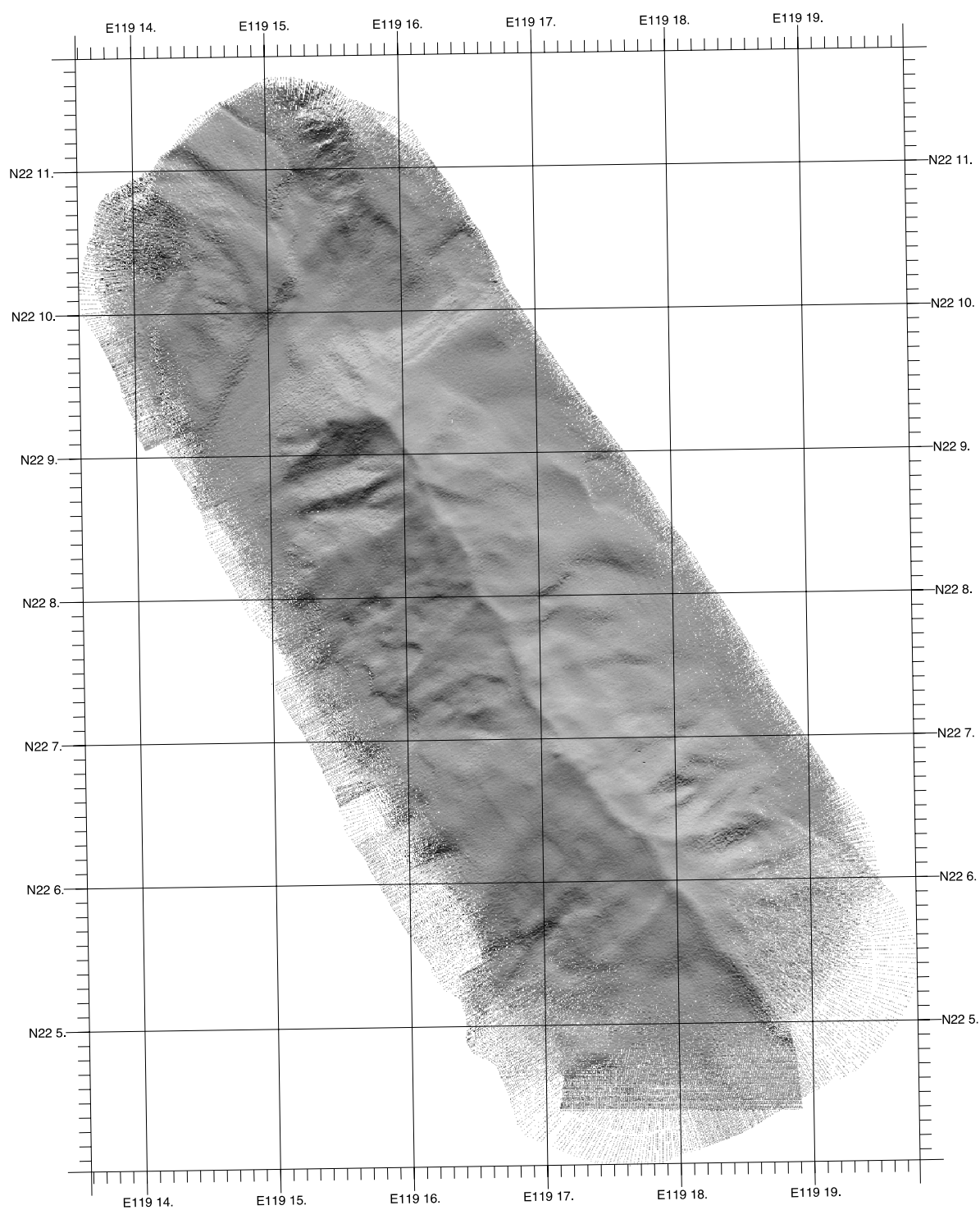


Fig. 5.5.3: Detailed shaded-relief map of Formosa Ridge based on a bathymetric grid with 10m grid cell size. Shading is from 355° azimuth and 30° dip.

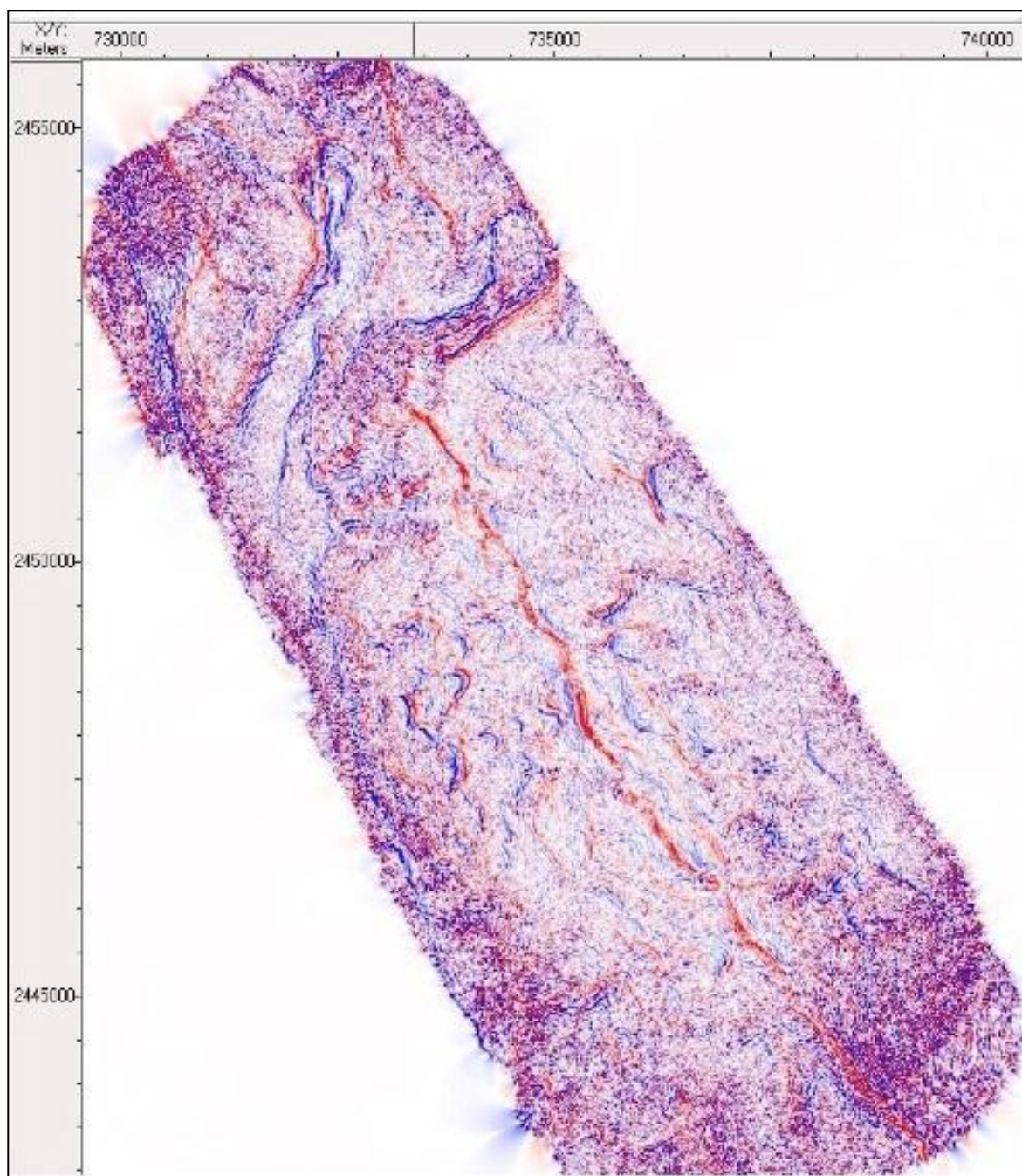


Fig. 5.5.4: Dip curvature map of Formosa Ridge based on 10m gridded bathymetric data.

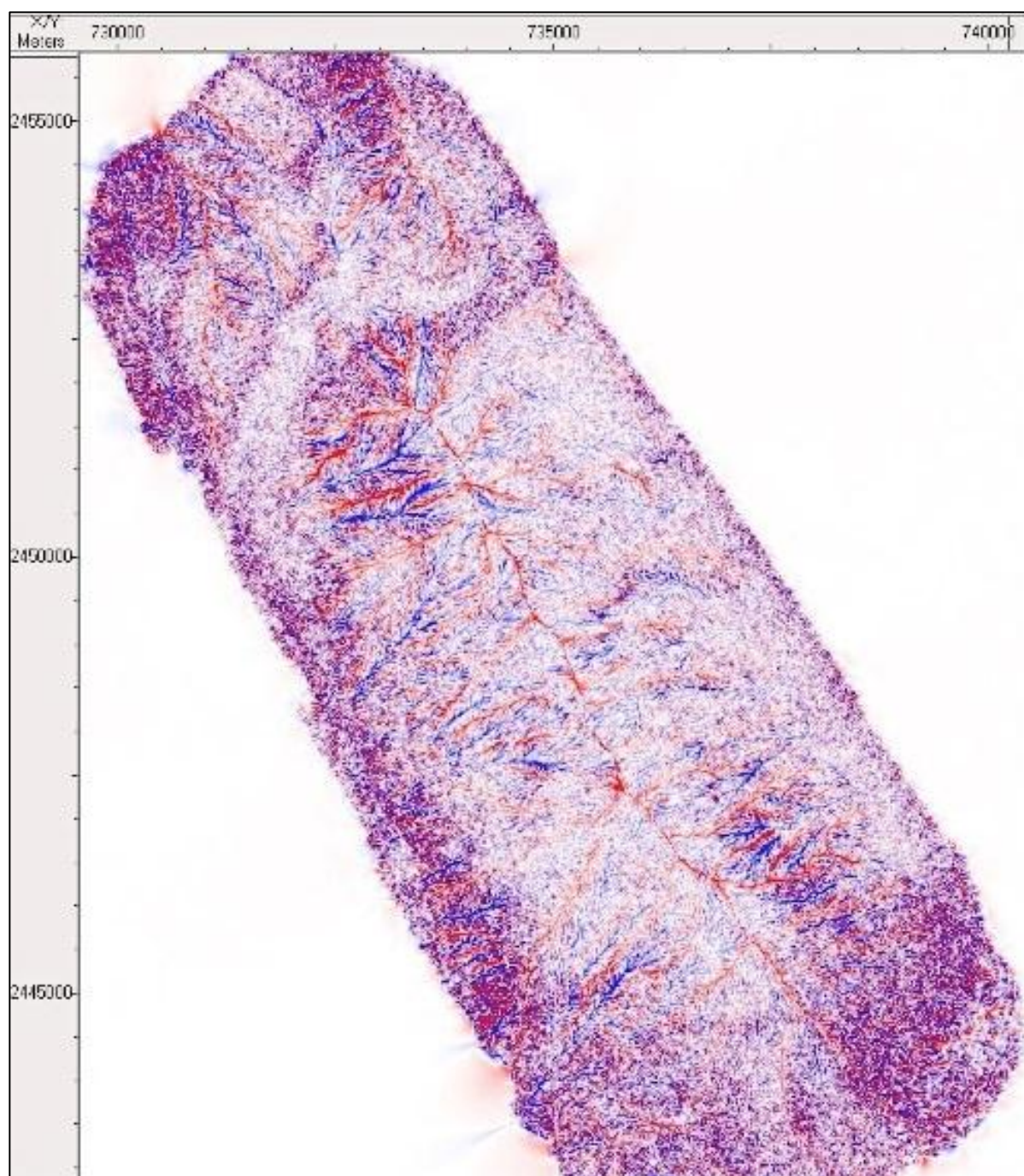


Fig. 5.5.5: Strike curvature map of Formosa Ridge based on 10m gridded bathymetric data.

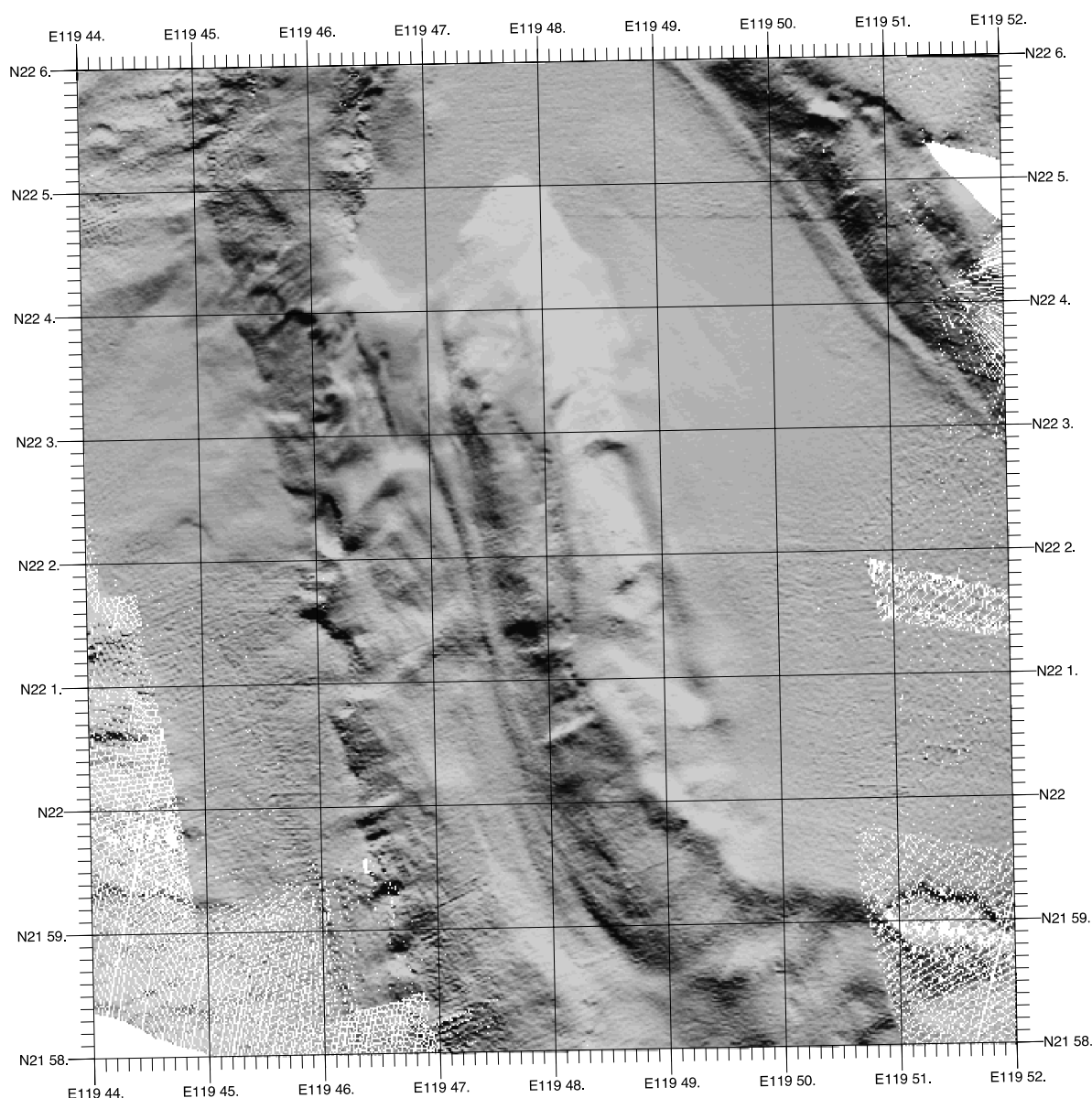


Fig. 5.5.6: Bathymetric chart of Four-Way-Closure Ridge based on a bathymetric grid with 25 m grid cell size.

5.6. Deep-towed sidescan sonar

5.6.1. Equipment used

Deep-towed geoacoustic images of the seafloor have been obtained using the DTS-1 system operated by GEOMAR. The DTS-1 consists of a modified EdgeTech dual-frequency side scan sonar and sub-bottom profiler (Fig. 5.6.1). During cruise SO227 only the low frequency option with a chirp signal of 75 kHz centre frequency and 14 ms pulse length has been used together with a sub-bottom profiler chirp signal of 2-10 kHz and 20ms pulse length. The 75 kHz side scan signal allows for 750 metres of range with a cross-track resolution of just a few centimetres, while the sub-bottom profiler allows for signal penetration of up to 40 metres sub-sea floor depth. The DTS also houses an internal Honeywell motion sensor recording fish heading, roll and pitch and a Sea&Sun pressure sensor that is needed to determine the towing depth of the sonar fish, which is required to process the sub-bottom profiler data.

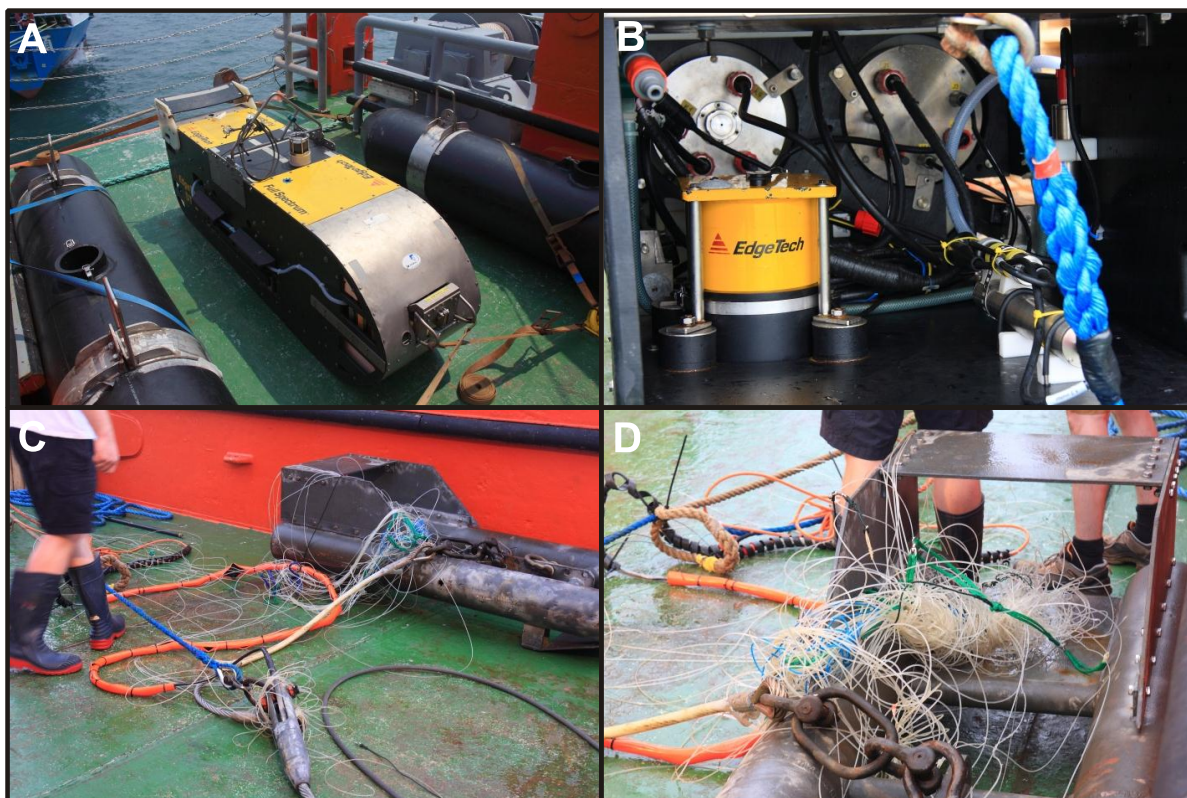


Fig. 5.6.1: The DTS-1 side scan sonar tow fish during cruise SO227. A. The tow fish on deck between floatations of the P-cable trawl doors. B. View inside the tow fish: telemetry wet end on the left, side scan electronics wet end on the right, the sub-bottom transducer in yellow and the CONTROS methane sensor. C. and D. fishing gear entangled around the side scan sonar depressor. Photographs: courtesy Chih-Wen Chen.

Sonar operations and data storage was realised using Hydrostar Online, resulting in data recorded in the XSE format. Back-up storage is also done directly in the tow fish in the JSF format. During operations the tow fish is towed roughly 100 metres above the seafloor (Fig. 5.6.2) and fish altitude is solely controlled by cable length.

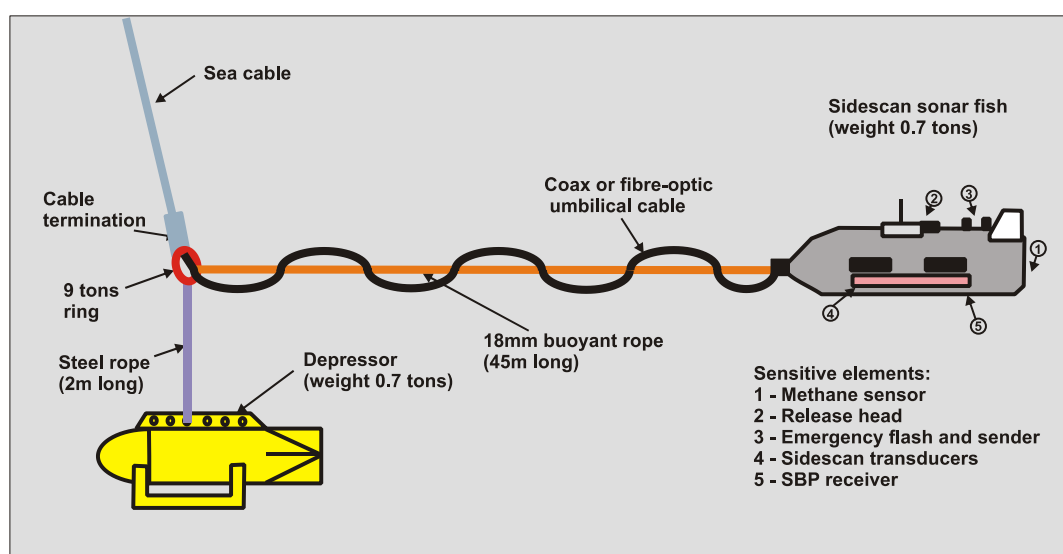


Fig. 5.6.2: The towing configuration of the DTS-1.

The side scan sonar data have been processed on-board using the Caraibes[®] software package and the sub-bottom profiler data using in-house scripts based on GMT and SeismicUNIX. The side scan data have been processed to a pixel size of 1.5 metres. As the Posidonia USBL system did not properly record the tow fish position, tow fish navigation is based on a layback method taking into account cable length and survey speed. This method gives good results for the distance of the tow fish behind the ship, but cannot account for lateral drift due to current. Such lateral mismatch can be on the order of a few hundreds of metres.

5.6.2. Deployments

The DTS-1 was used twice during cruise SO227. The first deployment dedicated to Formosa Ridge started at April 3rd, 2013 05:50 UTC and ended at April 4th, 2013 17:55 UTC and consisted of 7 roughly N-S profiles (Fig. 5.6.3). During the deployment the Posidonia USBL system only worked sporadically at the beginning of the survey after switching off the EM120 multi-beam system. Side scan sonar and sub-bottom profiler were pinging independently, which resulted to strong interferences in the sub-bottom profiler record. The morphology of Formosa Ridge only allowed north-south trending profiles, but even along these profiles, gradient were too steep and, at times, the instrument was either too far off the seafloor or even touched ground. Both situation resulted in a loss of data, but fortunately, the instrument was not damaged or the cable broken during contact with the seafloor. At one point during the second half of the deployment something has been entangled around the depressor weight. This went first unnoticed but some interference in the side scan sonar data and unusual strong roll when hauling in cable indicated that something was wrong. Upon recovery a thick, black rope was found entangled to the depressor and had to be cut free, so that the question what was attached to the rope has to remain unanswered.

The second deployment targeted Four-Way-Closure Ridge and lasted from April 10th, 2013 12:45 UTC until April 11th, 2013 09:30 UTC and consisted of 4 roughly N-S profiles (Fig. 5.6.4). During this deployment Posidonia was still not working with the transponder on the side scan tow fish, but side scan sonar and sub-bottom profiler were pinging simultaneously, resulting in much improved data quality. During the last profile the side scan sonar again became entangled in what turned out to be fishing gear. The entanglement was noticed by some small anomaly in the water column of the raw side scan sonar data and by increasing pull on the cable. The pull on the cable went from the usual 20 kN to over 70 kN before, luckily, the fishing gear snapped and not the side scan cable. We were able to finish the profile as planned and could recover the depressor with some remains of fishing lines attached to and entangled around it.

5.6.3. Results

Imaging steep morphologies such as Formosa Ridge and to a lesser extent Four-Way-Closure Ridge is quite challenging, as large portions of the side scan sonar lines lie within the shadows. More closely spaced survey lines would be required to obtain full imaging of the seafloor. Nevertheless some interesting features have been imaged including the known seep area at the southern summit of Formosa Ridge (Fig. 5.6.5). Unfortunately, the side scan images have been disturbed at this location by the ropes that have been entangled around the tow fish.

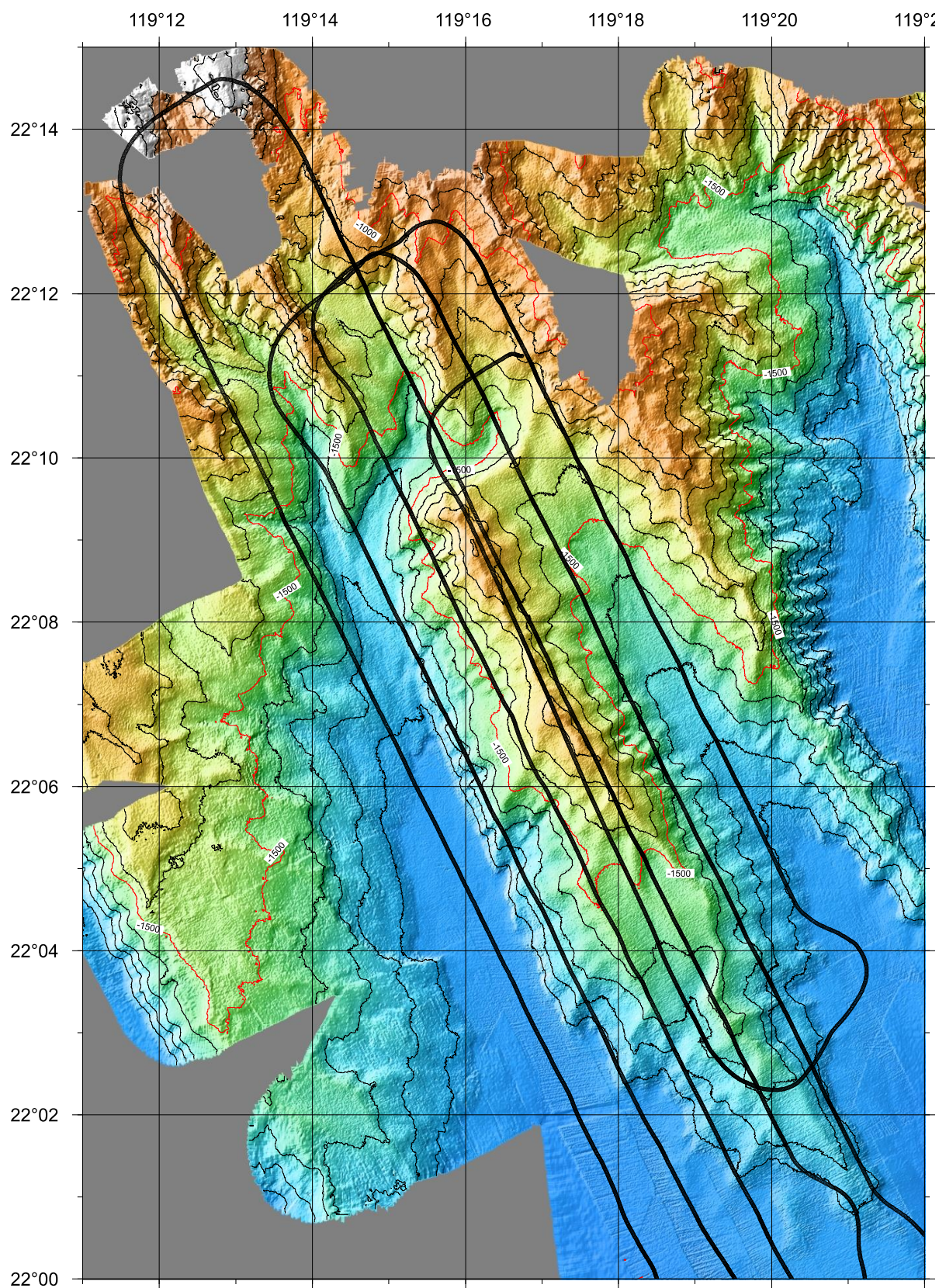


Fig. 5.6.3: Bathymetric map of Formosa Ridge with the DTS-1 tow fish navigation overlain. Tow fish navigation is based on a layback method.

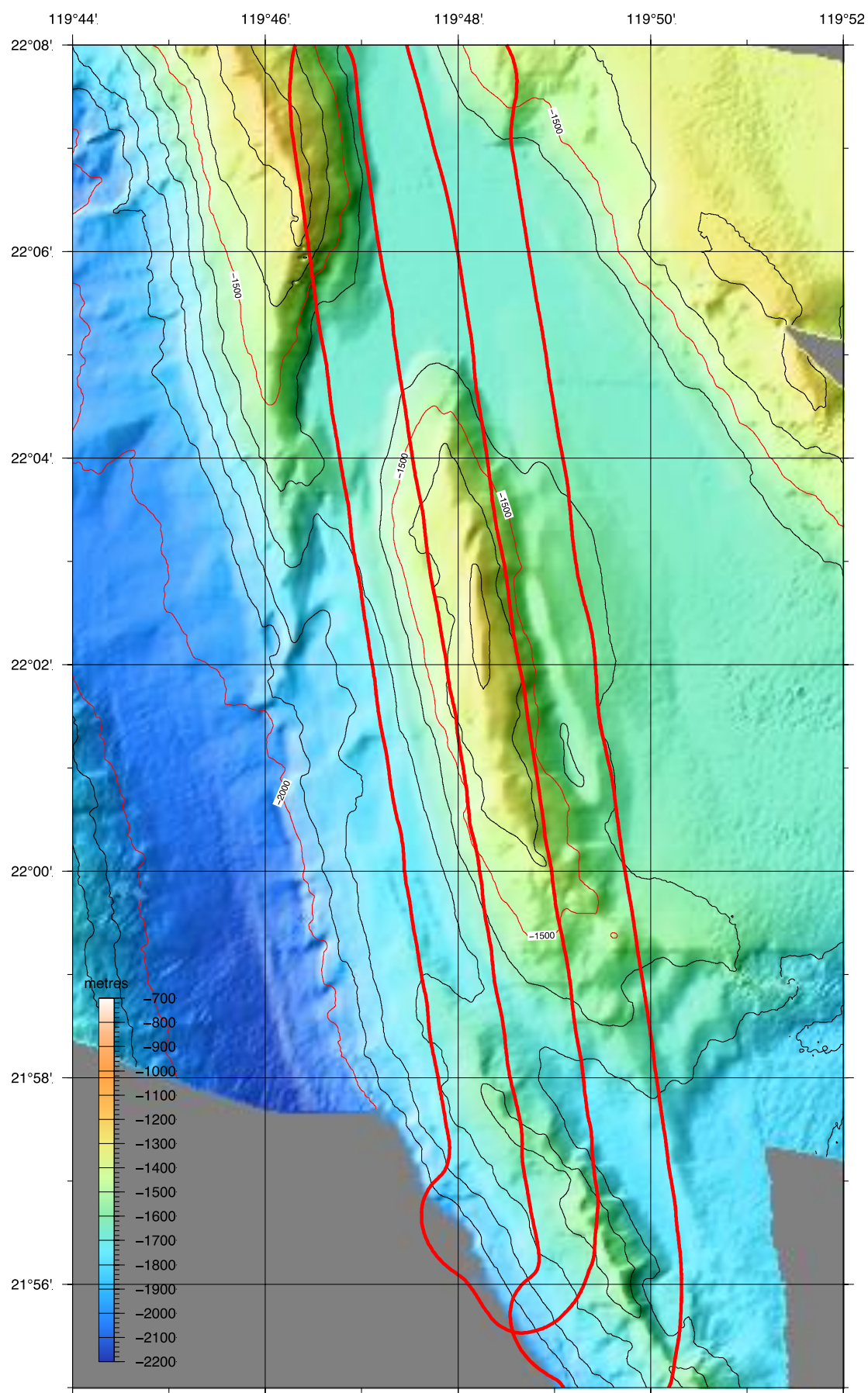


Fig. 5.6.4: Bathymetric map of Four-Way-Closure Ridge with the DTS-1 tow fish navigation overlain. Tow fish navigation is based on a layback method.

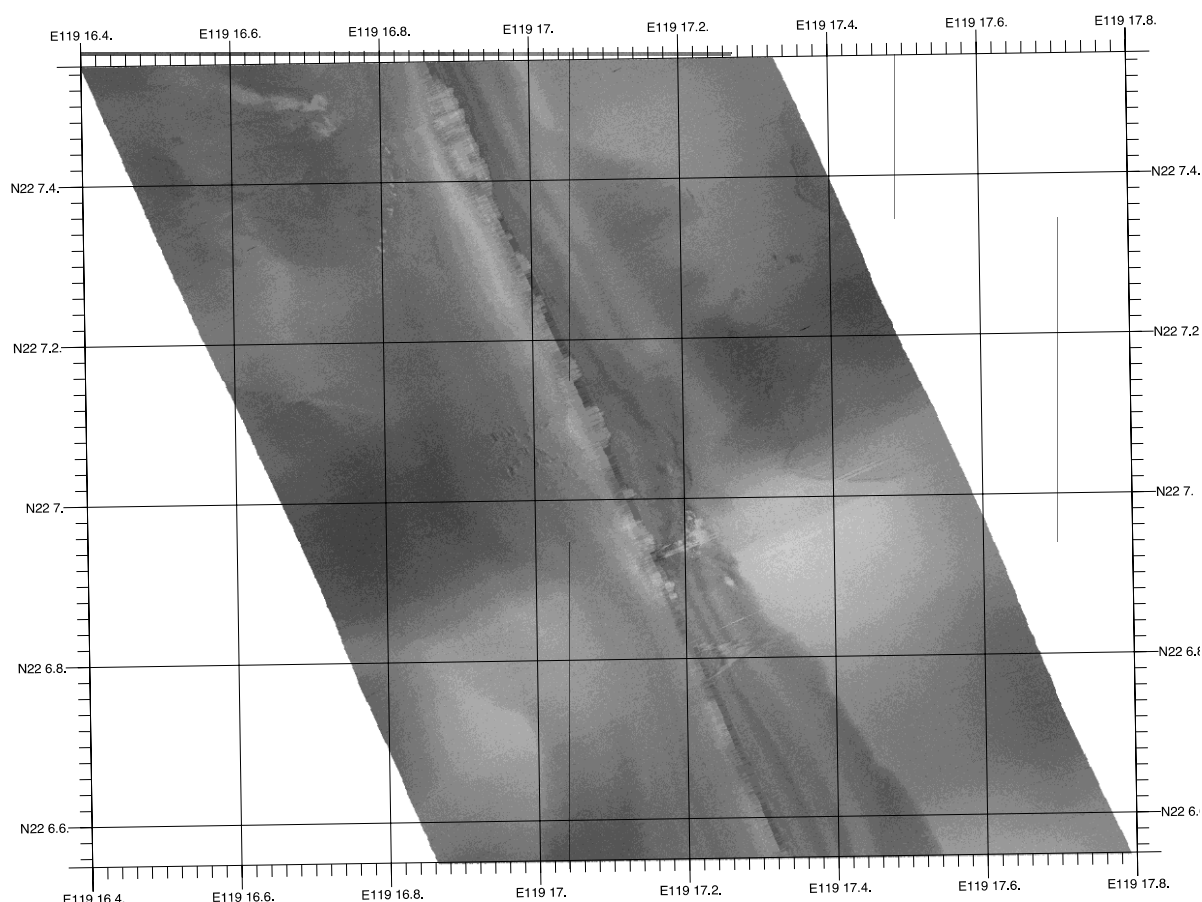


Fig. 5.6.5: Geo-referenced sides can sonar profile over the seeps at the southern summit of Formosa Ridge. High backscatter is shown in dark colours.

The seep area at the southern summit appears to be relatively small with an extension of roughly 100 metres along the crest of the ridge and only a few tens of metres in width. The side scan data also show that another potential seep area is located just 200 metres to the northwest of the southern summit. However, this site shows much less backscatter intensity and a patchy distribution of the elevated backscatter. The extent of shadows (light grey tones) in Fig. 5.6.5 highlights the difficulties in imaging high relief areas with deep-towed side scan sonar. Besides these examples, indications for cold seeps have not been found. The northern summit of Formosa Ridge (another potential seep site) could not be imaged, because the side scan fish was at or very near the seafloor at this steep location. The canyon floor east of Formosa ridge, however, revealed up to 2 km long, parallel grooves that are stretched along the canyon and with spacing of just of metres to tens of metres (Fig. 5.6.6). The origin of these lineations is not known, but they are likely the result of current activity.

Four-Way-Closure Ridge presents less relief and is therefore more suitable for side scan sonar imaging. During this survey potential cold seeps have been identified at two locations: on the crest of Four-Way-Closure Ridge and on the eastern flank of the frontal ridge to the South of Four-Way-Closure Ridge. The crest of Four-Way-Closure Ridge at 22°3.4'N shows very high backscatter intensity over an area almost 200 metres in length and 50 metres in width (Fig. 5.6.7). This seep is surrounded by smooth, uniform low backscatter deposits, forming some sort of westward tilted plateau.

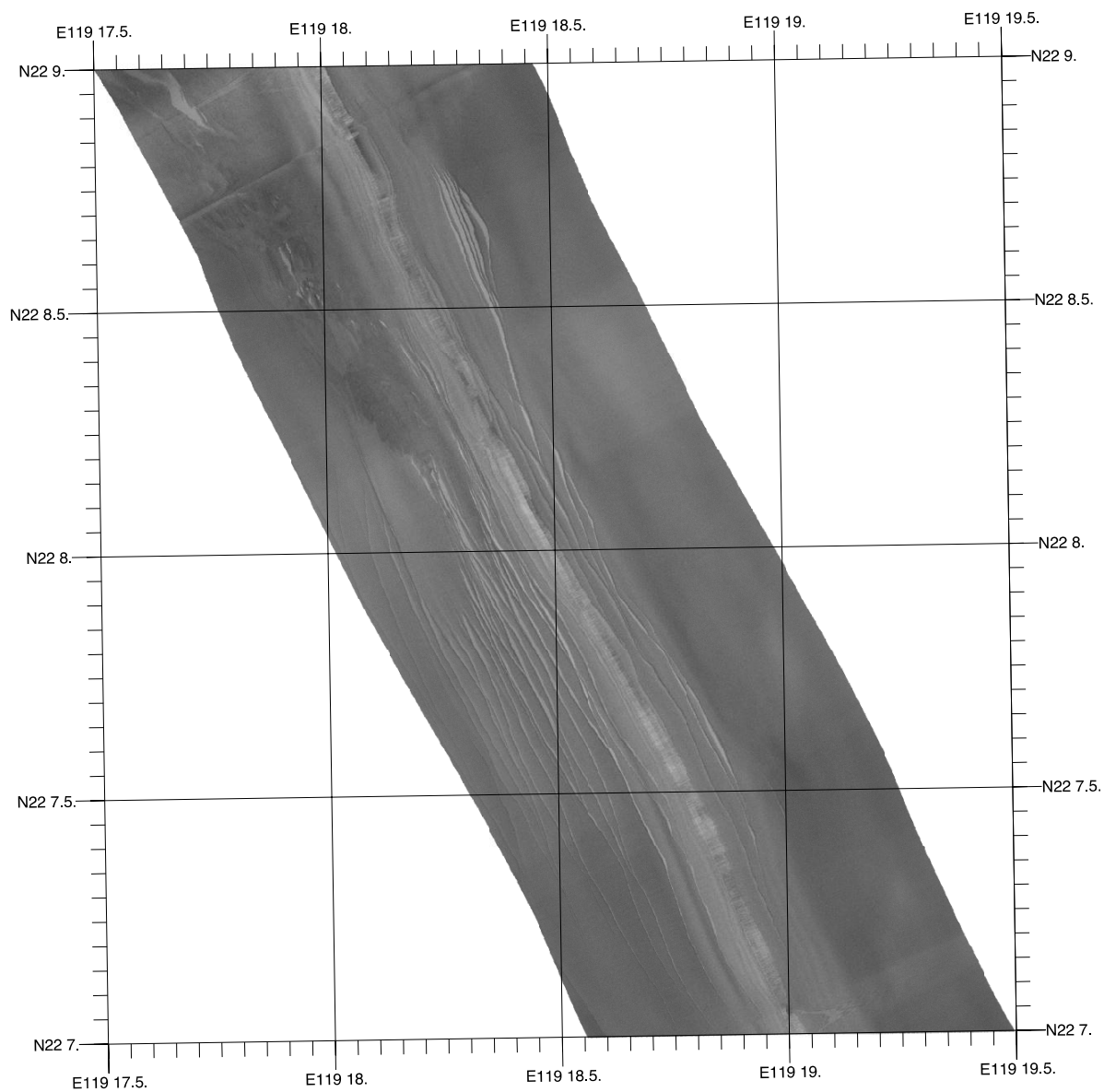


Fig. 5.6.6: Geo-referenced side scan sonar profile along the eastern bounding canyon of Formosa Ridge. High backscatter is shown in dark tones.

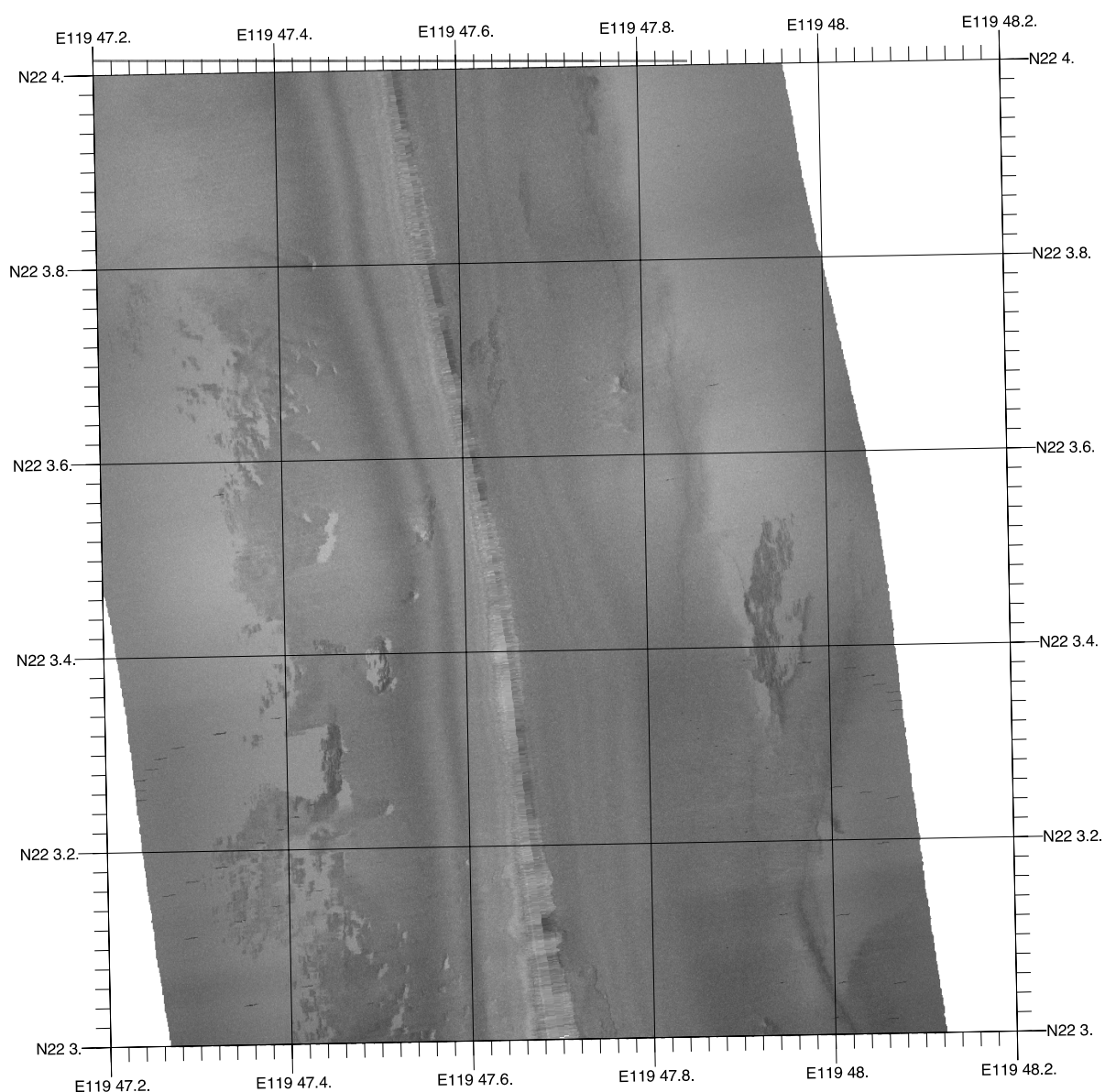


Fig. 5.6.7: Geo-referenced side scan sonar profile over the crest of Four-Way-Closure Ridge showing a seep. High backscatter is shown in dark colours.

Towards and at the western margin of this plateau several, north-south trending zones of very high backscatter intensity are visible. They make clear shadows and likely represent carbonate chemohierms on the seafloor. The chemohierms are 30-50 metres in length and have an aspect ratio of roughly 1:4. The steep flank beyond these potential chemohierms is not imaged. The second seep area on the north-eastern margin of the frontal ridge (Fig. 5.6.8) is more surprising, as it is located not on the crest of the ridge but on its flank and within uniform, featureless deposits. This zone actually consists of three individual seeps that are a few hundred metres apart. The largest and westernmost seep is roughly 500x300 metres in dimension and shows both large zones of high backscatter intensity and shadows indicating important relief that appears aligned in a N-S direction. High backscatter of the north-eastern seep is less intensive and shadows are only observed at the north-western edge. This seep is only 200x100 metres in dimension with the long axis SW-NE. The third seep lies right under the nadir and shows elevated backscatter intensity over a 400x100 metres wide area also with the long axis roughly SW-NE.

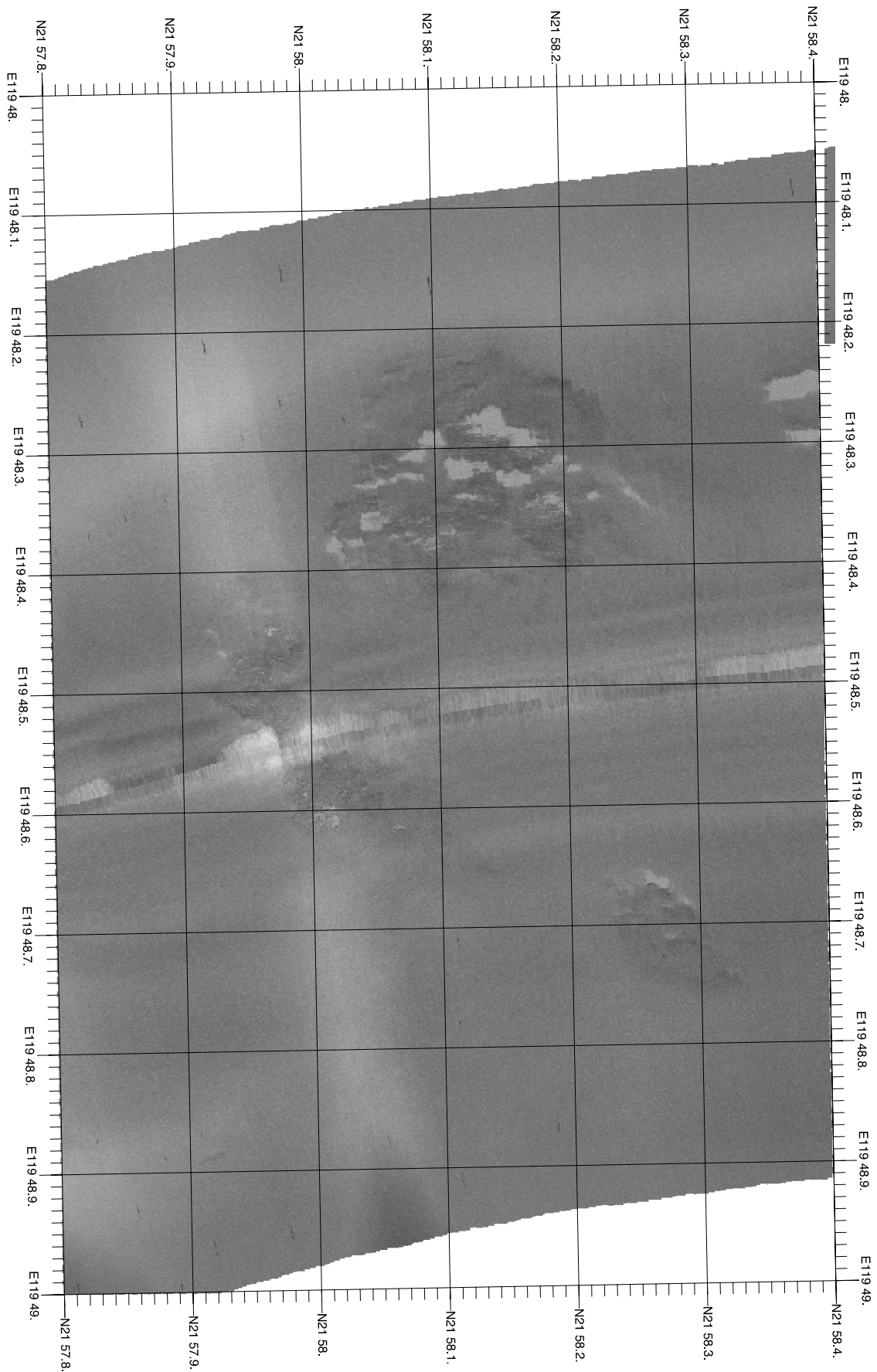


Fig. 5.6.8: Geo-referenced side scan sonar profile along the frontal ridge showing the location of three closely spaced seeps. High backscatter is shown in dark tones.

Besides potential seep areas, the side scan images of Four-Way-Closure Ridge also show extended zones of alternations between shadows and normal backscatter intensity (Fig. 5.6.9). These alternations likely represent bedding planes that are either exposed due to tectonic uplift of current erosion.

The 2-10 kHz echo sounder profiles allow to make some additional observations. The canyon floor west of Formosa Ridge (Fig. 5.6.10) shows little penetration of the signal and many small hyperbolae indicating a rough seafloor. In contrast, the canyon floor east of Formosa Ridge (Fig. 5.6.11) shows a typical cut-and-fill sequence composed of well-stratified sediments. Sub-bottom penetration along this profile is up to 40 metres. Profiles higher up on the flanks of Formosa Ridge (Fig. 5.6.12) also show well-stratified deposits in places. However, these deposits have been heavily eroded and a recent drape of 5-8 metres in thickness seems to cover the ridge. Sediment echo sounder profiles along the flanks of Four-Way-Closure Ridge (Fig. 5.6.13) also show little penetration of the signal and many small incisions. The reason for this pattern is not known. Finally, the profile crossing the seep on the frontal ridge (Fig. 5.6.14) shows a typical facies of high amplitude scattering within the seep that appears to be widening at depth. This seep facies occurs within well-stratified deposits that appear to be exposed at the margin-ward side of the ridge while a more recent, high amplitude facies covers the basin-ward margin.

Finally, the DTS-1 also housed a CONTROS methane sensor during the two deployments and although these are not geoacoustic data, they will be briefly mentioned here. During both deployments, the sensor registered elevated methane concentrations at specific locations in the water column. On Formosa Ridge, only one source of the methane seems to be present (Fig. 5.6.15) and must be located west of 22°04.283 N and 119°17.116 W. On Four-Way-Closure Ridge the methane signal is more pervasive (Fig. 5.6.16) and more time to analyse the data will be needed.

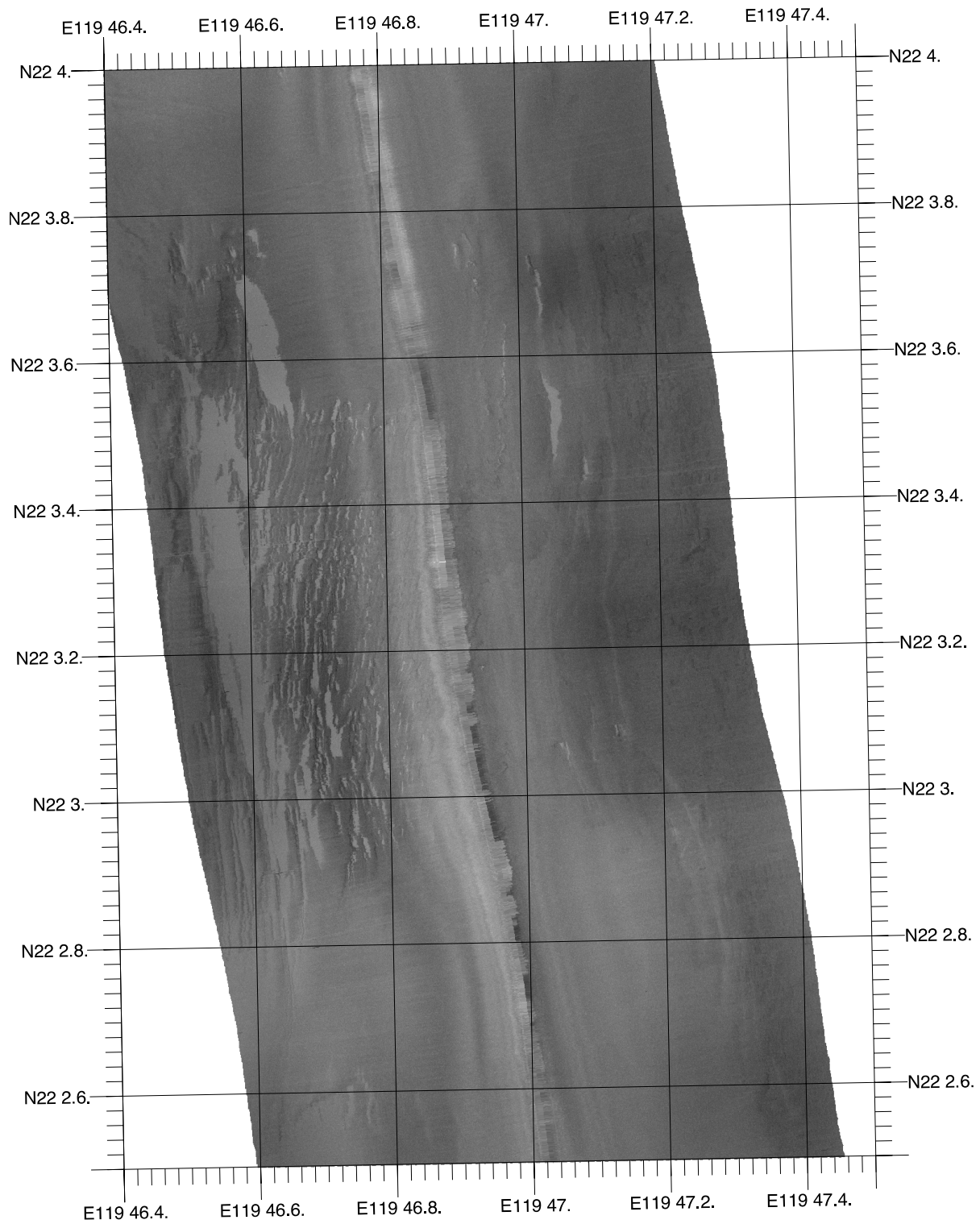


Fig. 5.6.9: Geo-referenced side scan sonar profile along the eastern flank of the frontal ridge just west of Four-Way-Closure Ridge showing alternating bands of high and low backscatter intensity. High backscatter is shown in dark tones.

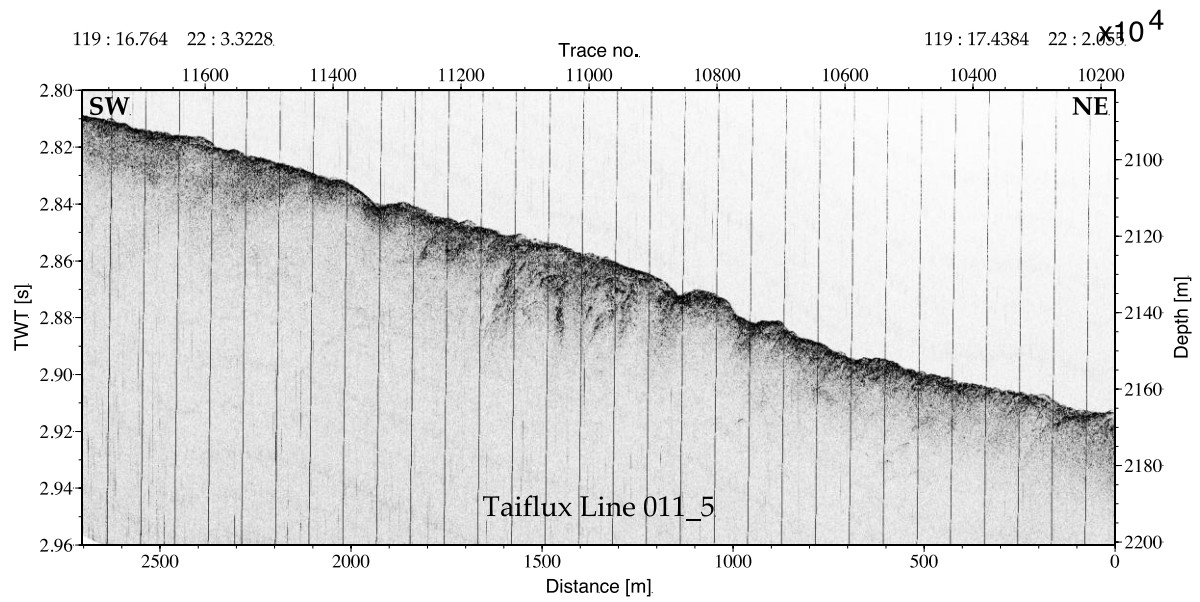


Fig. 5.6.10: High-resolution 2-10 kHz sediment echo sounder profile along the canyon floor West of Formosa Ridge.

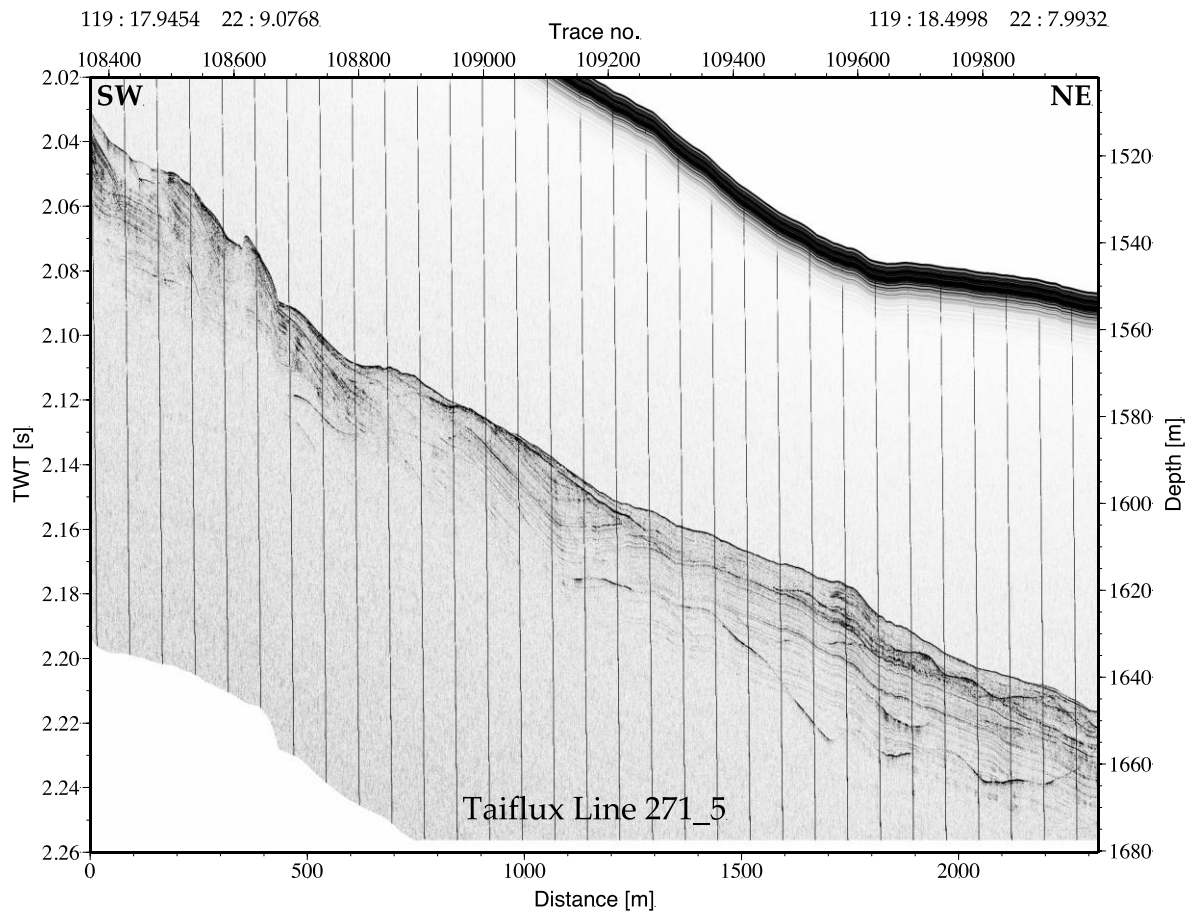


Fig. 5.6.11: High-resolution 2-10 kHz sediment echo sounder profile along the canyon floor East of Formosa Ridge.

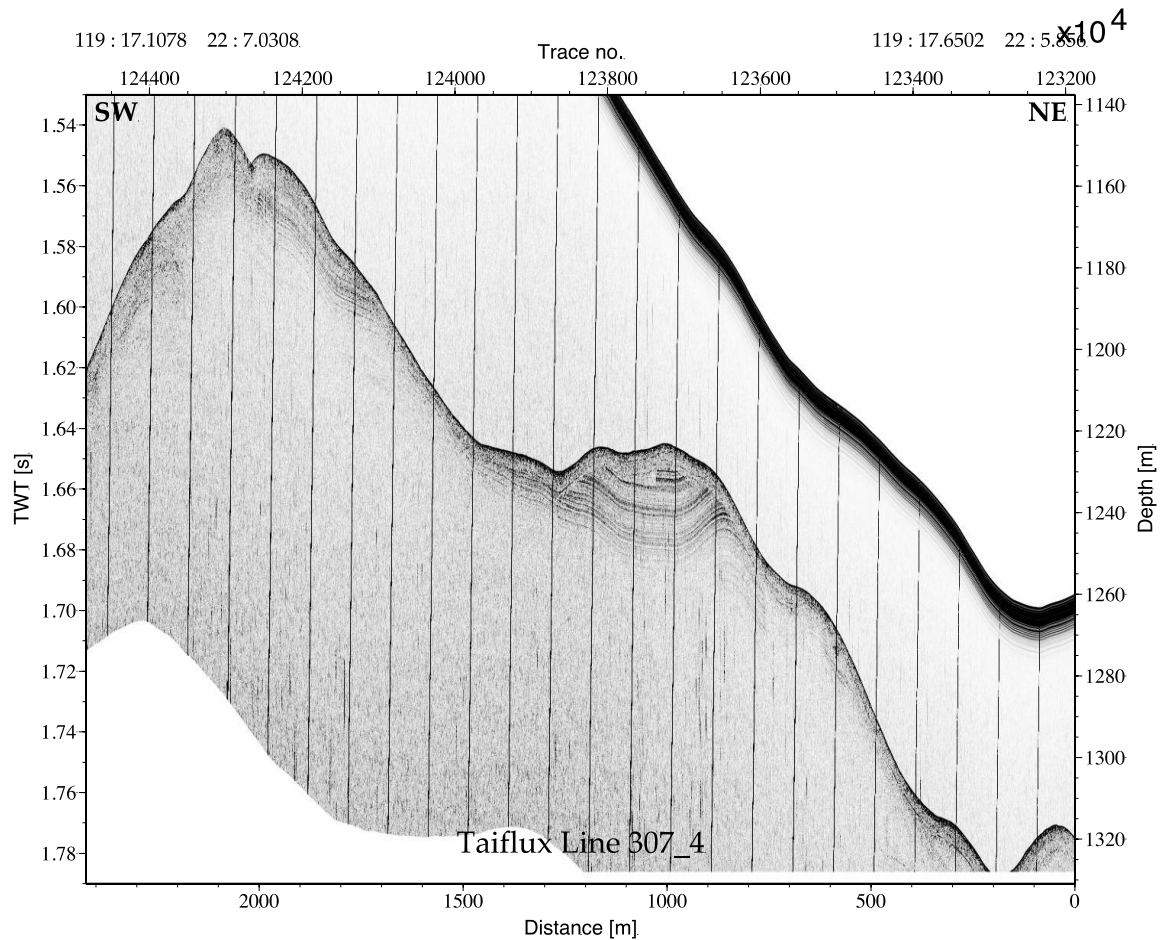


Fig. 5.6.12: High-resolution 2-10 kHz sediment echo sounder profile along the flanks of Formosa Ridge showing slope erosion and an angular unconformity.

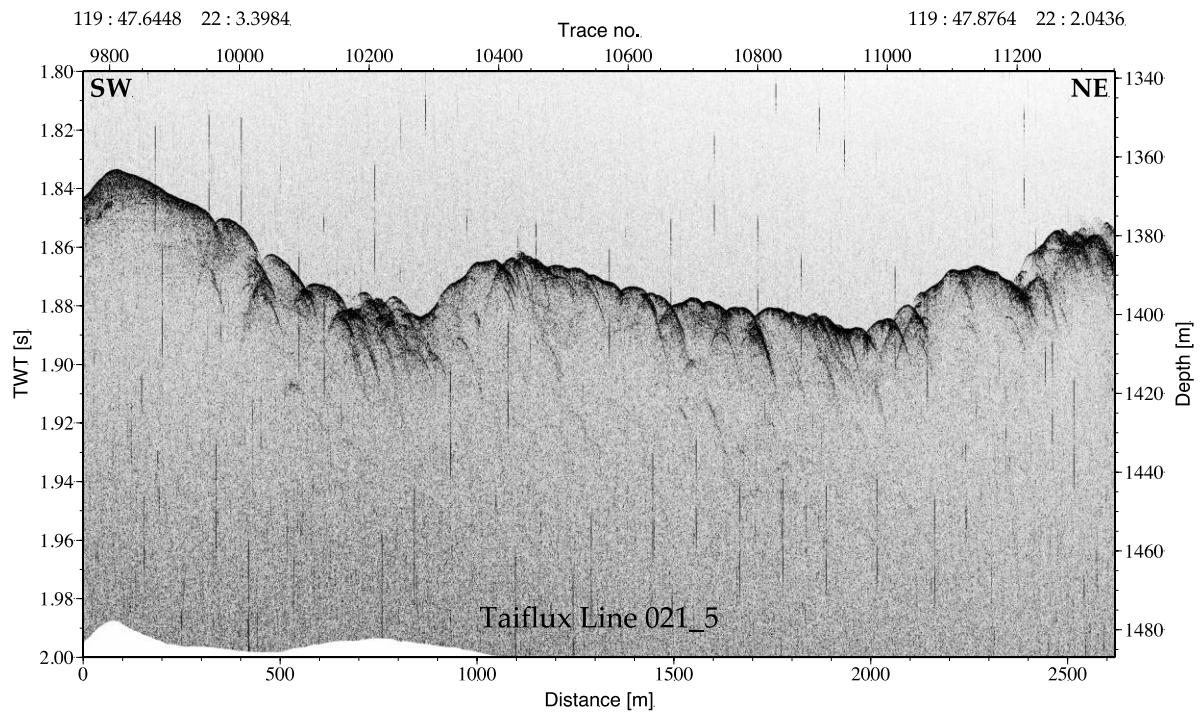


Fig. 5.6.13: High-resolution 2-10 kHz sediment echo sounder profile along the flanks of Four-Way-Closure Ridge showing many hyperbolae indicating a rough seafloor.

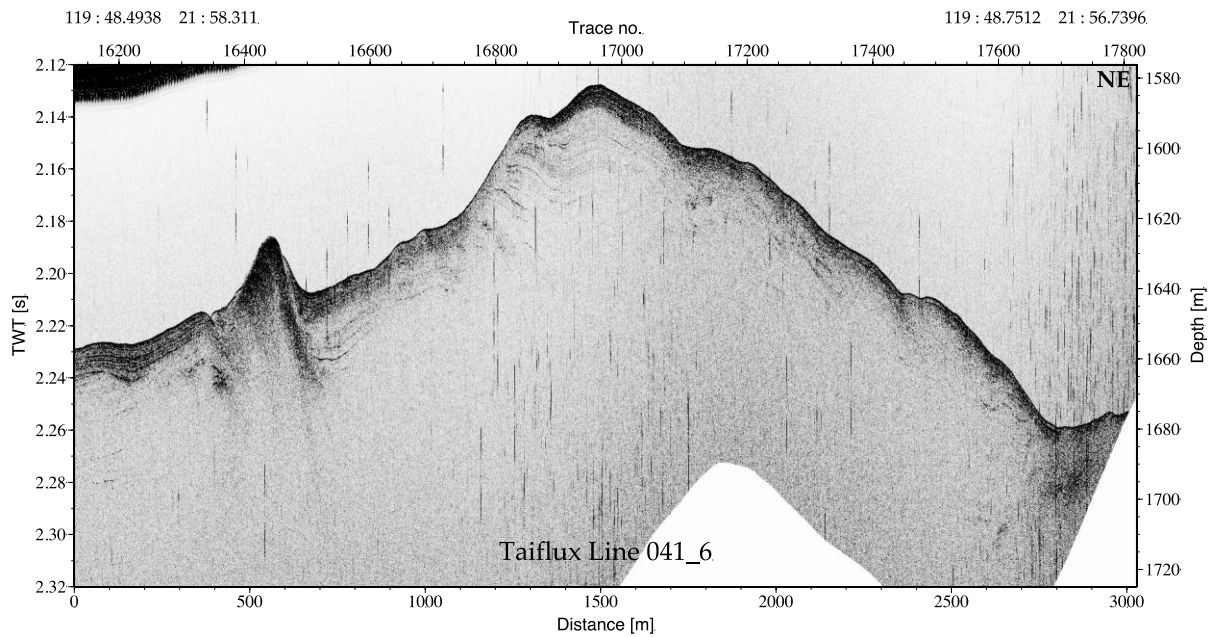


Fig. 5.6.14: High-resolution 2-10 kHz sediment echo sounder profile crossing a seep at the frontal ridge.

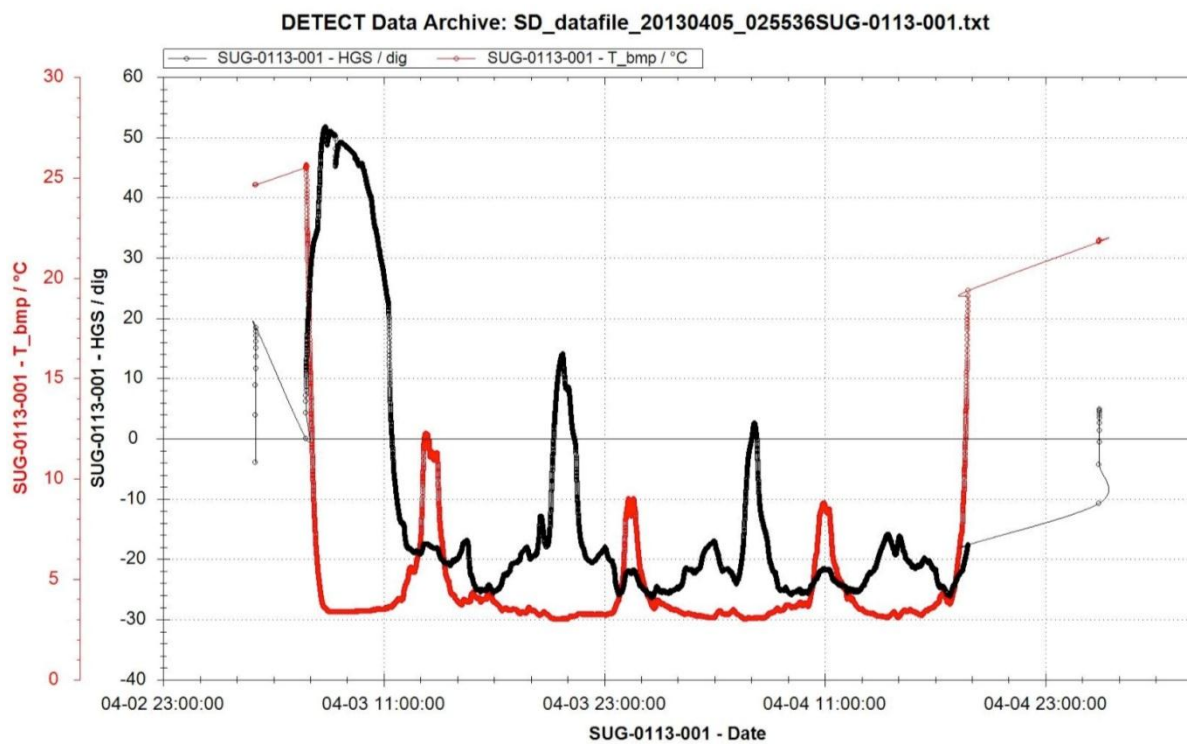


Fig. 5.6.15: Plot of bottom temperature and methane activity during the DTS-1 deployment at Formosa Ridge. The peaks in the temperature profile indicate the northern turning points, when the tow fish was pulled into shallow water depth.

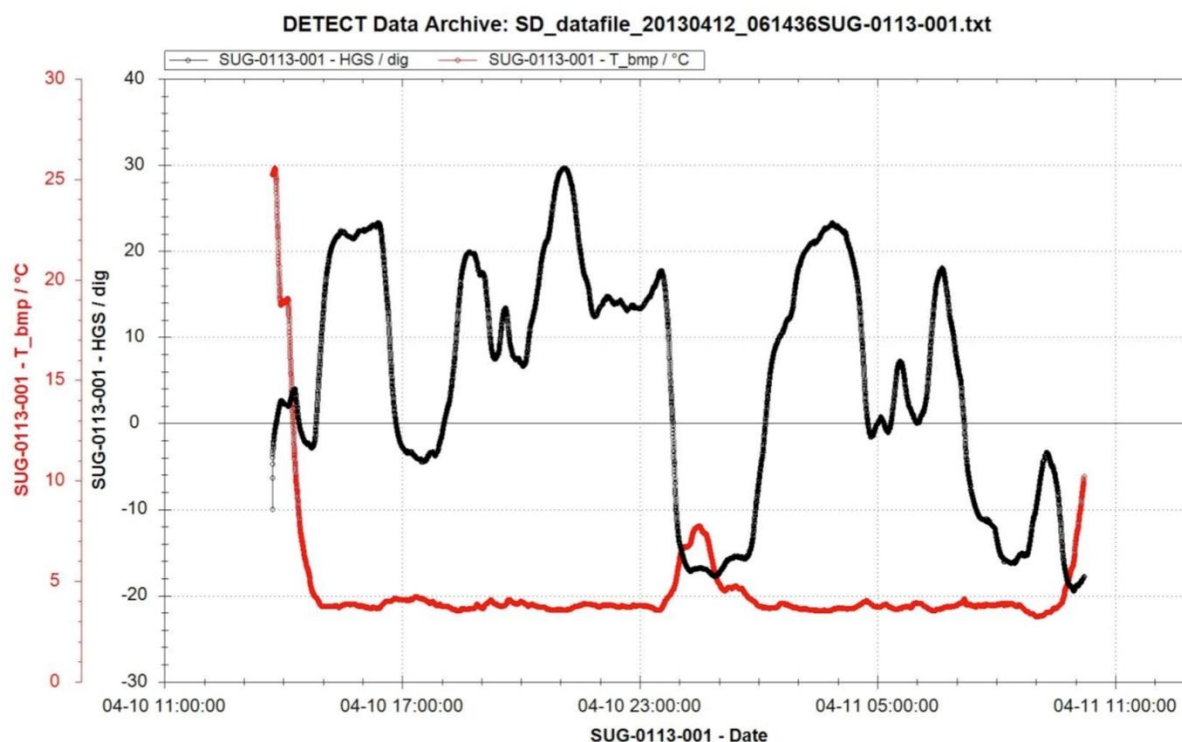


Fig. 5.6.16: Plot of bottom temperature and methane activity during the DTS-1 deployment at Four-Way-Closure Ridge.

5.7. HyBis operations

5.7.1. The HyBis vehicle

HyBis is a simple, low-cost, multi-purpose, survey and sampling robotic underwater vehicle (RUV) with a depth capability of 6000m (Fig.5.7.1). It was designed and built in the UK by Hydro-Lek Ltd. in collaboration with the National Oceanography Centre, Southampton (NOC), back in 2008. The GEOMAR HyBis is the second one built and this cruise was its maiden voyage.

The vehicle has a modular design that make its very versatile, with the top module being a command and power system that comprises power management, cameras, lights, hydraulics, thrusters and telemetry. Telemetry is via a single-mode fibre optic link and provides 3 channels of real-time standard-definition colour video plus vehicle attitude data. Power is supplied through a single-phase 1500V ac, 8kVA umbilical and converted to 3-phase 120V on the vehicle by two silicon motor controllers, 240V ac for the lights, and 24 to 12 V dc for onboard instruments.

The easily changeable lower modules available at the moment include a clam-shell sampling grab, a 5-function manipulator-arm and tool sled, and an ocean bottom seismometer deployment module. The sampling module used during SO227 during the video surveys comprised a 0.5 cubic metre clam-shell grab with a pay-load capacity of 750kg and closure force of 4 tonnes.

Unlike a conventional ROV, HyBis does not have any floatation or buoyancy. Instead it is suspended by its umbilical cable directly from the ship which makes it susceptible to ship roll and heave motion. On the positive side, the advantage of direct suspension is that HyBis can recover or deploy a payload of up to 750 kg.

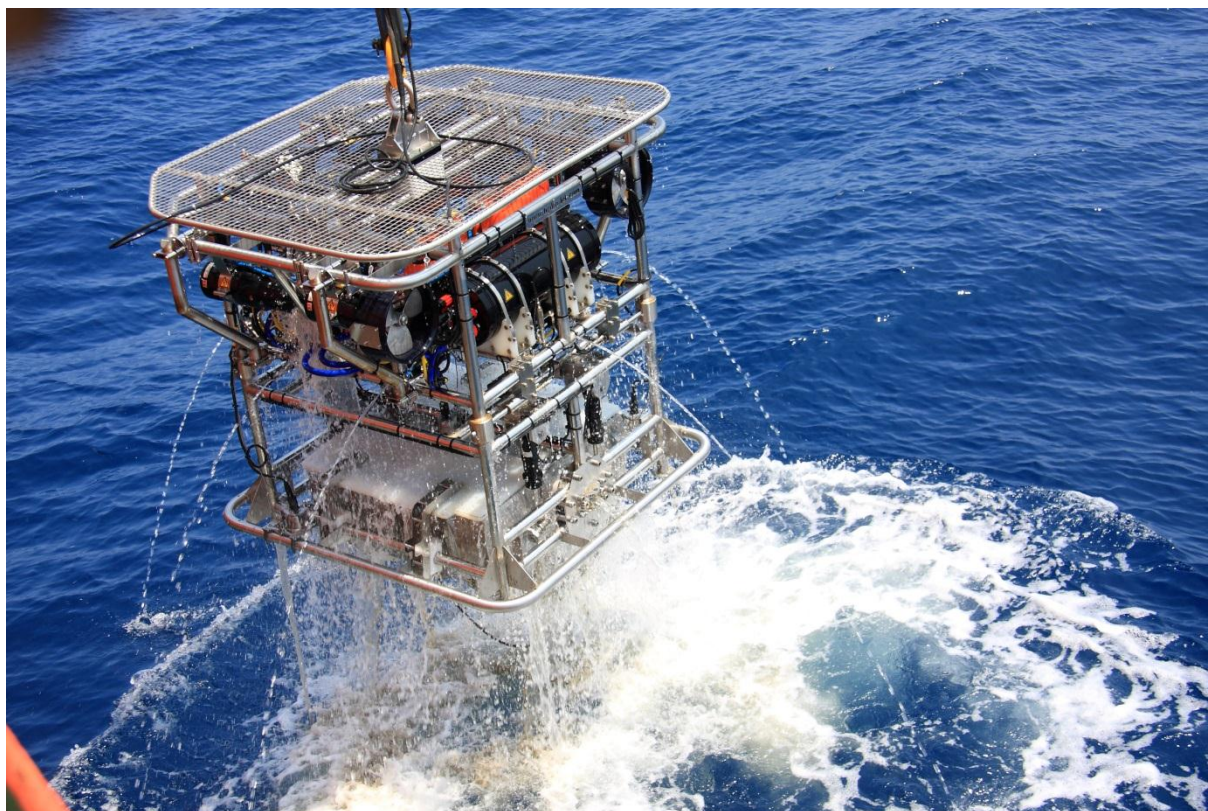


Fig.5.7.1: HyBis vehicle with grab on Formosa Ridge.

5.7.2. Laboratory control unit setup

The top-side control centre (Fig.6.7.2) was established in the geology lab, on port side, towards the aft. The vehicle's primary control box was supplemented with additional monitors and a relay of the USBL navigation screen. A dedicated GPS aerial was mounted on an out-rigger over the port side and provided a continuously recorded GPS string to the Garmin GPS navigation system in the control box. Winch controls were established adjacent to the vehicle pilot's position, allowing synchronisation between winch operator and pilot. Two additional television screens were installed in the conference room and the wet lab to give not involved cruise participants the opportunity to follow the operations without disturbing the driver.

Video was recorded digitally as .264 formats on 2Tb hard-discs. Two cameras (forward and downward SD) were recorded continuously in standard definition.

Acoustic navigation was provided by the 'Ixsea' USBL system Posidonia on RV Sonne and a mini transponder on the HyBis vehicle. Tracking was generally good although transponder battery conditions provided a limited maximum dive time of about 8 hours until recharge was necessary. The Posidonia data was recorded automatically in DShip.

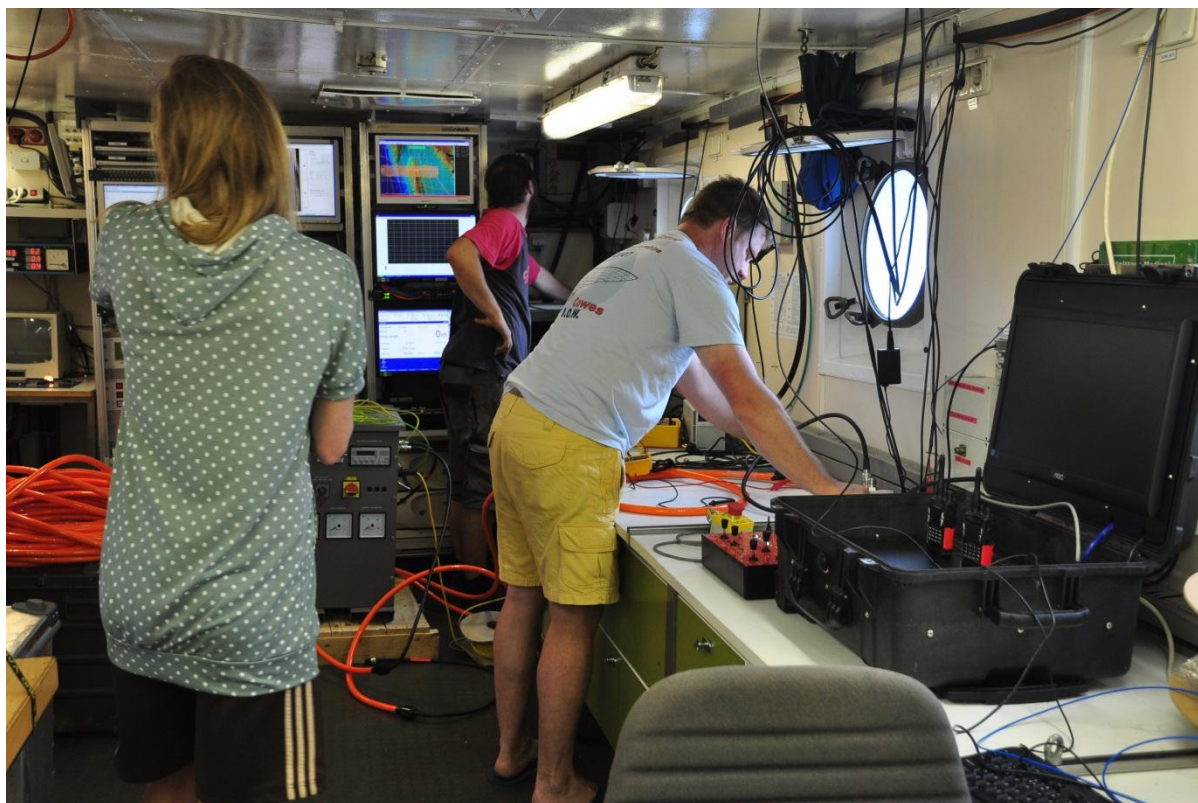


Fig.6.7.2: HyBis control unit (little black and red box to the right) with video monitors (black box to the right). The high-voltage transformer (grey box in the centre) was installed in the vicinity of the controls to keep it in sight. Posidonia navigation information was coming in on the monitors in the background.

5.7.3. High-voltage power setup

The high-voltage transformer was set up in a separated part of the Geology lab. The high-voltage was fed directly into the fibre optic cable. During tests we used a 220 V deck supply cable and high-voltage operations only started when HyBis was at 50 m depth except for one initial test on deck before the first cruise. Emergency stop buttons were installed on the transformer and next to the HyBis driver.

5.7.4. Dive narrative and vehicle performance summary

26th April 2013, HyBis Dive #1 Station number: SO227-34

Four-Way-Closure Ridge (119.80256°E 22.0583°N, approx. 1300 m water depth)

Aim: Assessment of the large seep system on Four-Way-Closure Ridge

Results: The dive discovered large carbonates and living mussel colonies. A sample of mud with dead mussels was collected.

26th April 2013, Hybis Dive #2 Station number: SO227-35

Four-Way-Closure Ridge (119.80256°E 22.0583°N, approx. 1300 m water depth)

Aim: Further mapping and assessment of the large seep system on Four-Way-Closure Ridge and a semi-circular side scan sonar anomaly to the west.

Results: During this dive we saw several large slabs of carbonate with cracks as well as bacterial mats. Everything indicates that this area is a fairly strong vent site. After a long transect across uniform grey seafloor we finally came to the side-scan sonar anomaly approximately 1 km further west. Here, we discovered very high carbonate blocks, but they were all covered by mud and seem to be not active anymore.

26th May 2012, HyBis Dive #3 Station number: SO227-37

Ridge south of Four-Way-Closure Ridge Ridge (19.79362°E 21.96883°N), water depth ~1692 m

Aim: Confirmation that the large side-scan sonar anomaly is caused by a seep

Results: With video footage and sampling we were able that this site is a methane seep. Large blocks of authigenic carbonate were discovered. A large fragment of a carbonate chimney could be picked up for geochemical analysis. In some places live mussel colonies.

27th April 2012, HyBis Dive #4 Station number: SO227-39

Top of Formosa Ridge (119.27413° E 22.11722°N), water depth ~1300 m

Aim: Sampling of live mussels

Results: Large pieces of carbonate overgrown with live mussels were found. Sampling did not work as HyBis tilted over when standing on a carbonate block. The camera into the grab moved and did not point down anymore. The system was recovered to fix it.

27th April 2012, HyBis Dive #5 Station number: SO227-39-2

Top of Formosa Ridge (119.27413° E 22.11722°N), water depth ~1300 m

Aim: Sampling of live mussels

Results: We recovered a large block of carbonate (0.3 m³) overgrown with mussels (*Bathymodiolus platifrons*). The grab also obtained limpet gastropods (*Bathymacrea tertia*), white shrimps (*shinkaia crosnieri*).

27th April 2012, HyBis Dive #6 Station number: SO227-39-3

Top of Formosa Ridge (119.27413° E 22.11722°N), water depth ~1300 m

Aim: Delimitation of the southern summit reef

Results: We circled once around the reef. Unfortunately, the *Posidonia* transponder ran out of battery shortly after deployment, so there is no navigation for this dive. Abundant carbonate blocks were found, some covered with live vent fauna.

27th April 2012, HyBis Dive #7 Station number: SO227-39-4

Top of Formosa Ridge (119.29483° E 22.09207°N), water depth ~1360 m

Aim: Investigation of flare SSW of the summit

Results: No evidence of seepage found.

27th April 2012, HyBis Dive #8 Station number: SO227-39-5

Eastern Flank of Formosa Ridge (119.30134°E 22.12863°N), water depth ~1360 m

Aim: Ground-truthing of linear features in the side-scan sonar.

Results: During the descent down the eastern flank of Formosa Ridge we saw terraces or sediment waves in the side scan sonar. Video observation of the seafloor did not show any fractures or fault cuts, but when approaching the thalweg we found several steps between smooth silty clays and rather undulated topography. There was approximately a 0.5 kt southerly current. Possibly these topographic steps caused the backscatter anomaly.

27th April 2012, HyBis Dive #8 Station number: SO227-39-40

Northern flank of Formosa Ridge (119.26878° E 22.14835°N), water depth 1300-160m

Aim: Investigation of the canyon incision

Results: As expected there was uniform seafloor at the top of the ridge. During the descent into the canyon there were several rugged areas with small ledges. There were several areas with increased benthic life, but no evidence of seep fauna. At the bottom of the canyon there are ripples and large blocks with dark patches.

5.7.4. Summary of HyBis operations

The first deployment of HyBis was a complete success. On its first dive it was possible to confirm the existence of an active seep system. On the fifth dive we recovered a large block of carbonate. In addition we recorded many hours of video observation of the seafloor which allowed us to correctly interpret the side scan sonar data and to distinguish between active and inactive seeps. So far, we have only made use of the video and grab capabilities and not of the manipulator arm as this was scientifically not sensible.

The system worked very well, but we discovered two construction deficits which have to be rectified after the cruise: a) the drainage holes for the frame should be on the downside not on the upside to prevent water from getting trapped in the system. The lid of one of the aluminium tubes is wired incorrectly and even after the 18 hours or so of deployment it is heavily eroded. This is potentially a safety problem as it may allow water to enter the system and short circuit the high voltage supply. This repair has to be carried out before the system is deployed again.

5.8. Geological Sampling

A total of 11 samples were collected using either Hybis Grab or TVG (Table 5.10.1). Among these, three authigenic carbonate were sampled, 3 seep sites with life benthic community, 3 with bleached shell fragments of various sizes, 1 relict seep tubes and 1 pelagic sediments.

Most sediment were collected at seep sites with the exception of pelagic mud at the site 39-5, a subcore taken from Hybis grab, on the slope edge of the Formosa Ridge. Black sediments and large bleached shells were found at Site 34. Site 37 sampled an area with relict tube and pipe shape in either yellow or brown colour. Hybis grab did not close at site 39 but some sediment with shell fragments remain on the side of grab. A large number of mussel and gastropoda were taken at site 39-2. Soft poorly cemented vent tubes, with bleached corals were found at site 42, a site near bacteria mats. Site 42-2 was taken at a cemented authigenic carbonate with mussel and galatheid carb on top. Site 48 was aiming at bacteria mat with black sediments. Site 48-3 was aiming at a large authigenic carbonate. Site 50 was characterized by a large patch of severely bleached shell patch with smelly black sediments. Another patch of life mussel and galatheid crab on a carbonate rock was taken at site 50-1.

6. Acknowledgements

We would like to thank captain Oliver Meyer, his officers and crew of RV Sonne for their professional support of our science programme and for very pleasant company on board. We also thank our technical team Martin Wollatz-Vogt, Gero Wetzel, Torge Matthiessen, Patrick Schröder and Olav Schwartz for being a great help.

The project TAIFLUX was funded by the BMBF through the RV Sonne program and by the National Science Council of Taiwan. Additional funding came from the institutions involved. We gratefully appreciate all these contributions.

7. References

- Abegg, F., Bohrmann, G., Freitag, J., und Kuhs, W., 2007, Fabric of gas hydrate in sediments from Hydrate Ridge—results from ODP Leg 204 samples: *Geo-Marine Letters*, v. 27, 269-277.
- Archer, D., und Buffett, B., 2005, Time-dependent response of the global ocean clathrate reservoir to climate und anthropogenic forcing: *Geochemistry Geophysics Geosystems*, v. 6, 1-13.
- Archie, G.E. The electrical resistivity log as an aid in determining some reservoir characteristics, *Petroleum Transactions of AIME* 146, 54-62.
- Berndt, C., 2005, Focused fluid flow in passive continental margins: *Philosophical Transactions of the Royal Society A*, v. 363, S. 2855-2871.
- Berndt, C., Mienert, J., Vanneste, M., und Bünz, S., 2004, Gas hydrate dissociation und seafloor collapse in the wake of the Storegga Slide, Norway, in Wandås, B.T.G., Eide, E., Gradstein, F., und Nystuen, J.P., eds., *Onshore–Offshore Relationships on the North Atlantic Margin*. Norwegian Petroleum Society (NPF) Special Publication, Volume Norwegian Petroleum Society (NPF) Special Publication: Amsterdam, Netherlands, Elsevier, 285–292.
- Birchwood, R., Singh, R., und Mese, A., 2006, Estimating the in situ mechanical properties of sediments containing gas hydrates, *Proceedings of the 6th International Conference on Gas Hydrates* ICGH 2008, Vancouver, British Columbia, Canada, July 6-10.
- Boswell, R., 2007, Resource potential of methane hydrate coming into focus, *Journal of Petroleum Engineering*, 56, 9-13.
- Bowin, C., Lu, R.S., Lee, C.S., und Schouten, H., 1978, Plate convergence und accretion in the Taiwan-Luzon region: *American Association of Petroleum Geologists Bulletin*, v. 62, 1645-1672.
- Brown, H.E., Holbrook, W.S., Hornbach, M.J., und Nealon, J., 2006, Slide structure und role of gas hydrate at the northern boundary of the Storegga Slide, offshore Norway: *Marine Geology*, v. 229, S. 179-186.
- Carcione, J.M. und Tinivella, U., 2000, Bottom-simulating reflectors: Seismic velocities und AVO effects, *Geophysics* 65, 54-67.
- Chand, S., Minshull, T.A., Gei, D., und Carcione, J.M., 2004, Elastic velocity models for gas-hydrate-bearing sediments - a comparison: *Geophysical Journal International*, v. 159, 573-590..
- Cheng, W.-B., Lee, C.-S., Liu, C.-S., Schnurle, P., Lin, S.-S., und Tsai, H.-R., 2006, Velocity structure in marine sediments with gas hydrate reflectors in offshore SW Taiwan, from OBS data tomography: *Terrestrial, atmospheric und ocean sciences*, v. 17.
- Cheng, W. B.; Lin, S. S.; Wang, T. K.; Lee, C. S.; Liu, C. S., 2010. Velocity structure und gas hydrate saturation estimation on active margin off SW Taiwan inferred from seismic tomography, *Marine Geophysical Researches*, 31(1-2), Sp. Iss. SI .77-87.
- Chi, W.-C., und Reed, D.L., 2008, Evolution of shallow, crustal thermal structure from subduction to collision: An example from Taiwan: *GSA Bulletin*, v. 120, 679-690.
- Chi, W.-C., Reed, D.L., Liu, C.-S., und Lundberg, N., 1998, Distribution of the Bottom-Simulating Reflector in the Offshore Taiwan Collision Zone: *Terrestrial, atmospheric und ocean sciences*, v. 9, 779-794.
- Chi, W.-C., Reed, D.L., und Tsai, C.-C., 2006, Gas Hydrate Stability Zone in Offshore Southern Taiwan: *Terrestrial, Atmospheric und Ocean Sciences*, v. 17, 829-843.
- Chiu, J.-K., Tseng, W.-H., und Liu, C.-S., 2006, Distribution of gassy sediments und mud volcanoes offshore southwestern Taiwan: *Terrestrial, atmospheric und ocean sciences*, v. 17, 703–722.
- Clennell, M.B., Hovland, M., Booth, J.S., Henry, P., und Winters, W.J., 1999, Formation of natural gas hydrates in marine sediments: 1. Conceptual model of gas hydrate growth conditioned by host sediment properties, *Journal of Geophysical Research* 104, 1978-2012.
- Dickens, G.R., O'Neil, J.R., D. K. Rea, und Owens, R.M., 1995, Dissociation of oceanic methane hydrate as a cause of the carbon isotope excursion at the end of the Paleocene: *Paleoceanography*, v. 10.
- Ecker, C., Dvorkin, J., und Nur, A.M., 1999, Estimating the amount of gas hydrate und free gas from marine seismic data, *Geophysics* 65, 565-573.
- Frej-Ayoub, R., Tan, C., Clennell, B., Tohidi, B., und Yang, J., 2007, A wellbore stability model for hydrate bearing sediments, *Journal of Petroleum Science und Engineering* 57, 209-220.

- Fyke, J.G., and Weaver, A.J., 2006, The Effect of Potential Future Climate Change on the Marine Methane Hydrate Stability Zone: *Journal of Climate*, v. 19, 5903-5917.
- Ginsburg, G.D., and Soloviev, V.A., 1997, Methane migration within the submarine gas-hydrate stability zone under deep-water conditions: *Marine Geology*, v. 137, 49-57.
- Golmshtok, A.Z. and Soloviev, V.A., 2006, Some remarks on the thermal nature of the double BSR, *Marine Geology* 229, 3-4.
- Haacke, R.R., Westbrook, G.K., and Hyndman, R.D., 2007, Gas hydrate, fluid flow and free gas: Formation of the bottom-simulating reflector: *Earth and Planetary Science Letters*, v. 261, 407-420.
- Hesslebo, S.P., Gröcke, D.R., Jenkyns, H.C., Bjerrum, C.J., Farrimond, P., Morgans-Bell, H.S., and Green, O.R., 2000, Massive dissociation of gas hydrate during a Jurassic oceanic anoxic event: *Nature*, v. 406.
- Hirtzel, J., Chi, W.C., Reed, D., Chen, L., Liu, C.-S., and Lundberg, N., 2009, Destruction of Luzon forearc basin from subduction to Taiwan arc–continent collision *Tectonophysics*, v. in Druck.
- Jakobsen, M., Hudson, J.A., Minshull, T.A., and Singh, S.C., 2000, Elastic properties of hydrate-bearing sediments using effective-medium theory: *Journal of Geophysical Research*, v. 105, 561-577.
- Johnson, A.H., and Max, M.D., 2006, The path to commercial hydrate gas production: *The Leading Edge*, v. May, S. 648-651.
- Jung, W.-Y., and Vogt, P., 2004, Effects of bottom water warming and sea level rise on Holocene hydrate dissociation and mass wasting along the Norwegian-Barents Continental Margin: *Journal of Geophysical Research*, v. 109, S. 1-18.
- Kennett, J.P., Cannariato, K.G., Hendy, I.L., and Behl, R.J., 2003, Methane Hydrates in Quaternary Climate Change: The Clathrate Gun Hypothesis: Washington DC, American Geophysical Union Special Publication, 216.
- Lin, C.-C., Lin, A.T.-S., Liu, C.-S., Chen, G.-Y., Liao, W.-Z., and Schnurle, P., 2009, Geological controls on BSR occurrences in the incipient arc-continent collision zone off southwest Taiwan: *Marine and Petroleum Geology*, v. 26, 1118-1131.
- Lin C-K., 2008, Algorithm for determining optimum sequestration depth of CO₂ trapped by residual-gas and solubility trapping mechanisms in a deep saline formation. *Geofluids*, 8, 333–343.
- Liu, C.-S., Schnurle, P., Wang, Y., Chuang, S.-H., Chen, S.-C., and Hsuan, T.-H., 2006, Distribution and characters of gas hydrate offshore of southwestern Taiwan: *Terrestrial, atmospheric and ocean sciences*, v. 17, S. 615–644.
- Liu, X., and Flemings, P.B., 2006, Passing gas through the hydrate stability zone at southern Hydrate Ridge, offshore Oregon: *Earth and Planetary Science Letters*, v. 241, S. 211-226.
- , 2007, Dynamic multiphase flow model of hydrate formation in marine sediments: *Journal of Geophysical Research*, v. 112.
- Long, D., Lovell, M.A., Rees, J.G., and Rochelle, C.A., 2009, Sediment-hosted gas hydrates: new insights on natural and synthetic systems: Geological Society, London, Special Publications, v. 319, S. 1-9.
- McDonnell, S.L., Max, M.D., Cherkis, N.Z., and Czarnecki, M.F., 2000, Tectono-sedimentary controls on the likelihood of gas hydrate occurrence near Taiwan, *Marine and Petroleum Geology*, 17, 929-936.
- Micallef, A., Masson, D.G., Berndt, C., and Stow, D.A.V., 2009, Development and mass movement processes of the north-eastern Storegga Slide: *Quaternary Science Reviews*, v. 28, S. 433-448.
- Mienert, J., Vanneste, M., Bünz, S., Andreassen, K., Haflidason, H., and Sejrup, H.P., 2005, Ocean warming and gas hydrate stability on the mid-Norwegian margin at the Storegga Slide: *Marine and Petroleum Geology*, v. 22, S. 233-244.
- Milkov, A.V., 2004, Global estimates of hydrate-bound gas in marine sediments: how much is really out there?: *Earth-Science Reviews*, v. 66, S. 183-197.
- Milkov, A.V., and Sassen, R., 2002, Economic geology of offshore gas hydrate accumulations and provinces: *Marine and Petroleum Geology*, v. 19, S. 1-11.
- , 2003, Preliminary assessment of resources and economic potential of individual gas hydrate accumulations in the Gulf of Mexico continental slope: *Marine and Petroleum Geology*, v. 20, S. 111-128.

- Nimblett, J., and Ruppel, C., 2003, Permeability evolution during the formation of gas hydrates in marine sediments: *Journal of Geophysical Research*, v. 108, p. 2420, doi: 10.1029/2001JB001650.
- Nouzé, H., Henry, P., Noble, M., Martin, V. and Pascal, G., 2004, Large gas hydrate accumulations on the eastern Nankai Trough inferred from new high-resolution 2-D seismic data, *Geophysical Research Letters* 31, doi:10.1029/2004GL019848.
- Oung, J.N., Lee, C.Y. Lee, C.S., and Kuo, C.L., 2006, Geochemical study on hydrocarbon gases in seafloor sediments, southwestern offshore Taiwan - implications in the potential occurrence of gas hydrates. *Terr. Atmos. Ocean. Sci.*, 17, 921-931.
- Paull, C.K., Ussler, W., and Dillon, W.P., 2000, Potential role of gas hydrate decomposition in generating submarine slope failures, in M., M., ed., *Natural gas hydrate in oceanic und permafrost environments*: Dordrecht, Kluwer, S. 149-156.
- Pecher, I.A., Henrys, S.A., Ellis, S., Chiswell, S.M., and Kukowski, N., 2005, Erosion of the seafloor at the top of the gas hydrate stability zone on the Hikurangi Margin, New Zealand: *Geophysical Research Letters*, v. 32, p. L24603.
- Reagan, M.T., and Moridis, G.J., 2007, Oceanic gas hydrate instability und dissociation under climate change scenarios: *Geophysical Research Letters*, v. 34, S. L22709.
- Ruppel, C., 2007, Tapping Methane Hydrates for Unconventional Natural Gas: *Elements*, v. 3, S. 193-199.
- Schnurle, P., Liu, C.-S., Hsiuan, T.-H., und Wang, T.-K., 2004, Characteristics of gas hydrate und free gas offshore southwestern Taiwan from a combined MCS/OBS data analysis: *Marine Geophysical Researches*, v. 25, S. 157-180.
- Shyu, C.-T., Chen, Y.-J., Chiang, S.-T., Liu, C.-S., 2006. Heat flow measurements over bottom simulating reflectors, offshore southwestern Taiwan. *Terrestrial, Atmospheric and Ocean Sciences*. 17, 845–869.
- Sloan, D. and Koh, C., 2007, *Clathrate Hydrates of Natural Gases*, 3. Ed., Taylor and Francis.
- Sultan, N., 2007, Comment on "Excess pore pressure resulting from methane hydrate dissociation in marine sediments: A theoretical approach" by Wenye Xu und Leonid N. Germanovich, *Journal of Geophysical Research-Solid Earth*, 112 (B2), Artikel Nr. B02103
- Sultan, N., Cochonat, P., Canals, M., Cattaneo, A., Dennielou, B., Haflidason, H., Laberg, J.S., Long, D., Mienert, J., Trincardi, F., Urgeles, R., Vorren, T.O., und Wilson, C., 2004a, Triggering mechanisms of slope instability processes und sediment failures on continental margins: a geotechnical approach: *Marine Geology*, v. 213, S. 291-321.
- Sultan, N., Cochonat, P., Foucher, J.P., und Mienert, J., 2004b, Effect of gas hydrates melting on seafloor slope instability: *Marine Geology*, v. 213, S. 379-401.
- Suppe, J., 1984, Kinematics of arc-continent collision, flipping of subduction, und back-arc spreading near Taiwan: *Memoir of the Geological Society of China*, v. 6, S. 21-33.
- Taylor, B., und Hayes, D.E., 1983, Origin und history of the south China Sea basin: *AGU Geophysical Monograph*, v. 27, S. 23-56.
- Wang, Y-S (2008) Recent development of gas hydrate investigation in Taiwan. The Taiwan-Germany Joint Symposium on Marine Gas Hydrate Exploration und Carbon Sequestration Technologies Conference.
- Westbrook, G.K., Thatcher, K.E., Rohling, E.J., Piotrowski, A.M., Pälike, H., Osborne, A.H., Nisbet, E.G., Minshull, T.A., Lanoisellé, M., James, R.H., Hühnerbach, V., Green, D., Fisher, R.E., Crocker, A.J., Chabert, A., Bolton, C., Beszczynska-Möller, A., Berndt, C., und Aquilina, A., 2009, Escape of methane gas from the seabed along the West Spitsbergen continental margin: *Geophysical Research Letters*, 36: L15608.
- Winters, W.J., Pecher, I.A., Waite, W.F., und Mason, D.H., 2004, Physical properties und rock physics models of sediment containing natural und laboratory-formed methane hydrate, *American Mineralogist* 89, 1221-1227.
- Wood, W.T., Gettrust, J.F., Chapman, N.R., Spence, G.D., und Hyndman, R.D., 2002, Decreased stability of methane hydrates in marine sediments owing to phase-boundary roughness: *Nature*, v. 420, S. 656-660.
- Xu, W., und Germanovich, L., N., 2006, Excess pore pressure resulting from methane hydrate dissociation in marine sediments: A theoretical approach: *Journal of Geophysical Research*, v. 111, S. 1-12.
- Yang, T., Jiang, S.Y., Yang, J.H., Ge, L., Wu, N.Y., Liu, J., und Chen, D.H., 2008, Dissolved inorganic carbon (DIC) und its carbon isotopic composition in sediment pore waters from the Shenhu area, northern South China Sea: *Journal of Oceanography*, v. 64, S. 303-310.

- Yang, T.F., Chuang, P.-C., Lin, S., Chen, J.-C., Wang, Y., and Chung, S.-H., 2006, Methane Venting in Gas Hydrate Potential Area Offshore of SW Taiwan: Evidence of Gas Analysis of Water Column Samples: *Terrestrial, atmospheric and ocean sciences*, v. 17, S. 933-950.
- You, C.F., J.M. Gieskes, T. Lee, T.F. Yui, and H.W. Chen, 2004. Geochemistry of mud volcano fluids in the Taiwan accretionary prism, *Applied Geochemistry*, 19, 695-707.

8. Appendices

Appendix 1: Multi-beam, Parasound

Parasound and Multi-beam: Formosa Ridge									
SO227	profile	start				End			
		date	time UTC	latitude	longitude	Date	time UTC	latitude	longitude
003-1	01	02.04.2013	18:10	22° 04.491' N	119° 22.783' E	02.04.2013	22:48	21° 59.795' N	119° 56.678' E
	02	02.04.2013	2307	22° 01.939' N	119° 58.461' E	03.04.2013	04:22	22° 07.885' N	119° 18.782' E
	03	03.04.2013	08:36	22° 04.180' N	119° 16.319' E	03.04.2013	11:30	22° 12.690' N	119° 11.824' E
	04	03.04.2013	12:00	22° 12.690' N	119° 11.824' E	03.04.2013	17:40	21° 59.885' N	119° 21.098' E
	05	03.04.2013	18:23	21° 59.780' N	119° 19.532' E	03.04.2013	22:40	22° 11.440' N	119° 13.392' E
	06	03.04.2013	23:20	22° 08.464' N	119° 15.195' E	04.04.2013	03:57	21° 59.877' N	119° 21.934' E
	07	04.04.2013	04:50	21° 59.614' N	119° 20.396' E	04.04.2013	09:00	22° 10.854' N	119° 14.482' E
	08	04.04.2013	09:46	22° 12.605' N	119° 15.099' E	04.04.2013	13:40	22° 02.734' N	119° 21.158' E
	09	04.04.2013	15:40	22° 03.358' N	119° 18.799' E	04.04.2013	16:51	22° 09.691' N	119° 15.975' E
	10	04.04.2013	04:33	22° 17.698' N	119° 35.908' E	05.04.2013	18:40	22° 11.095' N	119° 14.477' E
007-1	11	05.04.2013	22:38	22° 10.490' N	119° 14.989' E	05.04.2013	00:40	22° 05.239' N	119° 18.265' E
	12	06.04.2013	01:01	22° 04.324' N	119° 18.804' E	06.04.2013	03:40	22° 10.262' N	119° 14.271' E
	13	06.04.2013	04:00	22° 10.694' N	119° 14.910' E	06.04.2013	06:00	22° 05.418' N	119° 18.162' E
	14	06.04.2013	06:20	22° 05.265' N	119° 17.442' E	06.04.2013	08:14	22° 10.161' N	119° 14.387' E
	15	06.04.2013	08:45	22° 10.557' N	119° 15.050' E	06.04.2013	10:30	22° 05.888' N	119° 17.933' E
	16	06.04.2013	11:14	22° 05.833' N	119° 17.124' E	06.04.2013	13:04	22° 10.642' N	119° 14.164' E
	17	06.04.2013	13:40	22° 09.965' N	119° 15.390' E	06.04.2013	15:20	22° 05.527' N	119° 18.141' E
	18	06.04.2013	15:40	22° 04.914' N	119° 17.530' E	06.04.2013	17:40	22° 10.320' N	119° 14.335' E
008-1	19	07.04.2013	05:45	22° 11.682' N	119° 20.088' E	07.04.2013	08:20	22° 02.617' N	119° 14.928' E
	20	07.04.2013	08:45	22° 01.854' N	119° 14.487' E	07.04.2013	10:49	22° 05.449' N	119° 21.837' E
	21	07.04.2013	10:49	22° 05.449' N	119° 21.837' E	07.04.2013	11:20	22° 07.791' N	119° 21.629' E
	22	07.04.2013	11:20	22° 07.791' N	119° 21.629' E	07.04.2013	13:40	22° 03.648' N	119° 12.474' E

SONNE Cruise Report S0227 TAIFLUX

	23	07.04.2013	13:40	22° 03.648' N	119° 12.474' E	07.04.2013	14:00	22° 04.968' N	119° 11.815' E
	24	07.04.2013	14:00	22° 04.968' N	119° 11.815' E	07.04.2013	16:27	22° 09.273' N	119° 20.943' E
	25	07.04.2013	16:27	22° 09.273' N	119° 20.943' E	07.04.2013	16:54	22° 10.885' N	119° 20.211' E
009-1	26	08.04.2013	10:33	22° 04.627' N	119° 17.902' E	08.04.2013	12:20	22° 09.460' N	119° 14.921' E
	27	08.04.2013	12:58	22° 10.851' N	119° 14.706' E	08.04.2013	15:06	22° 05.440' N	119° 17.947' E
	28	08.04.2013	15:20	22° 05.772' N	119° 17.232' E	08.04.2013	17:20	22° 10.822' N	119° 14.546' E
	29	08.04.2013	17:40	22° 10.282' N	119° 15.323' E	08.04.2013	19:20	22° 05.970' N	119° 18.013' E
	30	08.04.2013	19:40	22° 05.363' N	119° 17.607' E	08.04.2013	21:04	22° 10.487' N	119° 14.366' E
	31	08.04.2013	22:02	22° 10.301' N	119° 15.349' E	08.04.2013	23:30	22° 06.436' N	119° 17.754' E
	32	08.04.2013	23:59	22° 05.285' N	119° 17.638' E	09.04.2013	04:00	22° 05.874' N	119° 18.139' E
	33	09.04.2013	04:00	22° 05.874' N	119° 18.139' E	09.04.2013	04:20	22° 05.147' N	119° 18.256' E
	34	09.04.2013	04:30	22° 05.094' N	119° 17.788' E	09.04.2013	06:43	22° 10.638' N	119° 14.782' E
	35	09.04.2013	07:05	22° 09.843' N	119° 15.719' E	09.04.2013	08:40	22° 05.945' N	119° 18.147' E
	36	09.04.2013	09:00	22° 05.840' N	119° 17.360' E	09.04.2013	10:47	22° 10.308' N	119° 14.578' E
010-1	37	09.04.2013	12:40	22° 08.103' N	119° 18.714' E	09.04.2013	17:59	22° 05.552' N	119° 55.160' E
	38	09.04.2013	17:59	22° 05.552' N	119° 55.160' E	09.04.2013	23:22	22° 12.559' N	119° 18.940' E
012-1	39	10.04.2013	07:24	22° 08.950' N	119° 16.575' E	10.04.2013	10:06	22° 06.899' N	119° 37.041' E
019-1	40	14.04.2013	04:40	22° 05.955' N	119° 17.322' E	14.04.2013	06:00	22° 10.158' N	119° 14.708' E
	41	14.04.2013	06:20	22° 10.637' N	119° 15.232' E	14.04.2013	07:56	22° 05.700' N	119° 18.081' E
	42	14.04.2013	08:08	22° 05.634' N	119° 17.570' E	14.04.2013	09:58	22° 10.650' N	119° 14.818' E
	43	14.04.2013	10:10	22° 10.519' N	119° 15.372' E	14.04.2013	11:34	22° 05.828' N	119° 18.274' E
	44	14.04.2013	11:53	22° 05.741' N	119° 17.540' E	14.04.2013	13:20	22° 09.695' N	119° 15.081' E
	45	14.04.2013	14:00	22° 10.291' N	119° 15.559' E	14.04.2013	15:40	22° 05.782' N	119° 18.124' E
	46	14.04.2013	16:00	22° 06.477' N	119° 17.129' E	14.04.2013	17:11	22° 10.617' N	119° 14.764' E
	47	14.04.2013	17:20	22° 10.826' N	119° 15.099' E	14.04.2013	19:20	22° 05.647' N	119° 17.881' E
	48	14.04.2013	19:50	22° 06.360' N	119° 17.245' E	14.04.2013	21:15	22° 10.543' N	119° 14.686' E
	49	14.04.2013	21:30	22° 10.744' N	119° 15.373' E	14.04.2013	23:13	22° 05.367' N	119° 18.690' E
	50	14.04.2013	23:33	22° 05.044' N	119° 17.581' E	15.04.2013	01:35	22° 10.522' N	119° 14.755' E
	51	15.04.2013	01:49	22° 10.658' N	119° 15.496' E	15.04.2013	03:21	22° 06.107' N	119° 18.286' E

SONNE Cruise Report S0227 TAIFLUX

	52	15.04.2013	03:41	22° 05.436' N	119° 17.705' E	15.04.2013	05:27	22° 10.873' N	119° 15.201' E
	53	15.04.2013	05:38	22° 10.607' N	119° 15.520' E	15.04.2013	07:00	22° 06.352' N	119° 18.171' E
	54	15.04.2013	07:20	22° 05.785' N	119° 17.705' E	15.04.2013	09:10	22° 10.590' N	119° 14.770' E
	55	15.04.2013	09:26	22° 10.586' N	119° 15.577' E	15.04.2013	10:48	22° 06.073' N	119° 18.385' E
	56	15.04.2013	11:05	22° 05.717' N	119° 17.813' E	15.04.2013	13:06	22° 10.711' N	119° 14.859' E
	57	15.04.2013	13:20	22° 10.550' N	119° 15.645' E	15.04.2013	01:41	22° 06.135' N	119° 18.378' E
	58	15.04.2013	14:55	22° 05.912' N	119° 17.771' E	15.04.2013	16:05	22° 09.557' N	119° 15.441' E
	59	15.04.2013	16:35	22° 10.912' N	119° 15.286' E	15.04.2013	18:37	22° 05.925' N	119° 18.370' E
	60	15.04.2013	18:47	22° 05.773' N	119° 17.784' E	15.04.2013	20:21	22° 10.492' N	119° 14.901' E
	61	15.04.2013	20:40	22° 10.834' N	119° 15.546' E	15.04.2013	22:12	22° 05.882' N	119° 18.297' E
	62	15.04.2013	22:28	22° 05.987' N	119° 17.754' E	15.04.2013	00:20	22° 10.609' N	119° 14.835' E
	63	16.04.2013	00:27	22° 10.185' N	119° 14.651' E	16.04.2013	01:54	22° 05.670' N	119° 17.814' E
	64	16.04.2013	02:01	22° 05.939' N	119° 18.029' E	16.04.2013	03:45	22° 10.682' N	119° 14.946' E
	65	16.04.2013	04:00	22° 10.066' N	119° 14.883' E	16.04.2013	05:00	22° 07.199' N	119° 16.827' E
	66	16.04.2013	05:35	22° 05.495' N	119° 17.807' E	16.04.2013	07:22	22° 10.426' N	119° 14.512' E
	67	16.04.2013	07:38	22° 10.451' N	119° 15.354' E	16.04.2013	08:26	22° 07.777' N	119° 16.479' E
044-1	68	29.04.2013	18:10	21° 58.550' N	119° 31.408' E	29.04.2013	21:51	21° 55.966' N	119° 58.712' E
	69	29.04.2013	22:10	21° 55.579' N	119° 56.636' E	29.04.2013	23:30	21° 58.232' N	119° 46.054' E
046-1	70	30.04.2013	01:15	21° 56.622' N	119° 43.785' E	30.04.2013	01:40	21° 56.806' N	119° 42.150' E

Parasound and Multibeam: Four Way Closure									
SO227	profile	start				End			
		date	time UTC	latitude	longitude	Date	time UTC	latitude	longitude
012-1	01	10.04.2013	14:26	22° 05.721' N	119° 47.235' E	10.04.2013	18:00	21° 55.259' N	119° 49.040' E
	02	10.04.2013	19:00	21° 56.284' N	119° 50.340' E	10.04.2013	23:00	22° 08.306' N	119° 48.262' E
	03	10.04.2013	23:40	22° 07.477' N	119° 46.188' E	11.04.2013	04:00	21° 55.728' N	119° 49.209' E
013-1	04	11.04.2013	04:40	21° 57.370' N	119° 49.443' E	11.04.2013	08:00	22° 06.913' N	119° 47.799' E
014-1	05	11.04.2013	11:00	22° 07.886' N	119° 48.236' E	11.04.2013	15:39	22° 13.222' N	119° 14.079' E
024-1	06	18.04.2013	11:06	22° 05.214' N	119° 19.508' E	18.04.2013	16:20	21° 58.105' N	119° 56.914' E
	07	18.04.2013	17:00	22° 00.682' N	119° 57.540' E	18.04.2013	20:53	22° 05.343' N	119° 28.606' E
	08	18.04.2013	21:20	22° 08.161' N	119° 28.877' E	18.04.2013	23:42	22° 05.449' N	119° 46.285' E
026-1	09	19.04.2013	05:40	22° 02.832' N	119° 49.423' E	19.04.2013	06:50	22° 03.128' N	119° 44.458' E
	10	19.04.2013	07:00	22° 03.481' N	119° 44.558' E	19.04.2013	09:12	22° 03.261' N	119° 50.550' E
	11	19.04.2013	09:25	22° 02.855' N	119° 50.043' E	19.04.2013	10:36	22° 02.955' N	119° 44.618' E
	12	19.04.2013	11:00	22° 03.508' N	119° 44.552' E	19.04.2013	13:06	22° 03.391' N	119° 50.429' E
	13	19.04.2013	13:20	22° 02.837' N	119° 50.335' E	19.04.2013	14:40	22° 03.105' N	119° 44.422' E
	14	19.04.2013	15:00	22° 03.540' N	119° 45.096' E	19.04.2013	17:00	22° 03.419' N	119° 50.404' E
	15	19.04.2013	17:16	22° 02.933' N	119° 50.395' E	19.04.2013	18:25	22° 03.127' N	119° 44.631' E
	16	19.04.2013	18:41	22° 03.568' N	119° 45.183' E	19.04.2013	20:35	22° 03.422' N	119° 50.534' E
	17	19.04.2013	20:50	22° 02.959' N	119° 50.161' E	19.04.2013	22:00	22° 03.052' N	119° 44.762' E
	18	19.04.2013	22:20	22° 03.608' N	119° 44.860' E	20.04.2013	00:20	22° 03.516' N	119° 50.345' E
	19	20.04.2013	00:37	22° 02.994' N	119° 50.105' E	20.04.2013	01:44	22° 03.088' N	119° 44.804' E
	20	20.04.2013	01:59	22° 03.584' N	119° 44.627' E	20.04.2013	04:02	22° 03.562' N	119° 49.912' E
	21	20.04.2013	04:25	22° 03.016' N	119° 50.065' E	20.04.2013	05:32	22° 03.533' N	119° 44.454' E
	22	20.04.2013	05:51	22° 03.678' N	119° 44.975' E	20.04.2013	07:51	22° 03.519' N	119° 50.298' E
	23	20.04.2013	07:51	22° 03.519' N	119° 50.298' E	20.04.2013	09:13	22° 03.178' N	119° 44.581' E
	24	20.04.2013	09:30	22° 03.720' N	119° 44.827' E	20.04.2013	11:33	22° 03.622' N	119° 50.450' E

SONNE Cruise Report S0227 TAIFLUX

	25	20.04.2013	11:49	22° 03.099' N	119° 50.114' E	20.04.2013	12:57	22° 03.200' N	119° 44.643' E
	26	20.04.2013	13:20	22° 03.748' N	119° 45.184' E	20.04.2013	15:20	22° 03.660' N	119° 50.292' E
	27	20.04.2013	15:37	22° 03.141' N	119° 50.299' E	20.04.2013	16:48	22° 03.311' N	119° 44.590' E
	28	20.04.2013	17:01	22° 03.787' N	119° 44.822' E	20.04.2013	18:40	22° 03.702' N	119° 49.802' E
	29	20.04.2013	19:15	22° 03.178' N	119° 49.763' E	20.04.2013	20:36	22° 03.429' N	119° 44.478' E
	30	20.04.2013	20:49	22° 03.820' N	119° 44.771' E	20.04.2013	23:06	22° 03.693' N	119° 50.497' E
	31	20.04.2013	23:21	22° 03.206' N	119° 50.066' E	21.04.2013	00:40	22° 03.300' N	119° 44.861' E
	32	21.04.2013	01:00	22° 03.835' N	119° 44.857' E	21.04.2013	02:56	22° 03.751' N	119° 50.452' E
	33	21.04.2013	03:10	22° 03.247' N	119° 49.901' E	21.04.2013	04:40	22° 03.348' N	119° 43.468' E
027-1	34	21.04.2013	07:40	22° 06.387' N	119° 44.613' E	21.04.2013	09:40	22° 59.548' N	119° 45.958' E
	35	21.04.2013	09:57	22° 59.698' N	119° 46.811' E	21.04.2013	11:58	22° 06.457' N	119° 45.616' E
	36	21.04.2013	12:09	22° 06.410' N	119° 46.235' E	21.04.2013	14:10	21° 59.711' N	119° 47.902' E
	37	21.04.2013	14:22	21° 59.991' N	119° 48.536' E	21.04.2013	16:18	22° 06.631' N	119° 47.215' E
	38	21.04.2013	16:33	22° 06.784' N	119° 48.072' E	21.04.2013	18:33	21° 59.983' N	119° 49.540' E
	39	21.04.2013	18:45	22° 00.196' N	119° 50.203' E	21.04.2013	20:30	22° 06.140' N	119° 48.978' E
	40	21.04.2013	20:50	22° 06.530' N	119° 49.257' E	21.04.2013	21:48	22° 03.953' N	119° 51.370' E
	41	21.04.2013	21:48	22° 03.953' N	119° 51.370' E	22.04.2013	00:08	22° 02.863' N	119° 43.240' E
	42	22.04.2013	00:08	22° 02.863' N	119° 43.240' E	22.04.2013	02:20	22° 04.427' N	119° 43.745' E
028-1	43	22.04.2013	02:40	22° 03.886' N	119° 44.600' E	22.04.2013	04:20	22° 03.802' N	119° 50.185' E
	44	22.04.2013	04:40	22° 03.280' N	119° 49.784' E	22.04.2013	06:04	22° 03.825' N	119° 44.416' E
	45	22.04.2013	06:30	22° 03.910' N	119° 45.744' E	22.04.2013	08:02	22° 03.831' N	119° 50.430' E
	46	22.04.2013	08:18	22° 03.306' N	119° 49.934' E	22.04.2013	09:24	22° 03.426' N	119° 44.556' E
	47	22.04.2013	09:38	22° 03.966' N	119° 44.666' E	22.04.2013	11:20	22° 03.868' N	119° 50.083' E
	48	22.04.2013	11:39	22° 03.346' N	119° 50.149' E	22.04.2013	12:52	22° 03.456' N	119° 44.572' E
	49	22.04.2013	13:08	22° 03.997' N	119° 44.808' E	22.04.2013	15:00	22° 03.898' N	119° 50.166' E
	50	22.04.2013	15:20	22° 03.286' N	119° 50.529' E	22.04.2013	16:20	22° 03.643' N	119° 47.339' E
	51	22.04.2013	17:35	22° 03.854' N	119° 47.917' E	22.04.2013	18:00	22° 07.300' N	119° 50.162' E
029-1	52	22.04.2013	18:00	22° 07.300' N	119° 50.162' E	22.04.2013	18:30	22° 07.329' N	119° 53.584' E
	53	22.04.2013	18:30	22° 07.329' N	119° 53.584' E	22.04.2013	19:52	22° 11.484' N	119° 45.899' E

SONNE Cruise Report S0227 TAIFLUX

	54	22.04.2013	19:52	22° 11.484' N	119° 45.899' E	22.04.2013	21:00	22° 12.901' N	119° 37.591' E
	55	22.04.2013	21:00	22° 12.901' N	119° 37.591' E	22.04.2013	22:20	22° 13.521' N	119° 30.013' E
	56	22.04.2013	22:20	22° 13.521' N	119° 30.013' E	23.04.2013	00:16	22° 03.353' N	119° 47.376' E
049-1	57	30.04.2013	16:56	22° 03.343' N	119° 57.556' E	30.04.2013	17:48	22° 03.964' N	119° 51.143' E
	58	30.04.2013	17:48	22° 03.964' N	119° 51.143' E	30.04.2013	17:59	22° 04.983' N	119° 50.370' E
	59	30.04.2013	17:59	22° 04.983' N	119° 50.370' E	30.04.2013	18:48	22° 04.290' N	119° 56.318' E
	60	30.04.2013	18:48	22° 04.290' N	119° 56.318' E	30.04.2013	19:32	22° 07.829' N	119° 52.654' E
	61	30.04.2013	19:32	22° 07.829' N	119° 52.654' E	30.04.2013	19:53	22° 08.209' N	119° 50.081' E
	62	30.04.2013	19:53	22° 08.209' N	119° 50.081' E	30.04.2013	20:51	22° 08.584' N	119° 42.650' E
	63	30.04.2013	20:51	22° 08.584' N	119° 42.650' E	30.04.2013	22:29	22° 10.215' N	119° 30.463' E
	64	30.04.2013	22:29	22° 10.215' N	119° 30.463' E	30.04.2013	23:22	22° 11.499' N	119° 29.697' E
	65	30.04.2013	23:22	22° 11.499' N	119° 29.697' E	01.05.2013	01:12	22° 09.717' N	119° 43.332' E
	66	01.05.2013	01:12	22° 09.717' N	119° 43.332' E	01.05.2013	01:23	22° 10.345' N	119° 44.440' E
	67	01.05.2013	01:23	22° 10.345' N	119° 44.440' E	01.05.2013	02:33	22° 11.572' N	119° 36.558' E
052-1	68	01.05.2013	11:44	21° 56.899' N	119° 31.377' E	01.05.2013	13:35	21° 55.280' N	119° 44.822' E
	69	01.05.2013	13:35	21° 55.280' N	119° 44.822' E	01.05.2013	13:45	21° 54.793' N	119° 45.913' E
	70	01.05.2013	13:45	21° 54.793' N	119° 45.913' E	01.05.2013	15:30	21° 54.373' N	119° 58.825' E

Appendix 2: Sidescan Sonar profiles

Sidescan Sonar: Formosa Ridge									
SO227	profile	start				End			
		date	time UTC	latitude	longitude	Date	time UTC	latitude	longitude
004-1	01	03.04.2013	08:36	22° 04.180' N	119° 16.319' E	03.04.2013	11:30	22° 12.690' N	119° 11.824' E
	02	03.04.2013	12:00	22° 12.690' N	119° 11.824' E	03.04.2013	17:40	21° 59.885' N	119° 21.098' E
	03	03.04.2013	18:23	21° 59.780' N	119° 19.532' E	03.04.2013	22:40	22° 11.440' N	119° 13.392' E
	04	03.04.2013	23:20	22° 08.464' N	119° 15.195' E	04.04.2013	03:57	21° 59.877' N	119° 21.934' E
	05	04.04.2013	04:50	21° 59.614' N	119° 20.396' E	04.04.2013	09:00	22° 10.854' N	119° 14.482' E
	06	04.04.2013	09:46	22° 12.605' N	119° 15.099' E	04.04.2013	13:40	22° 02.734' N	119° 21.158' E
	07	04.04.2013	15:40	22° 03.358' N	119° 18.799' E	04.04.2013	16:51	22° 09.691' N	119° 15.975' E

Sidescan Sonar: Four Way Closure									
SO227	profile	start				End			
		date	time UTC	latitude	longitude	Date	time UTC	latitude	longitude
013-1	01	10.04.2013	14:26	22° 05.721' N	119° 47.235' E	10.04.2013	18:00	21° 55.259' N	119° 49.040' E
	02	10.04.2013	19:00	21° 56.284' N	119° 50.340' E	10.04.2013	23:00	22° 08.306' N	119° 48.262' E
	03	10.04.2013	23:40	22° 07.477' N	119° 46.188' E	11.04.2013	04:00	21° 55.728' N	119° 49.209' E
	04	11.04.2013	04:40	21° 57.370' N	119° 49.443' E	11.04.2013	08:00	22° 06.913' N	119° 47.799' E

Appendix 3: OBS stations

OBS stations: Formosa Ridge							
OBS	Profile 1			deployment		recovery	
	latitude	longitude	depth (m)	date	time UTC	Date	time UTC
OBS 1	22° 06.605' N	119° 17.534' E	1200	05.04.2013	06:40	10.04.2013	01:06
OBS 2	22° 06.342' N	119° 17.694' E	1198	05.04.2013	06:53	10.04.2013	01:39
OBS 3	22° 06.197' N	119° 17.446' E	1262	05.04.2013	07:09	10.04.2013	02:02
OBS 4	22° 06.466' N	119° 17.308' E	1229	05.04.2013	07:23	10.04.2013	02:25
OBS 5	22° 06.681' N	119° 16.989' E	1229	05.04.2013	07:34	10.04.2013	02:51
OBS 6	22° 06.989' N	119° 16.835' E	1298	05.04.2013	07:45	10.04.2013	03:14
OBS 7	22° 07.710' N	119° 16.783' E	1273	05.04.2013	08:04	10.04.2013	04:03
OBS 8	22° 07.944' N	119° 16.654' E	1268	05.04.2013	08:16	10.04.2013	04:24
OBS 9	22° 08.182' N	119° 16.531' E	1209	05.04.2013	08:37	10.04.2013	04:59
OBS 10	22° 08.510' N	119° 16.257' E	1119	05.04.2013	08:45	10.04.2013	05:42
OBS 11	22° 09.027' N	119° 15.971' E	1141	05.04.2013	09:02	10.04.2013	06:14
OBS 12	22° 09.305' N	119° 15.814' E	1147	05.04.2013	09:16	10.04.2013	06:41

OBS stations: Four Way Closure							
OBS	Profile 2			deployment		recovery	
	latitude	longitude	depth (m)	date	time UTC	Date	time UTC
OBS 1	22° 02.977' N	119° 45.309' E	1974	19.04.2013	00:21	24.04.2013	03:57
OBS 2	22° 03.069' N	119° 45.710' E	1888	19.04.2013	00:37	24.04.2013	03:19
OBS 3	22° 03.119' N	119° 46.055' E	1767	19.04.2013	00:56	24.04.2013	02:39
OBS 4	22° 03.196' N	119° 46.462' E	1707	19.04.2013	01:13	24.04.2013	02:02
OBS 5	22° 03.295' N	119° 46.906' E	1678	19.04.2013	01:31	24.04.2013	01:29
OBS 6	22° 03.367' N	119° 47.356' E	1488	19.04.2013	01:47	24.04.2013	00:54

OBS 7	22° 03.481' N	119° 47.875' E	1351	19.04.2013	02:08	24.04.2013	00:10
OBS 8	22° 03.536' N	119° 48.253' E	1408	19.04.2013	02:25	23.04.2013	23:35
OBS 9	22° 03.619' N	119° 48.698' E	1570	19.04.2013	02:44	23.04.2013	23:04
OBS 10	22° 03.708' N	119° 49.120' E	1608	19.04.2013	03:00	23.04.2013	22:33
OBS 11	22° 03.774' N	119° 49.463' E	1630	19.04.2013	03:16	23.04.2013	22:02
OBS 12	22° 03.845' N	119° 49.805' E	1644	19.04.2013	03:33	23.04.2013	21:23

Appendix 4: Seismic profiles

4.1. 3D seismic profiles

3D seismic: Formosa Ridge									
SO227	profile	start				End			
		date	time UTC	latitude	longitude	Date	time UTC	latitude	longitude
		P1100							
007-1	01	05.04.2013	16:28	22° 05.576' N	119° 17.156' E	05.04.2013	18:17	22° 10.147' N	119° 14.311' E
	02	05.04.2013	22:38	22° 10.449' N	119° 15.009' E	06.04.2013	01:00	22° 04.473' N	119° 18.740' E
	03	06.04.2013	01:20	22° 04.246' N	119° 18.041' E	06.04.2013	03:40	22° 10.176' N	119° 14.322' E
	04	06.04.2013	04:07	22° 10.331' N	119° 15.130' E	06.04.2013	05:50	22° 05.863' N	119° 17.910' E
	05	06.04.2013	06:28	22° 05.575' N	119° 17.239' E	06.04.2013	08:19	22° 10.369' N	119° 14.246' E
	06	06.04.2013	08:52	22° 10.185' N	119° 15.255' E	06.04.2013	09:30	22° 05.870' N	119° 17.948' E
		P1200							
	07	06.04.2013	11:14	22° 05.782' N	119° 17.173' E	06.04.2013	12:54	22° 10.189' N	119° 14.408' E
	08	06.04.2013	14:05	22° 08.781' N	119° 16.095' E	06.04.2013	15:15	22° 05.689' N	119° 18.042' E
	09	06.04.2013	15:55	22° 05.615' N	119° 17.276' E	06.04.2013	17:31	22° 09.872' N	119° 14.602' E
		P1300							
009-1	08-2	08.04.2013	03:25	22° 10.310' N	119° 15.170' E	08.04.2013	05:09	22° 05.861' N	119° 17.987' E
		P1400							

SONNE Cruise Report SO227 TAIFLUX

	09-2	08.04.2013	10:28	22° 04.328' N	119° 18.078' E	08.04.2013	12:35	22° 10.233' N	119° 04.418' E
	08-3	08.04.2013	13:10	22° 10.451' N	119° 15.048' E	08.04.2013	14:55	22° 05.853' N	119° 17.925' E
	11	08.04.2013	15:20	22° 05.772' N	119° 17.230' E	08.04.2013	17:03	22° 10.213' N	119° 14.472' E
	12	08.04.2013	17:33	22° 10.541' N	119° 15.160' E	08.04.2013	19:20	22° 05.945' N	119° 18.023' E
	13	08.04.2013	19:47	22° 05.637' N	119° 17.372' E	08.04.2013	21:33	22° 10.223' N	119° 14.505' E
	14	08.04.2013	21:57	22° 10.561' N	119° 15.186' E	08.04.2013	23:40	22° 05.957' N	119° 18.055' E
	15	09.04.2013	00:07	22° 05.561' N	119° 17.391' E	09.04.2013	01:55	22° 10.302' N	119° 14.498' E
	16	09.04.2013	01:55	22° 10.577' N	119° 15.214' E	09.04.2013	04:00	22° 05.966' N	119° 18.088' E
	17	09.04.2013	04:32	22° 05.100' N	119° 17.779' E	09.04.2013	06:32	22° 10.245' N	119° 14.572' E
	18	09.04.2013	06:52	22° 10.573' N	119° 15.271' E	09.04.2013	08:37	22° 05.987' N	119° 18.122' E
	19	09.04.2013	09:01	22° 05.687' N	119° 17.450' E	09.04.2013	10:48	22° 10.346' N	119° 14.575' E
	P1500								
019-1	20	14.04.2013	04:34	22°07.700 ' N	119°17.492' E	14.04.2013	06:03	22°10.287' N	119°14.632' E
	21	14.04.2013	06:18	22°10.515' N	119° 15.341' E	14.04.2013	07:50	22°05.994' N	119°18.149' E
	22	14.04.2013	08:10	22°05.766' N	119°17.481' E	14.04.2013	09:49	22°10.286' N	119°14.664' E
	23	14.04.2013	10:08	22°10.591' N	119°15.322' E	14.04.2013	11:31	22°06.023' N	119°18.173' E
	24	14.04.2013	11:54	22°05.721' N	119°17.555' E	14.04.2013	13:35	22°10.373' N	119°14.655' E
	25	14.04.2013	13:55	22°10.593' N	119°15.362' E	14.04.2013	15:35	22°06.004' N	119°18.226' E
	26	14.04.2013	15:52	22°06.068' N	119°17.380' E	14.04.2013	17:07	22°10.406' N	119°14.762' E
	27	14.04.2013	17:27	22°10.644' N	119°15.366' E	14.04.2013	19:09	22°06.053' N	119°18.289' E
	28	14.04.2013	19:27	22°05.810' N	119°17.557' E	14.04.2013	21:11	22°10.344' N	119°14.752' E
	29	14.04.2013	21:31	22°10.669' N	119°15.409' E	14.04.2013	23:00	22°06.054' N	119°18.282' E
	30	15.04.2013	00:03	22°06.422' N	119°17.233' E	15.04.2013	01:33	22°10.380' N	119°14.768' E
	31	15.04.2013	01:53	22°10.399' N	119°15.624' E	15.04.2013	03:23	22°06.060' N	119°18.334' E
	32	15.04.2013	03:52	22°06.070' N	119°17.492' E	15.04.2013	05:14	22°10.402' N	119°14.791' E
	33	15.04.2013	05:34	22°10.690' N	119°15.463' E	15.04.2013	07:05	22°06.089' N	119°18.327' E
	34	15.04.2013	07:20	22°05.806' N	119°17.679' E	15.04.2013	09:05	22°10.383' N	119°14.846' E
	35	15.04.2013	09:24	22°10.714' N	119°15.496' E	15.04.2013	10:48	22°06.117' N	119°18.359' E

SONNE Cruise Report SO227 TAIFLUX

	36	15.04.2013	11:08	22°05.818' N	119°17.740' E	15.04.2013	13:01	22°10.458' N	119°14.839' E
	37	15.04.2013	13:18	22°10.703' N	119°15.555' E	15.04.2013	14:42	22°06.134' N	119°18.380' E
	38	15.04.2013	14:57	22°06.018' N	119°17.646' E	15.04.2013	16:21	22°10.448' N	119°14.882' E
	39	15.04.2013	16:44	22°10.743' N	119°15.541' E	15.04.2013	18:33	22°06.159' N	119°18.408' E
	40	15.04.2013	18:52	22°06.052' N	119°17.657' E	15.04.2013	20:20	22°10.439' N	119°14.935' E
	41	15.04.2013	20:41	22°10.746' N	119°15.598' E	15.04.2013	22:04	22°06.336' N	119°18.047' E
	42	15.04.2013	22:25	22°05.863' N	119°17.829' E	16.04.2013	00:13	22°10.485' N	119°14.950' E
	43	16.04.2013	00:26	22°10.218' N	119°14.632' E	16.04.2013	01:50	22°05.800' N	119°17.596' E
	44	16.04.2013	02:03	22°05.993' N	119°17.988' E	16.04.2013	03:44	22°10.608' N	119°15.070' E
	45	16.04.2013	03:55	22°10.313' N	119°14.742' E	16.04.2013	03:59	22°10.145' N	119°14.839' E
	46	16.04.2013	04:01	22°10.041' N	119°14.896' E	16.04.2013	05:24	22°06.100' N	119°17.452' E
	47	16.04.2013	05:47	22°05.627' N	119°17.336' E	16.04.2013	07:16	22°10.101' N	119°14.519' E
	48	16.04.2013	07:35	22°10.492' N	119°15.101' E	16.04.2013	08:24	22°07.881' N	119°16.420' E

3D seismic: Four Way Closure									
SO227	profile	start				end			
		date	time	latitude	longitude	Date	time UTC	latitude	longitude
		P2100							
026-1	01	19.04.2013	05:53	22° 02.845' N	119° 48.585' E	19.04.2013	06:43	22° 02.917' N	119° 44.808' E
	02	19.04.2013	07:06	22° 03.469' N	119° 44.863' E	19.04.2013	09:05	22° 02.276' N	119° 50.279' E
	03	19.04.2013	09:23	22° 02.848' N	119° 50.228' E	19.04.2013	10:34	22° 02.946' N	119° 44.796' E
	04	19.04.2013	11:05	22° 03.506' N	119° 44.836' E	19.04.2013	13:03	22° 03.417' N	119° 50.307' E
	05	19.04.2013	13:24	22° 02.892' N	119° 49.920' E	19.04.2013	14:35	22° 02.978' N	119° 44.800' E
	06	19.04.2013	14:55	22° 03.542' N	119° 44.805' E	19.04.2013	16:55	22° 03.449' N	119° 50.285' E
	07	19.04.2013	17:11	22° 02.925' N	119° 50.240' E	19.04.2013	18:21	22° 03.013' N	119° 44.822' E
	08	19.04.2013	18:37	22° 03.571' N	119° 44.877' E	19.04.2013	20:30	22° 03.481' N	119° 50.360' E
	09	19.04.2013	20:49	22° 02.961' N	119° 50.128' E	19.04.2013	22:00	22° 03.053' N	119° 04.677' E
	10	19.04.2013	22:20	22° 03.608' N	119° 44.887' E	20.04.2013	00:20	22° 03.520' N	119° 50.254' E

SONNE Cruise Report SO227 TAIFLUX

	11	20.04.2013	00:35	22° 03.001' N	119° 50.141' E	20.04.2013	01:45	22° 03.088' N	119° 44.780' E
	12	20.04.2013	02:04	22° 03.644' N	119° 44.861' E	20.04.2013	04:10	22° 03.532' N	119° 50.347' E
	13	20.04.2013	04:28	22° 03.034' N	119° 49.980' E	20.04.2013	05:30	22° 03.119' N	119° 44.824' E
	14	20.04.2013	05:48	22° 03.682' N	119° 44.861' E	20.04.2013	07:47	22° 03.587' N	119° 50.297' E
	15	20.04.2013	08:03	22° 03.054' N	119° 50.141' E	20.04.2013	09:10	22° 03.156' N	119° 44.789' E
	16	20.04.2013	09:30	22° 03.720' N	119° 44.849' E	20.04.2013	11:30	22° 03.627' N	119° 50.299' E
	17	20.04.2013	11:45	22° 03.100' N	119° 50.107' E	20.04.2013	13:05	22° 03.192' N	119° 44.779' E
	18	20.04.2013	13:10	22° 03.748' N	119° 44.830' E	20.04.2013	15:21	22° 03.659' N	119° 50.354' E
	19	20.04.2013	15:40	22° 03.138' N	119° 50.219' E	20.04.2013	16:45	22° 03.223' N	119° 44.814' E
	20	20.04.2013	17:01	22° 03.788' N	119° 44.867' E	20.04.2013	18:55	22° 03.696' N	119° 50.296' E
	21	20.04.2013	19:11	22° 03.171' N	119° 50.187' E	20.04.2013	20:32	22° 03.277' N	119° 44.613' E
	22	20.04.2013	20:50	22° 03.819' N	119° 44.840' E	20.04.2013	23:03	22° 03.725' N	119° 50.325' E
	23	20.04.2013	23:18	22° 03.183' N	119° 50.244' E	21.04.2013	00:40	22° 03.301' N	119° 44.799' E
	24	21.04.2013	01:00	22° 03.842' N	119° 44.899' E	21.04.2013	02:54	22° 03.766' N	119° 50.327' E
	25	21.04.2013	03:07	22° 03.238' N	119° 50.192' E	21.04.2013	05:22	22° 03.410' N	119° 40.200' E
	P2200/1								
028-1	26	22.04.2013	02:46	22° 03.887' N	119° 44.889' E	22.04.2013	04:23	22° 03.798' N	119° 50.310' E
	27	22.04.2013	04:35	22° 03.275' N	119° 50.239' E	22.04.2013	05:52	22° 03.369' N	119° 44.825' E
	28	22.04.2013	06:13	22° 03.928' N	119° 44.864' E	22.04.2013	08:00	22° 03.839' N	119° 50.383' E
	29	22.04.2013	08:16	22° 03.277' N	119° 50.069' E	22.04.2013	09:21	22° 03.401' N	119° 44.853' E
	30	22.04.2013	09:42	22° 03.963' N	119° 44.861' E	22.04.2013	11:24	22° 03.869' N	119° 50.316' E
	31	22.04.2013	11:38	22° 03.334' N	119° 50.270' E	22.04.2013	12:49	22° 03.437' N	119° 44.795' E
	P2200/2								
	32	22.04.2013	13:10	22° 03.996' N	119° 44.856' E	22.04.2013	15:03	22° 03.905' N	119° 50.380' E
	33	22.04.2013	15:30	22° 02.999' N	119° 49.922' E	22.04.2013	16:01	22° 03.076' N	119° 47.453' E

4.2. Air gun shooting for OBS

Air gun shooting for OBS: Formosa Ridge (SO227/008-1)									
SO227	profile	start				End			
		date	time UTC	latitude	longitude	Date	time UTC	latitude	longitude
008-1	OBS-P01	07.04.2013	05:45	22° 11.682' N	119° 20.088' E	07.04.2013	08:20	22° 02.617' N	119° 14.928' E
	OBS-P02	07.04.2013	08:45	22° 01.854' N	119° 14.487' E	07.04.2013	10:49	22° 05.449' N	119° 21.837' E
	OBS-P03	07.04.2013	10:49	22° 05.449' N	119° 21.837' E	07.04.2013	11:20	22° 07.791' N	119° 21.629' E
	OBS-P04	07.04.2013	11:20	22° 07.791' N	119° 21.629' E	07.04.2013	13:40	22° 03.648' N	119° 12.474' E
	OBS-P05	07.04.2013	13:40	22° 03.648' N	119° 12.474' E	07.04.2013	14:00	22° 04.968' N	119° 11.815' E
	OBS-P06	07.04.2013	14:00	22° 04.968' N	119° 11.815' E	07.04.2013	16:27	22° 09.273' N	119° 20.943' E
	OBS-P07	07.04.2013	16:27	22° 09.273' N	119° 20.943' E	07.04.2013	16:54	22° 10.885' N	119° 20.211' E
	OBS-P08	07.04.2013	16:54	22° 10.885' N	119° 20.211' E	07.04.2013	19:13	22° 06.764' N	119° 11.152' E
	OBS-P09	07.04.2013	19:30	22° 06.806' N	119° 10.155' E	07.04.2013	22:00	22° 06.472' N	119° 21.958' E

Air gun shooting for OBS: Four Way Closure									
SO227	profile	start				End			
		date	time	latitude	longitude	Date	time	latitude	longitude
027-1	OBS-P01	21.04.2013	07:39	22° 06.405' N	119° 44.612' E	21.04.2013	09:42	21° 59.424' N	119° 46.018' E
	OBS-P02	21.04.2013	09:55	21° 59.549' N	119° 46.819' E	21.04.2013	11:54	22° 06.387' N	119° 45.398' E
	OBS-P03	21.04.2013	12:07	22° 06.505' N	119° 46.206' E	21.04.2013	14:09	21° 59.690' N	119° 47.826' E
	OBS-P04	21.04.2013	14:21	21° 59.853' N	119° 48.513' E	21.04.2013	16:18	22° 06.631' N	119° 47.217' E
	OBS-P05	21.04.2013	16:35	22° 06.743' N	119° 48.132' E	21.04.2013	18:31	22° 00.016' N	119° 49.458' E
	OBS-P06	21.04.2013	18:45	22° 00.170' N	119° 50.199' E	21.04.2013	20:40	22° 06.724' N	119° 48.862' E
	OBS-P07	21.04.2013	21:45	22° 04.091' N	119° 51.501' E	22.04.2013	00:05	22° 02.645' N	119° 43.459' E

4.3. P-Cable recording parameters

P-Cable 3D Survey	number of streamers	channel interval (m)	rec. sample rate (Hz):	rec. trace length (ms)	delay (ms)	stretch str. 1 (m)	stretch str. 2-14 (m)	remarks
Formosa Ridge								
P1100	14	1.5625	1000	4000	30	10	5	
P1200	14	1.5625	1000	4000	30	10	5	
P1300	13	1.5625	1000	4000	30	10	5	signal of streamer #5 lost
P1400	14	1.5625	1000	4000	30	10	5	
P1500	14	1.5625	1000	4000	30	10	5	
Four Way Closure								
P2100	14	1.5625	1000	4000	30	10	5	
P2200/1	14	1.5625	1000	4000	30	10	5	
P2200/2	12	1.5625	1000	4000	30	10	5	signal of streamer #13 and #14 lost

4.4. OBS recording parameter

OBS recording parameter: Formosa Ridge							
station	sample rate	gain	skew after sync.	file size	error messages	coordinates deployment	coordinates recovery
OBS 1	500 Hz	7 21 21 21	-148 ms	1388 MB	resuming recording; battery low	22° 06.605' N 119° 17.534' E	22° 06.647' N 119° 17.284' E
OBS 2	500 Hz	7 21 21 21	-7 ms	0 MB	disk write error; skipping data due to slow card; boot delay;	22° 06.342' N 119° 17.694' E	22° 06.403' N 119° 17.543' E
OBS 3	500 Hz	7 21 21 21	-148 ms	986 MB	battery low	22° 06.197' N 119° 17.446' E	22° 06.330' N 119° 17.319' E
OBS 4	500 Hz	7 21 21 21	-56 ms	1370 MB	None	22° 06.466' N 119° 17.308' E	22° 06.490' N 119° 17.131' E
OBS 5	500 Hz	5 21 21 21	9 ms	1420 MB	None	22° 06.681' N 119° 16.989' E	22° 06.664' N 119° 16.892' E
OBS 6	500 Hz	7 21 21 21	23 ms	0 MB	disk write error	22° 06.989' N 119° 16.835' E	22° 06.994' N 119° 16.754' E
OBS 7	500 Hz	7 21 21 21	3 ms	1514 MB	None	22° 07.710' N 119° 16.783' E	22° 07.690' N 119° 16.790' E
OBS 8	500 Hz	7 21 21 21	-8 ms	1207 MB	None	22° 07.944' N 119° 16.654' E	22° 08.070' N 119° 16.185' E
OBS 9	500 Hz	7 21 21 21	17 ms	1259 MB	None	22° 08.182' N 119° 16.531' E	22° 08.090' N 119° 16.432' E
OBS 10	500 Hz	5 21 21 21	-153 ms	1373 MB	None	22° 08.510' N 119° 16.257' E	22° 08.417' N 119° 16.137' E
OBS 11	500 Hz	5 21 21 21	-251 ms	1122 MB	resuming recording	22° 09.027' N 119° 15.971' E	22° 08.937' N 119° 15.973' E
OBS 12	500 Hz	7 21 21 21	20 ms	1265 MB	battery low	22° 09.305' N 119° 15.814' E	22° 09.249' N 119° 15.782' E
Shot logger	1000 Hz	1	-149 ms	414 MB	None		

OBS recording parameter: Four Way Closure							
station	sample rate	gain	skew after sync.	file size	error messages	coordinates deployment	coordinates recovery
OBS 1	1000 Hz	7 21 21 21	-68 ms	2.83 GB	None	22° 02.977' N 119° 45.309' E	22° 02.980' N 119° 45.320' E
OBS 2	1000 Hz	7 21 21 21	-4 ms	2.5 GB	battery low (23.04.13/13:58)	22° 03.069' N 119° 45.710' E	22° 02.938' N 119° 45.398' E
OBS 3	1000 Hz	7 21 21 21	-251 ms	2.84 GB	None	22° 03.119' N 119° 46.055' E	22° 03.145' N 119° 45.914' E
OBS 4	1000 Hz	7 21 21 21	-62 ms	3.13 GB	None	22° 03.196' N 119° 46.462' E	22° 03.179' N 119° 46.304' E
OBS 5	1000 Hz	5 21 21 21	9 ms	3.13 GB	None	22° 03.295' N 119° 46.906' E	22° 03.290' N 119° 46.910' E
OBS 6	1000 Hz	5 23 23 23	-12 ms	2.73 GB	None	22° 03.367' N 119° 47.356' E	22° 03.370' N 119° 47.360' E
OBS 7	1000 Hz	7 21 21 21	4 ms	2.99 GB	none	22° 03.481' N 119° 47.875' E	22° 03.470' N 119° 47.860' E
OBS 8	1000 Hz	7 21 21 21	-7 ms	3.08 GB	None	22° 03.536' N 119° 48.253' E	22° 03.600' N 119° 47.998' E
OBS 9	1000 Hz	7 21 21 21	22 ms	2.84 GB	None	22° 03.619' N 119° 48.698' E	22° 03.682' N 119° 48.415' E
OBS 10	1000 Hz	5 21 21 21	-32 ms	3.03 GB	None	22° 03.708' N 119° 49.120' E	22° 03.783' N 119° 48.786' E
OBS 11	1000 Hz	5 21 21 21	-149 ms	2.49 GB	battery low (23.04.13/22:15)	22° 03.774' N 119° 49.463' E	22° 03.875' N 119° 49.166' E
OBS 12	1000 Hz	7 21 21 21	19 ms	2.70 GB	None	22° 03.845' N 119° 49.805' E	22° 03.947' N 119° 49.471' E
Shot logger	1000 Hz	1	-15 ms	0.42 GB	None		

Appendix 5: Controlled source EM**5.1: OBEM stations**

OBEM stations: Formosa Ridge							
OBEM	Profile 1			deployment		Recovery	
	latitude	longitude	depth (m)	date	time UTC	Date	time UTC
EM01	22° 05.128' N	119° 18.721' E	1458	12.04.2013	03:15	18.04.2013	10:12
EM02	22° 05.379' N	119° 18.421' E	1400	12.04.2013	06:57	18.04.2013	08:53
EM03	22° 05.385' N	119° 18.155' E	1330	12.04.2013	08:44	18.04.2013	09:32
EM04	22° 05.851' N	119° 18.079' E	1265	12:04:2013	10:24	18.04.2013	09:11
EM05	22° 06.123' N	119° 17.875' E	1240	12.04.2013	12:05	18.04.2013	08:48
EM06	22° 06.361' N	119° 17.686' E	1200	12.04.2013	13:40	18.04.2013	08:20
EM07	22° 06.573' N	119° 17.475' E	1160	12.04.2013	15:06	18.04.2013	07:59
EM08	22° 06.589' N	119° 17.486' E	1150	12.04.2013	16:35	18.04.2013	07:37
EM09	22° 07.044' N	119° 17.118' E	1200	12.04.2013	18:07	18.04.2013	07:22
EM10	22° 07.310' N	119° 16.941' E	1260	12.04.2013	19:45	18.04.2013	06:59
EM11	22° 07.557' N	119° 16.773' E	1260	12.04.2013	21:13	18.04.2013	06:21
EM12	22° 07.891' N	119° 16.679' E	1270	12.04.2013	23:01	18.04.2013	05:53

OBEM stations: Four Way Closure							
OBEM	Profile 2			deployment		Recovery	
	latitude	longitude	depth (m)	date	time UTC	Date	time UTC
EM01	22° 03.328' N	119° 47.397' E	1450	23.04.2013	01:33	27.04.2013	02:03
EM02	22° 03.421' N	119° 47.685' E	1375	23.04.2013	03:19	27.04.2013	02:35
EM03	22° 03.452' N	119° 47.892' E	1345	23.04.2013	05:01	27.04.2013	03:17
EM04	22° 03.472' N	119° 48.050' E	1353	23.04.2013	06:23	27.04.2013	03:52
EM05	22° 03.530' N	119° 48.248' E	1408	23.04.2013	08:05	27.04.2013	04:34
EM06	22° 03.583' N	119° 48.436' E	1488	23.04.2013	09:58	27.04.2013	05:09
EM07	22° 03.636' N	119° 48.646' E	1560	23.04.2013	11:35	27.04.2013	05:50
EM08	22° 03.669' N	119° 48.864' E	1585	23.04.2013	13:16	27.04.2013	06:11
EM09	22° 03.697' N	119° 49.121' E	1605	23.04.2013	14:49	27.04.2013	06:49
EM10	22° 03.761' N	119° 49.364' E	1627	23.04.2013	16:39	27.04.2013	07:20
EM11	22° 03.780' N	119° 49.602' E	1644	23.04.2013	18:22	27.04.2013	07:50
EM12	22° 03.842' N	119° 49.852' E	1580	23.04.2013	20:02	27.04.2013	08:27

5.2: Sputnik transmitting stations

Sputnik stations: Formosa Ridge						
SO227	station	Profile 1			Transmitting	
		latitude	longitude	depth (m)	date	time UTC
017-1	01	22° 04.709' N	119° 19.045' E	1527	13.04.2013	06:01
	02	22° 04.780' N	119° 18.989' E	1480	13.04.2013	07:27
	03	22° 04.884' N	119° 18.939' E	1476	13.04.2013	13:01
	04	22° 05.067' N	119° 18.785' E	1487	13.04.2013	14:26
	05	22° 05.145' N	119° 18.716' E	1462	13.04.2013	15:13
	06	22° 05.207' N	119° 18.643' E	1444	13.04.2013	15:46
	07	22° 05.258' N	119° 18.515' E	1466	13.04.2013	17:09
022-1	08	22° 05.120' N	119° 18.714' E	1424	17.04.2013	00:11
	09	22° 05.173' N	119° 18.638' E	1410	17.04.2013	00:44
	10	22° 05.233' N	119° 18.604' E	1394	17.04.2013	01:13
	11	22° 05.315' N	119° 18.519' E	1370	17.04.2013	02:08
	12	22° 05.322' N	119° 18.439' E	1408	17.04.2013	02:49
	13	22° 05.415' N	119° 18.413' E	1355	17.04.2013	03:28
	14	22° 05.454' N	119° 18.364' E	1333	17.04.2013	04:06
	15	22° 05.541' N	119° 18.315' E	1305	17.04.2013	04:46
	16	22° 05.626' N	119° 18.251' E	1264	17.04.2013	05:18
	17	22° 05.724' N	119° 18.197' E	1245	17.04.2013	05:53
	18	22° 05.821' N	119° 18.145' E	1235	17.04.2013	06:29
	19	22° 05.911' N	119° 18.073' E	1221	17.04.2013	07:02
	20	22° 05.906' N	119° 18.057' E	1199	17.04.2013	07:23
	21	22° 06.005' N	119° 17.960' E	1198	17.04.2013	08:05
	22	22° 06.050' N	119° 17.928' E	1242	17.04.2013	12:57

SONNE Cruise Report S0227 TAIFLUX

	02	22° 03.454' N	119° 47.938' E	1342	24.04.2013	07:24
	03	22° 03.459' N	119° 47.997' E	1342	24.04.2013	07:51
	04	22° 03.414' N	119° 48.041' E	1344	24.04.2013	08:15
	05	22° 03.486' N	119° 48.107' E	1348	24.04.2013	08:45
	06	22° 03.520' N	119° 48.163' E	1369	24.04.2013	09:20
	07	22° 03.565' N	119° 48.350' E	1444	24.04.2013	10:10
	08	22° 03.563' N	119° 48.420' E	1475	24.04.2013	11:00
	09	22° 03.579' N	119° 48.479' E	1501	24.04.2013	11:31
	10	22° 03.588' N	119° 48.541' E	1529	24.04.2013	11:59
	11	22° 03.612' N	119° 48.613' E	1554	24.04.2013	12:33
	12	22° 03.624' N	119° 48.670' E	1563	24.04.2013	13:01
	13	22° 03.632' N	119° 48.746' E	1573	24.04.2013	13:47
	14	22° 03.626' N	119° 48.772' E	1496	24.04.2013	14:11
	15	22° 03.673' N	119° 48.888' E	1572	24.04.2013	14:51
	16	22° 03.641' N	119° 48.876' E	1580	24.04.2013	15:18
	17	22° 03.650' N	119° 48.929' E	1497	24.04.2013	15:43
	18	22° 03.653' N	119° 48.925' E	1586	24.04.2013	16:04
	19	22° 03.655' N	119° 48.988' E	1589	24.04.2013	16:34
	20	22° 03.669' N	119° 49.042' E	1594	24.04.2013	17:05
	21	22° 03.674' N	119° 49.110' E	1598	24.04.2013	17:32
	22	22° 03.707' N	119° 49.151' E	1602	24.04.2013	18:09
	23	22° 03.709' N	119° 49.223' E	1605	24.04.2013	18:52
	24	22° 03.718' N	119° 49.262' E	1608	24.04.2013	19:17
	25	22° 03.731' N	119° 49.327' E	1613	24.04.2013	19:43
	26	22° 03.747' N	119° 49.389' E	1620	24.04.2013	20:25
	27	22° 03.772' N	119° 49.441' E	1622	24.04.2013	20:59
	28	22° 03.754' N	119° 49.501' E	1623	24.04.2013	21:29
	29	22° 03.770' N	119° 49.575' E	1627	24.04.2013	22:07
	30	22° 03.795' N	119° 49.644' E	1632	24.04.2013	22:50

SONNE Cruise Report S0227 TAIFLUX

	31	22° 03.805' N	119° 49.705' E	1635	24.04.2013	23:20
	32	22° 03.736' N	119° 49.760' E	1629	24.04.2013	23:58
	33	22° 03.838' N	119° 49.802' E	1636	25.04.2013	00:29
	34	22° 03.854' N	119° 49.860' E	1638	25.04.2013	01:22
	35	22° 03.860' N	119° 49.932' E	1640	25.04.2013	01:57
	36	22° 03.864' N	119° 50.039' E	1642	25.04.2013	02:50
	37	22° 03.871' N	119° 50.085' E	1643	25.04.2013	03:13
032-2	38	22° 03.354' N	119° 47.449' E	1423	25.04.2013	07:22
	39	22° 03.368' N	119° 47.496' E	1405	25.04.2013	07:56
	40	22° 03.344' N	119° 47.543' E	1394	25.04.2013	08:42
	41	22° 03.403' N	119° 47.554' E	1382	25.04.2013	09:12
	42	22° 03.419' N	119° 47.659' E	1376	25.04.2013	09:39
	43	22° 03.440' N	119° 47.746' E	1363	25.04.2013	10:13
	44	22° 03.449' N	119° 47.786' E	1357	25.04.2013	10:38

Appendix 6: HyBis transects

SO227	transect	start				End			
		date	time	latitude	longitude	Date	time	latitude	longitude
034-1	1	26.04.2013	04:43	22° 3,51' N	119° 48,17' E	26.04.2013	08:10	22° 3,49' N	119° 47,98' E
035-1	2	26.04.2013	08:11	22° 3,50' N	119° 47,98' E	26.04.2013	12:43	22° 3,37' N	119° 47,40' E
037-1	3	26.04.2013	14:25	21° 58,12' N	119° 47,59' E	26.04.2013	17:42	21° 58,11' N	119° 47,88' E
037-2	4	26.04.2013	17:43	21° 58,11' N	119° 47,89' E	27.04.2013	00:48	21° 57,98' N	119° 48,57' E
039-1	5	27.04.2013	11:40	22° 7,02' N	119° 16,45' E	27.04.2013	17:39	22° 6,94' N	119° 17,12' E
039-2	6	27.04.2013	17:40	22° 6,94' N	119° 17,12' E	27.04.2013	19:30	22° 6,94' N	119° 17,13' E
039-3	7	27.04.2013	19:32	22° 6,93' N	119° 17,13' E	27.04.2013	22:38	22° 6,89' N	119° 17,26' E
039-4	8	27.04.2013	23:15	22° 5,52' N	119° 17,63' E	28.04.2013	02:04	22° 5,72' N	119° 17,73' E
039-5	9	28.04.2013	02:37	22° 7,65' N	119° 18,13' E	28.04.2013	05:38	22° 8,00' N	119° 18,34' E
040-1	10	28.04.2013	06:18	22° 8,95' N	119° 16,03' E	28.04.2013	13:42	22° 10,22' N	119° 15,61' E

Appendix 7: Heat flow stations

Heat flow stations: Formosa Ridge					
station	latitude	longitude	depth	date	time
015-1	22° 05.996' N	119° 15.203' E	1932	11.04.2013	18:04
015-2	22° 09.041' N	119° 16.021' E	1127	11.04.2013	20:39
015-3	22° 09.275' N	119° 15.866' E	1139	11.04.2013	21:24
015-4	22° 09.509' N	119° 15.764' E	1260	11.04.2013	22:08
015-5	22° 09.712' N	119° 15.630' E	1452	11.04.2013	22:55
018-1	22° 09.963' N	119° 15.500' E	1614	13.04.2013	20:59
018-2	22° 10.424' N	119° 15.216' E	1616	13.04.2013	23:33
018-3	22° 10.643' N	119° 15.054' E	1530	14.04.2013	00:17

SONNE Cruise Report S0227 TAIFLUX

021-1	22° 06.552' N	119° 16.429' E	1492	16.04.2013	16:12
021-2	22° 06.636' N	119° 16.606' E	1381	16.04.2013	17:00
021-3	22° 06.832' N	119° 16.789' E	1307	16.04.2013	17:38
021-4	22° 06.840' N	119° 16.970' E	1222	16.04.2013	18:15
021-5	22° 06.882' N	119° 17.087' E	1160	16.04.2013	18:50
021-6	22° 06.892' N	119° 17.155' E	1143	16.04.2013	19:35
021-7	22° 06.972' N	119° 17.221' E	1196	16.04.2013	20:31
021-8	22° 07.031' N	119° 17.366' E	1270	16.04.2013	21:08
041-1	22° 09.289' N	119° 15.211' E	1528	28.04.2013	15:35
041-2	22° 09.288' N	119° 15.459' E	1312	28.04.2013	16:19
041-3	22° 09.282' N	119° 15.726' E	1172	28.04.2013	16:59
041-4	22° 08.970' N	119° 15.612' E	1483	28.04.2013	17:49
041-5	22° 08.092' N	119° 16.520' E	1224	28.04.2013	19:58
041-6	22° 08.184' N	119° 16.729' E	1308	28.04.2013	20:52
041-7	22° 06.173' N	119° 17.131' E	1363	28.04.2013	23:25
041-8	22° 06.310' N	119° 17.364' E	1240	29.04.2013	00:17
041-9	22° 06.368' N	119° 17.507' E	1204	29.04.2013	00:59
041-10	22° 06.424' N	119° 17.582' E	1185	29.04.2013	01:29
041-11	22° 06.465' N	119° 17.720' E	1245	29.04.2013	02:37
043-1	22° 05.624' N	119° 17.780' E	1368	29.04.2013	14:19
043-2	22° 05.805' N	119° 18.069' E	1285	29.04.2013	15:13
043-3	22° 05.929' N	119° 18.327' E	1387	29.04.2013	15:58

Heat flow stations: Four Way Closure					
station	latitude	longitude	depth	date	time
033-1	22° 03.859' N	119° 50.055' E	1651	25.04.2013	13:14
033-2	22° 03.749' N	119° 49.497' E	1629	25.04.2013	14:40
033-3	22° 03.655' N	119° 49.012' E	1595	25.04.2013	15:57
033-4	22° 03.566' N	119° 48.565' E	1533	25.04.2013	16:53
033-5	22° 03.495' N	119° 48.137' E	1360	25.04.2013	18:10
033-6	22° 03.461' N	119° 47.956' E	1351	25.04.2013	18:58

SONNE Cruise Report S0227 TAIFLUX

033-7	22° 03.430' N	119° 47.759' E	1364	25.04.2013	19:36
033-8	22° 03.379' N	119° 47.521' E	1408	25.04.2013	20:46
033-9	22° 03.344' N	119° 47.244' E	1563	25.04.2013	21:43
033-10	22° 03.280' N	119° 46.970' E	1646	25.04.2013	22:33
047-1	22° 02.967' N	119° 45.165' E	1958	30.04.2013	03:21
047-2	22° 03.034' N	119° 45.629' E	1925	30.04.2013	04:21
047-3	22° 03.128' N	119° 46.120' E	1718	30.04.2013	05:19
047-4	22° 03.146' N	119° 46.266' E	1662	30.04.2013	05:50
047-5	22° 03.160' N	119° 46.616' E	1756	30.04.2013	06:39

Appendix 8: TV-Grap

	TV-Grap stations: Formosa Ridge					
SO227	station	date	time	latitude	longitude	depth (m)
042-2	01	29.04.2013	08:16	22° 06.971' N	119° 17.133' E	1150
042-3	02	29.04.2013	11:45	22° 06.960' N	119° 17.129' E	1143
050-1	03	01.05.2013	05:26	22° 06.930' N	119° 17.119' E	1122
050-2	04	01.05.2013	07:04	22° 06.924' N	119° 17.132' E	1122
	TV-Grap stations: Four Way Closure					
048-1	01	30.04.2013	09:50	22° 03.528' N	119° 47.979' E	1355
048-2	02	30.04.2013	11:53	22° 03.498' N	119° 47.999' E	1346
048-3	03	30.04.2013	15:00	22° 03.420' N	119° 47.978' E	1217

Appendix 9: Sound velocity profiles

SO227	latitude	longitude	depth (m)	date	time UTC	
					surface	Depth
001-2	22° 00.050' N	119° 39.810' E	2367	02.04.2013	05:11	06:02
051-1	21° 56.842' N	119° 31.460' E	2500	01.05.2013	09:35	10:40

GEOMAR Reports

No.	Title
1	FS POSEIDON Fahrtbericht / Cruise Report POS421, 08. – 18.11.2011, Kiel - Las Palmas, Ed.: T.J. Müller, 26 pp, DOI: 10.3289/GEOMAR_REP_NS_1_2012
2	Nitrous Oxide Time Series Measurements off Peru – A Collaboration between SFB 754 and IMARPE –, Annual Report 2011, Eds.: Baustian, T., M. Graco, H.W. Bange, G. Flores, J. Ledesma, M. Sarmiento, V. Leon, C. Robles, O. Moron, 20 pp, DOI: 10.3289/GEOMAR_REP_NS_2_2012
3	FS POSEIDON Fahrtbericht / Cruise Report POS427 – Fluid emissions from mud volcanoes, cold seeps and fluid circulation at the Don-Kuban deep sea fan (Kerch peninsula, Crimea, Black Sea) – 23.02. – 19.03.2012, Burgas, Bulgaria - Heraklion, Greece, Ed.: J. Bialas, 32 pp, DOI: 10.3289/GEOMAR_REP_NS_3_2012
4	RV CELTIC EXPLORER EUROFLEETS Cruise Report, CE12010 – ECO2@NorthSea, 20.07. – 06.08.2012, Bremerhaven – Hamburg, Eds.: P. Linke et al., 65 pp, DOI: 10.3289/GEOMAR_REP_NS_4_2012
5	RV PELAGIA Fahrtbericht / Cruise Report 64PE350/64PE351 – JEDDAH-TRANSECT –, 08.03. – 05.04.2012, Jeddah – Jeddah, 06.04 - 22.04.2012, Jeddah – Duba, Eds.: M. Schmidt, R. Al-Farawati, A. Al-Aidaroos, B. Kurten and the shipboard scientific party, 154 pp, DOI: 10.3289/GEOMAR_REP_NS_5_2013
6	RV SONNE Fahrtbericht / Cruise Report SO225 - MANIHIKI II Leg 2 The Manihiki Plateau - Origin, Structure and Effects of Oceanic Plateaus and Pleistocene Dynamic of the West Pacific Warm Water Pool, 19.11.2012 - 06.01.2013 Suva / Fiji – Auckland / New Zealand, Eds.: R. Werner, D. Nürnberg, and F. Hauff and the shipboard scientific party, 176 pp, DOI: 10.3289/GEOMAR_REP_NS_6_2013
7	RV SONNE Fahrtbericht / Cruise Report SO226 – CHRIMP CHatham RIse Methane Pockmarks, 07.01. – 06.02.2013 / Auckland – Lyttleton & 07.02. – 01.03.2013 / Lyttleton – Wellington, Eds.: Jörg Bialas / Ingo Klauke / Jasmin Mögeltönder, 126 pp, DOI: 10.3289/GEOMAR_REP_NS_7_2013
8	The SUGAR Toolbox - A library of numerical algorithms and data for modelling of gas hydrate systems and marine environments, Eds.: Elke Kossel, Nikolaus Bigalke, Elena Piñero, Matthias Haeckel, 168 pp, DOI: 10.3289/GEOMAR_REP_NS_8_2013
9	RV ALKOR Fahrtbericht / Cruise Report AL412, 22.03.-08.04.2013, Kiel – Kiel. Eds: Peter Linke and the shipboard scientific party, 38 pp, DOI: 10.3289/GEOMAR_REP_NS_9_2013
10	Literaturrecherche, Aus- und Bewertung der Datenbasis zur Meerforelle (Salmo trutta trutta L.) Grundlage für ein Projekt zur Optimierung des Meerforellenmanagements in Schleswig-Holstein. Eds.: Christoph Petereit, Thorsten Reusch, Jan Dierking, Albrecht Hahn, 158 pp, DOI: 10.3289/GEOMAR_REP_NS_10_2013

For GEOMAR Reports, please visit:

https://oceanrep.geomar.de/view/series/GEOMAR_Report.html

Reports of the former IFM-GEOMAR series can be found under:
https://oceanrep.geomar.de/view/series/IFM-GEOMAR_Report.html

Das GEOMAR Helmholtz-Zentrum für Ozeanforschung Kiel
ist Mitglied der Helmholtz-Gemeinschaft
Deutscher Forschungszentren e.V.

The GEOMAR Helmholtz Centre for Ocean Research Kiel
is a member of the Helmholtz Association of
German Research Centres

Helmholtz-Zentrum für Ozeanforschung Kiel / Helmholtz Centre for Ocean Research Kiel

GEOMAR
Dienstgebäude Westufer / West Shore Building
Düsternbrooker Weg 20
D-24105 Kiel
Germany

Helmholtz-Zentrum für Ozeanforschung Kiel / Helmholtz Centre for Ocean Research Kiel

GEOMAR
Dienstgebäude Ostufer / East Shore Building
Wischhofstr. 1-3
D-24148 Kiel
Germany

Tel.: +49 431 600-0
Fax: +49 431 600-2805
www.geomar.de